UNIVERSITY OF CAPE TOWN
IYUNIVESITHI YASEKAPA • UNIVERSITEIT VAN KAAPSTAD

sasol
reaching new frontiers

Carbidization and size effects of unsupported nano-sized iron in the low temperature Fischer-Tropsch process

By

Muhammad Ali Amod

Submitted to the University of Cape Town
in fulfillment of the requirements
for the degree of
Masters in Science

Department of Chemical Engineering

November, 2011

Acknowledgements

This thesis was developed from January 2009 to November 2011 at the Centre for Catalysis Research in the Department of Chemical Engineering at the University of Cape Town (UCT).

I am very grateful to my supervisors, Prof. Michael Claeys and Prof. Eric van Steen, who have advised me throughout my thesis. Special thanks to Prof. Michael Claeys for his great efforts and patience during the thesis correction stage.

I would also like to thank Mr. Mohammed Jaffer from the Electron Microscope Unit at UCT. Thanks to Debbie De Jager, Rosalind Maree, Eloise Williams, Nico Fischer and Theresa Feltes for their support.

Thanks to my sponsor, Sasol, for their financial support.

Abstract

In the process of developing the most efficient production of fuels from coal or natural gas, there have been major advancements in the development of the catalysts used. The Centre for Catalysis Research at UCT has had many research projects that determine the size and phase effects on the catalysts' activity and selectivity in the Fischer-Tropsch process.

Previous work conducted in the Centre for Catalysis Research has shown great potential and provided a much deeper understanding of the workings of the Fischer-Tropsch catalyst. The research has found that the catalyst crystallite size plays a crucial part in the product selectivity and requires strict control in order to obtain a certain desired product spectrum. The purpose of this research project is to provide insight on the behavior of various iron oxide crystallite sizes when placed in a CO concentrated environment during catalyst pretreatment. It will also clarify as to whether the sizes of the nano-crystallites will increase or decrease when the different phases form and which size carbides faster. This is accomplished through the preparation of three crystallite size classes using the micro-emulsion reverse micelle method and observing the effects of the carbidization of the iron catalyst under various conditions in order to obtain a narrow distribution. The analysis and testing of the catalyst was conducted using both, spectroscopic (XRD) and microscopic techniques (TEM). XRD studies were conducted using an in-situ reaction cell.

The uncalcined iron precursor was identified through XRD analysis to be in the form of an iron hydroxide (FeO(OH)). The concentration of oxygen and the temperature used in the calcination process played an important role in the formation of the crystallites; their phases and sizes. Ignition caused by residual surfactant from the reverse micelle systems resulted in over-temperatures during calcinations with the higher temperatures resulting in the formation of the γ-Fe_2O_3 phase of the iron oxides, then the α-Fe_2O_3 followed by the Fe_3O_4 phase. The crystallite sizes are highly affected by the temperature as there is an increase in the size when the temperature increases and with a too high temperature, the

crystallites were distorted. A narrow distribution is attained for the medium (‘7 nm’) and large (‘15 nm’) crystallites, however, the smaller crystallite size proved to be much more difficult to obtain due to sintering at 300°C. The altered calcination step utilized for the desired small crystallite size, managed to obtain a much lower size and narrower distribution (± ‘3 nm’).

Reduction of the crystallites in hydrogen (H_2) proved to be unsatisfactory as sintering was observed, believed to be due to the production of water. Hence, the originally targeted synthesis of pure iron crystallites became difficult and did not provide the desired narrow distribution. However, reduction in carbon monoxide (CO) formed various iron carbides allowing the crystallites to maintain their narrow distribution. The CO reduction results provided insight into the size effects on the iron carbide formation and they showed that the larger crystallites form very slight amounts of carbides compared to the amount of iron and iron oxides. With the small and medium crystallites, mainly carbides (χ-Fe_5C_2 carbide and ε’-Carbides) were formed and the crystallites sizes remained largely unchanged. The amorphous iron carbides for the large crystallites do not show in the XRD analysis but they were observed by means of Mössbauer spectroscopy.

The evaluation of the small and medium crystallites was conducted in a fixed bed reactor, including CO treatment, and testing at 250°C, 20 bars and with a H_2/CO ratio of 2 for their Fischer-Tropsch performance. The crystallites phases did not change significantly after the Fischer-Tropsch process. The CO steady state conversion values were 9.5% and 6% for the small and medium crystallites, respectively. However, the surface area specific activity was found to be higher in the medium crystallites than the small crystallites. The methane selectivity was higher for the smaller crystallites and the CO_2 selectivity was higher for the larger crystallites corresponding to findings obtained from previous research where supported iron crystallites were used. It was found that the olefin selectivity was higher for the smaller crystallites than the medium crystallites.

The products also consisted of small amounts of oxygenates, 11 C-% for the small crystallites and 13 C-% for the medium crystallites. Trace amounts of branched products were found to be 2.7 C-% and 3 C-% for the small and medium crystallites, respectively.

Table of Contents

List of Figures

List of Tables

Nomenclature

n	Hydrocarbon with carbon number n
w_n	Weight fraction of carbon number n [wt%]
α	Chain growth probability
P_{CO}	Partial pressure of carbon monoxide [bar]
P_{H2}	Partial pressure of hydrogen [bar]

Glossary

FT	Fischer-Tropsch
FTS	Fischer-Tropsch Synthesis
TOS	Time On Stream
TOF	Turn Over Frequency
R_{wp}	Weighted Profile R-factor
HCNs	Hydrocarbon Number
LTFT	Low Temperature Fischer-Tropsch
HTFT	High Temperature Fischer-Tropsch
WGS	Water Gas Shift
XRD	X-Ray Diffraction
TEM	Transmission Electron Microscopy
HRTEM	High Resolution Transmission Electron Microscopy

1 Introduction

Due to the advancement of technology and our increased use of machinery for transportation, i.e. automobiles, ships and airplanes, it was necessary to look for a more efficient and abundant energy source. This promoted the use of petrochemicals and provided the basis for the shift to liquid fuels rather than solid fuels (such as coal and wood) as a major energy source (Stranges, 2007).

This is the foundation for the development of the Fischer-Tropsch process where natural gas or coal is catalytically converted to synthesis gas (CO and H_2) to produce a wide range of hydrocarbon products (petrol, diesel, olefins, oxygenates and aromatics) (Dry, 2004). In the Fischer-Tropsch process, the catalyst chosen plays a crucial part in the product selectivity and the overall plant since it dictates the behavior of the recycle streams and the catalyst's lifetime. This defines the motivation behind the increased research and development of Fischer-Tropsch catalysts. One aspect presently being investigated is the development to obtain the optimum crystallite size for iron catalysts and provide a further understanding on the workings of the iron catalyst. Previous research has shown that the decrease in crystallite size of supported metallic iron shows inferior behavior with regards to activity and selectivity (Cheang, 2009). This project will look at the synthesis of unsupported nano-sized iron crystallites and their reduction behavior in a H_2 and CO atmosphere. The different nano-sized iron carbide crystallites are then tested (for the first time) in the low temperature Fischer-Tropsch process.

This thesis consists of a section that focuses on the previous literature providing the information required to obtain the desired objectives of the research study. This is then followed by the project's aims, objectives, key questions and hypotheses. The experimental methodology and catalyst characterization is then discussed to provide information on how the catalyst is synthesized, characterized and tested. The results obtained from the experiments can be seen in the results section where the experimental outcomes are discussed. The summary of the findings is then outlined in the conclusions section and recommendations for further study have been proposed thereafter.

2 Literature Review

2.1 Energy

Fossil fuels, defined as oil, coal and natural gas, supply more than 80% of the world's energy. The world's economical, technological and social development is considered dependent on the availability and consumption of fossil fuels causing a country's progression to be shaped, in many aspects, to their access to these energy sources. However, there are major concerns regarding their usage, availability, waste disposal and accidents. Out of all this, the rising energy costs are the one major factor driving new research towards alternative energy sources (Steynberg, 2004).

This leads to the implementation and optimization of new and existing processes. This is the basis for the current industrial development and research trends for the Fischer-Tropsch synthesis process from which the production of hydrocarbon fuels is achieved from coal and, more recently, natural gas (Steynberg, 2004). This process is the fundamental driving force for the work found in this thesis.

2.2 Fischer-Tropsch Process

2.2.1 History

During the 1920s, two scientists at the Kaiser Wilhelm Institute for Coal Research in Germany, Franz Fischer and Hans Tropsch, developed a process whereby they gasified coal to form a mixture of hydrogen and carbon monoxide which is then converted to liquid hydrocarbons (petroleum) (Steynberg, 2004).

This was accomplished by reacting coal with steam (the steam reforming / partial oxidation process) to produce CO and H_2 (known as synthesis gas). Through vigorous experimental research, the synthesis gas was fed into a reactor containing cobalt/iron catalysts and operating at 250 – 300°C and 1 atmosphere. The ratio of hydrogen to carbon monoxide (H_2/CO) fed to the reactor was 2 (explained further in section 2.2.2). This process came to be known as the Fischer-Tropsch (FT) process,

named after the discovering scientists. There are three distinct segments within the FT process: the synthesis gas generation, FT synthesis and product refining (Steynberg, 2004; Stranges, 2007).

This research project exclusively investigates the FT synthesis segment, thus, the following literature review will only discuss this portion of the process. To understand the capabilities of the Fischer-Tropsch Synthesis (FTS), it is necessary to look at the reactions that take place and conditions these reactions occur under.

2.2.2 Reaction Mechanisms, Conditions and Products

The Fischer-Tropsch product range consists of a variety of products including mostly linear hydrocarbons and oxygenated products (van der Laan, 1999).

Reactions

Many reactions take place in the FT reactor. However, the most credited reactions are listed below:

The basic chain growth reaction (Olefin Production)

$nCO + 2nH_2 \rightarrow C_nH_{2n} + nH_2O$ Reaction 2.1

Paraffin Formation

$nCO + (2n+1)H_2 \rightarrow C_nH_{2n+2} + nH_2O$ Reaction 2.2

Methane Production

$CO + 3H_2 \rightarrow CH_4 + H_2O$ Reaction 2.3

Alcohol Production

$nCO + 2nH_2 \rightarrow C_nH_{2n+2}O + (n-1)H_2O$ Reaction 2.4

Water Gas Shift (WGS) Reaction

$CO + H_2O \leftrightarrow CO_2 + H_2$ Reaction 2.5

Boudouard Reaction

$2CO \rightarrow CO_2 + C$ Reaction 2.6

(van der Laan, 1999; Dry, 2004)

Reactions 2.1 and 2.2 are considered the main reactions which produce the long chain hydrocarbons. The ratio of H_2 to CO in the syngas is very important in obtaining a desired selectivity of the desired products. The ratio is manipulated to alter product composition, for example, when a low ratio is utilized a more olefinic product can be achieved. The WGS reaction (Reaction 2.5), which usually takes place on an iron catalyst, plays an important role in shifting the H_2 to CO ratio, which can affect the product selectivity. Therefore, when there is high water gas activity, the syngas ratio will increase and result in a greater selectivity of paraffins. However, reaction performance is also dependent on many other factors, most prominently being the reaction temperature and catalyst formulation.

Operating Temperature

There are 2 types of industrial Fischer-Tropsch operations; the low temperature Fischer-Tropsch (LTFT) and high temperature Fischer-Tropsch (HTFT) processes, which were first implemented commercially by Sasol (van der Laan, 1999; Dry, 2004). The LTFT operation is between 245°C and 265°C and produces mainly waxes and middle distillate (diesel) products. The HTFT operation takes place between 300°C and 350°C and produces gasoline, olefins and lower carbon chain hydrocarbons (Dry, 2004). The general understanding of the temperature effect is that when the temperature increases, it is expected that the products will decrease in molecular size and more of the high temperature thermodynamically stable products are formed (alkenes). The temperature increase will also increase the amount of branched and aromatic products (Dry, 2002).

Fischer-Tropsch Product Distribution and Selectivity

No matter what the operating conditions, in the Fischer-Tropsch process a wide range of hydrocarbons (mainly olefins and paraffin) and oxygenates products are expected. The FT synthesis is a polymerization process and a simple chain growth mechanism for one sort of product is provided in Figure 2.1.

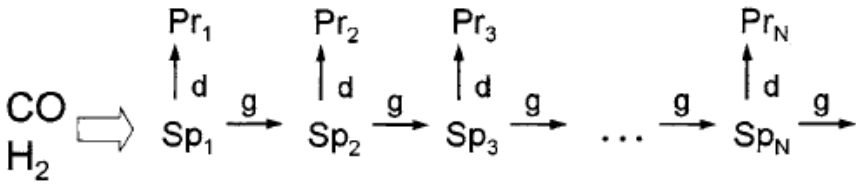

Figure 2.1: Polymerization chain growth and product desorption in FTS (Claeys and van Steen, 2004)

Where: Sp_n = Surface species with carbon number n

Pr_n = Product species with carbon number n

The product distribution can be generally modeled by the Anderson-Schulz-Flory (ASF) equation:

$$W_n/n = \alpha^{n-1}(1-\alpha)^2 \qquad \text{Equation 2.1}$$

Where: n = hydrocarbon of carbon number n

w_n = the weight fraction of carbon number n

α = the chain growth propagation probability

(Bartholomew and Farrauto, 2007)

This mathematical model depicts the FT product distribution reasonably, however, due to the occurrences of secondary reactions; slight deviations can be observed. This can be seen in Figure 2.2 below:

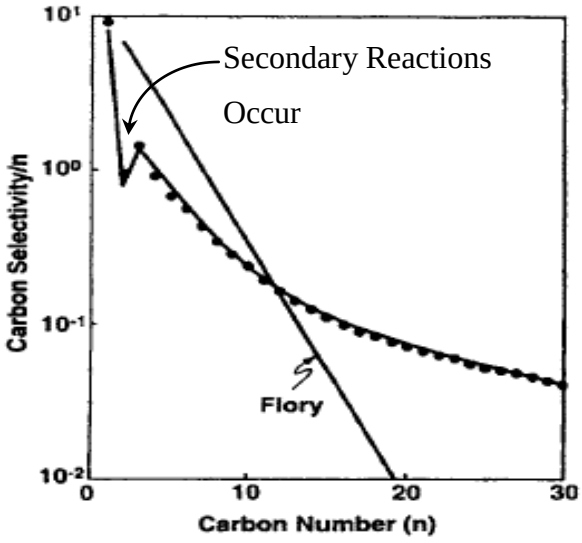

Figure 2.2: Ideal and modified product distribution of model & experimental (Claeys and van Steen, 2004)

It is important to note that the methane production is often higher and the C_2 hydrocarbon selectivity is lower than expected. Re-adsorption and incorporation of primarily formed olefins can lead to a curvature in the product distribution; the high reactivity of ethene causing the relatively low C_2 content (Claeys and van Steen, 2004).

This model only provides a general understanding of the product distribution and the range of α value is dependent on the operating conditions and catalyst. The FT catalyst is a major research area within the FT process and these catalysts are discussed in detail in the following section.

2.3 Fischer-Tropsch Catalysts

2.3.1 Types

The catalysts utilized in the Fischer-Tropsch process need to be highly active and selective in order for the process to be feasible. The catalysts that are the most active in the Fischer-Tropsch process are cobalt, ruthenium, nickel, iron and rhodium. Ruthenium, cobalt, rhodium and nickel are much more expensive catalysts than iron and the relative costs can be seen in the table below (Table 2.1).

Table 2.1: Relative costs of FT active metals (van der Laan, 1999; Dry, 2002)

Metal	Relative Cost
Iron	1
Nickel	250
Cobalt	1000
Ruthenium	31,000
Rhodium	570,000

Rhodium and ruthenium are the most active FT catalysts but they are currently not implemented commercially because they are very expensive and scarce. The nickel catalyst produces a lot of CH_4 (methane) which is undesired and is usually utilized to convert methane to synthesis gas via steam reforming. It is also considered to be

unstable since it readily forms volatile nickel carbonyls. The remaining active catalysts are the iron and cobalt catalysts, which are utilized the most in industry.

Cobalt is very expensive, yet has a high intrinsic activity and stability compared to iron. However, it is typically utilized in the LTFT process and not utilized in the HTFT process as it produces predominantly methane at high temperatures. As a result, the main products are linear long-chain hydrocarbons, i.e. high molecular weight paraffins/waxes (Dry, 2002; Schulz, 2007). The iron catalyst is utilized in both the LTFT and HTFT operations. It is the cheapest of the FT catalysts and it is usually applied to processes with syngas derived from carbon-rich sources (coal or biomass) because of its good WGS activity which can reduce the cost of utilizing a WGS unit (Remans et al., 2008). The iron catalyst produces more olefins and oxygenates in the product than the cobalt catalyst. At low temperatures, the iron catalyst produces less methane than the cobalt catalyst. However, the cobalt catalyst forms methane at a much faster rate than the iron catalyst when the temperature is too high (Dry, 2002; Schulz, 2007).

Although the temperature and catalyst chosen have a profound effect on the product selectivity, there are other aspects of the catalyst (such as crystallite size) that can be used to optimize and improve the catalyst activity, selectivity and life-time.

2.3.2 Iron

It has been debated that there are various forms of FT catalysts such as metals, metal oxides, metal carbides and supported catalysts (Li et al., 2002, de Smit et al., 2010). All metals are considered to be electropositive as they readily give off free valence electrons allowing reactions to take place on the metal surface. The metal of concern in this thesis is iron and its various forms will be discussed.

Iron Properties

Iron belongs to group 8 of the periodic table and is considered to be much more stable as an oxide at room temperature than metallic iron. It has a very low electron

binding energy making it highly electropositive which contributes to understanding its activity in the FT process (Kammermeier, 1998).

Iron Phases

The iron catalyst, after preparation via precipitation, is initially often present in the form of iron hydroxide phases ($FeO(OH)_x$) which can then be dehydrated into hematite, α-Fe_2O_3 (Cornell and Schwertmann, 2003). This is then calcined in air at high temperatures to form iron oxides. There are three main iron oxides: hematite (α-Fe_2O_3), maghemite (γ-Fe_2O_3) and magnetite (Fe_3O_4). Before the catalyst is added to the reactor, it is pretreated; on a laboratory scale this pre-treatment is often conducted in the FT test reactor. The iron oxides are normally reduced in hydrogen and converted from Fe_2O_3 to form Fe_3O_4 and then the metallic iron phase (Li et al., 2002; Sarkar and Davis, 2007; de Smit et al., 2010). During the FT process, there is a quick transformation that produces both oxides and carbides as seen by Dry (2004) in Figure 2.3. This schematic represents the different iron phases present as a function of time on stream run in an HTFT fluidized bed that was operated at 330°C and 22 bars. The carbides formed in the FT synthesis using the iron catalysts remain throughout the process and the stability of these carbides are a function of the reaction conditions (Sarkar and Davis, 2007).

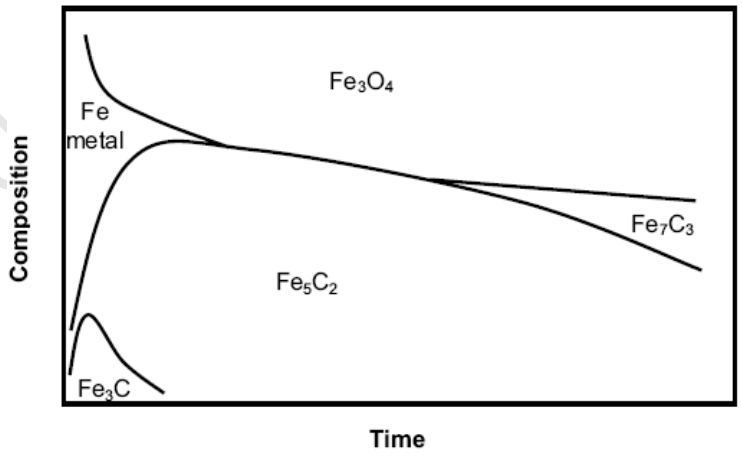

Figure 2.3: Phase changes of the Fe catalyst during the FT synthesis (Dry, 2004)

It should be noted that the spent catalysts do not normally contain metallic iron suggesting that the iron carbides are the active phases. However, previous studies

have shown that the active carbide phases can further transform into less active carbide phases and into inactive carbon phases such as the formation of graphite and coke (Ferdous and Demirel, 2010, Pour et al., 2010).

2.3.3 Metallic Iron, Iron Carbides and Iron Oxides

In Figure 2.3 it is shown that the metallic iron over time is quickly converted to a mixture of the magnetite (Fe_3O_4); Hägg carbide (χ-Fe_5C_2) and the pseudo-cementite (Fe_3C) which is then converted further into the χ-Fe_5C_2 and Fe_7C_2 carbides (Bartholomew and Farrauto, 2007) during the FT reaction. Other carbide phases used as FT catalysts, often reported in literature, also include ε-Fe_2C and ε'-$Fe_{2.2}C$ carbides (de Smit et al., 2010).

To further investigate the formation of these carbides, a study conducted by Kalakkad et al. (1995) has shown that when the reduction of the iron oxide (Fe_2O_3) catalyst precursor is conducted under CO at 100°C, trace amounts of Fe_3O_4 start to form. At 200°C, this catalyst is mainly transformed to Fe_3O_4 and the Fe_3O_4 (magnetite) phases is dominant at 270°C. At the temperature of 320°C, trace amounts of iron oxides, α-Fe and graphitized carbon were observed, however, the iron carbides are considered to be the dominant phase at this temperature. When exposed to CO at 400°C, complete transformations of all the oxides into the χ-Fe_5C_2 and Fe_3C carbides take place with traces of graphitized carbon.

Work conducted by Sarkar et al. (2007) showed that when the iron catalyst is reduced in CO at 270°C the Fe_2O_3 is transformed into a mixture of χ-Fe_5C_2 (85%) and Fe_3O_4 (15%). Ning et al. (2006) showed that the iron catalyst (Fe_2O_3) is transformed into the iron carbide at 230°C in CO atmosphere with traces of Fe_3O_4. Hayakawa et al. (2006) showed in a H_2/CO atmosphere (ratio of 1, 20 bar and 260°C) that the Fe_2O_3 precursor converts first to the Fe_3O_4 catalyst and then to the iron carbide phases. They suggested that the metallic iron did not form due to the iron readily reacting with the carbon from the dissociated CO on the surface. Research conducted by de Smit and Weckhuysen (2008) states that the ε-Fe_2C

carbide is synthesized from the iron-based catalyst when placed in a CO atmosphere at a low temperature of 170°C. The χ-Fe_5C_2 carbide is also mentioned to readily form around 250°C. In a study by de Smit et al. (2010), they synthesized 2 reference carbide materials, the χ-Fe_5C_2 and θ-Fe_3C. The χ-Fe_5C_2 (Hägg) was synthesized in CO at 350°C and the θ-Fe_3C (cementite) at 450°C. De Smit et al. (2010) found that at temperatures lower than 200°C, the ε-carbides (ε'-$Fe_{2.2}C$/ε-Fe_2C) are dominant and transform into the χ-Fe_5C_2 (Hägg) carbide at around 250°C. They also state that as the temperature increases, the χ-Fe_5C_2 carbide is transformed into the θ-Fe_3C (cementite) carbide and then the Fe_7C_3 carbide. Bian et al. (2002) reduced the iron catalyst (Fe_2O_3) in CO at 300°C and observed the formation of both, metallic iron and iron carbides (ε'-$Fe_{2.2}C$ and χ-Fe_5C_2). Luo and Davis (2003) found the same outcome as the above mentioned research. They observed that the iron catalyst is reduced to χ-Fe_5C_2 and Fe_3O_4 in a CO atmosphere at 400°C.

De Smit and Weckhuysen (2008) also stated that the metallic iron catalyst is synthesized when reducing Fe_2O_3/Fe_3O_4/FeO(OH) in an H_2 atmosphere at temperatures of 250°C – 300°C. Niemantsverdriet et al. (1980) showed that reducing the iron catalyst in H_2 at a temperature of 350°C will convert the α-Fe_2O_3 to metallic iron with traces of Fe_3O_4 present. The Fe_3O_4 was explained to be a result of the re-oxidation of the catalyst when removing it from the reactor. Bian et al. (2002) also found that reducing the Fe_2O_3 catalyst, it is transformed into the Fe_3O_4 and metallic iron catalyst (α-Fe) when exposed to H_2 at 300°C. The same outcome was observed by Luo and Davis (2003) where the Fe_2O_3 catalyst is reduced in H_2 at 400°C and formed the metallic iron (α-Fe) and Fe_3O_4 iron phases.

They, Luo and Davis (2003), also found that the Fe_2O_3 catalyst is transformed into the χ-Fe_5C_2 (Hägg) carbide and Fe_3O_4 when exposed to a 2% CO in H_2 atmosphere at 400°C. de Smit et al. (2010) conducted an analysis of the iron-based catalyst in 1% CO in H_2 at 350°C which showed the transformation of Fe_3O_4 into FeO and then the χ-Fe_5C_2 and θ-Fe_3C carbides. These studies showed that the type of iron phase that is formed is highly dependent on the temperature and the atmosphere the

catalysts are placed in. However, the trends seen do look similar when comparing the related studies (i.e. comparing the CO studies to each other).

It is important to note that in order to further increase the catalyst utilization and activity, it is necessary to optimize the crystallite surface exposure. Commercially, the iron catalysts are usually used in their bulk form (i.e. there are no supports). However, on a microscopic scale, the catalysts and the various phases therein are in fact made up of nano-sized crystallites. The term that is usually associated with determining the number of active sites on the surface relative to the total number of atoms is called the dispersion (Farkas, 2002; Niemantsverdriet and Chorkendorff, 2003). A maximum dispersion normally allows for the maximum use of the catalyst which reduces the catalyst costs.

2.3.4 Observed Nano-crystallite Activity and Selectivity

This section looks at whether a decrease in the nano-crystallite sizes (increase of dispersion) does indeed increase the catalysts' activity.

A study conducted by Bezemer et al. (2006) on various nano-sized carbon supported cobalt crystallites showed a decrease in surface specific activity below a certain size (see Figure 2.4, left). On a mass basis, indeed a maximum with respect to crystallite size exists, in this case at around 6 nm (see Figure 2.4, right). This was also observed with the alumina supported ruthenium crystallites where there was also a decrease in the TOF with decreasing crystallite size (Figure 2.5) (Barkhuizen et al., 2006; Welker, 2007).

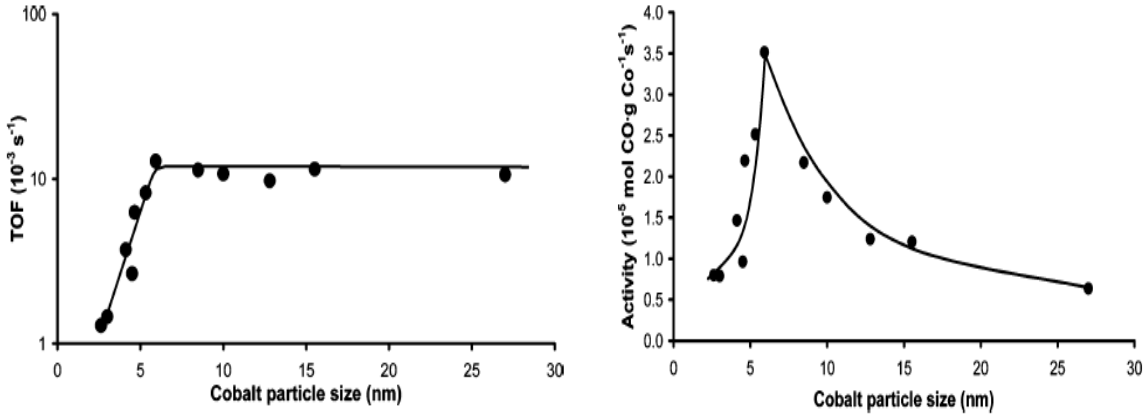

Figure 2.4: TOF and activity as a function of Co crystallite size for Co/C catalysts - 220°C, 1 bar and $H_2/CO = 2$ (Bezemer et al., 2006)

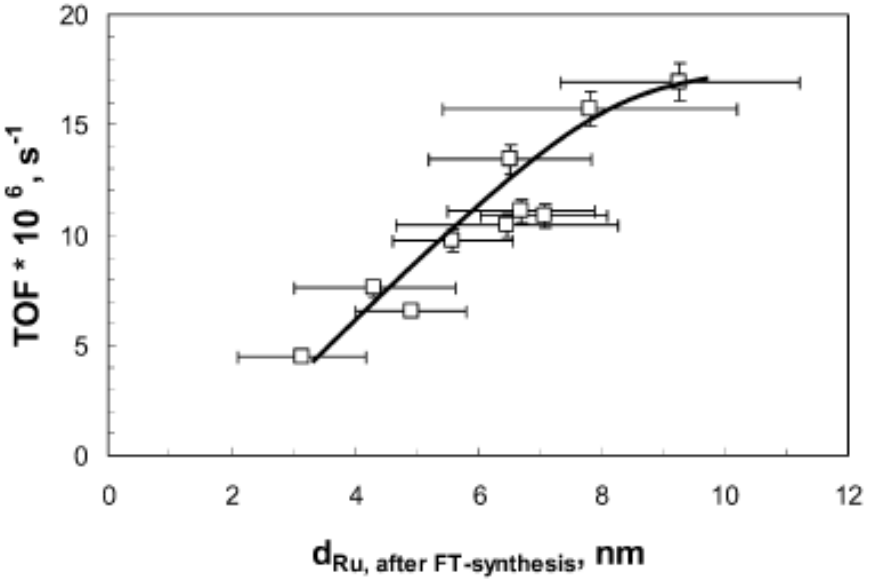

Figure 2.5: TOF as a function of Ru crystallite size for Ru/Al_2O_3 catalysts - 170°C, 1 bar and $H_2/CO = 2$ (Barkhuizen et al., 2006; Welker, 2007)

A similar trend was observed on the carbon and alumina supported, and potassium promoted, iron nano-crystallites (Mabaso, 2005; Cheang, 2009). Figure 2.6 displays the changes found by Mabaso (2005) in the integral activity per unit surface area as a function of crystallite size at the initial stages of the FT reaction. In addition, Cheang (2009) reported, more recently, that there was an increase in the methane selectivity (Figure 2.7) and a decrease in the chain growth probability with decreasing crystallite size. This increased methane selectivity, which was also found by the

others (Barkhuizen et al., 2006; Bezemer et al., 2006; Welker, 2007) and the lower activity of smaller crystallites was explained with the 'ensemble' theory (Bezemer et al., 2006; Cheang, 2009).

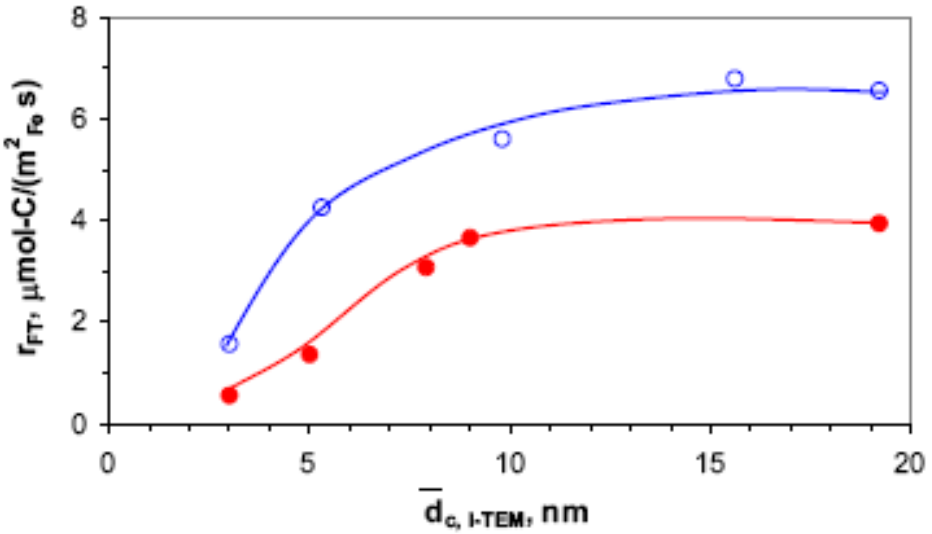

Figure 2.6: Initial state metal area specific FT rate as a function of Fe crystallite sizes for Fe/C (○) and Fe/Al_2O_3 catalysts (●) - 240°C, 10 bar and $H_2/CO = 2$ (Mabaso, 2005)

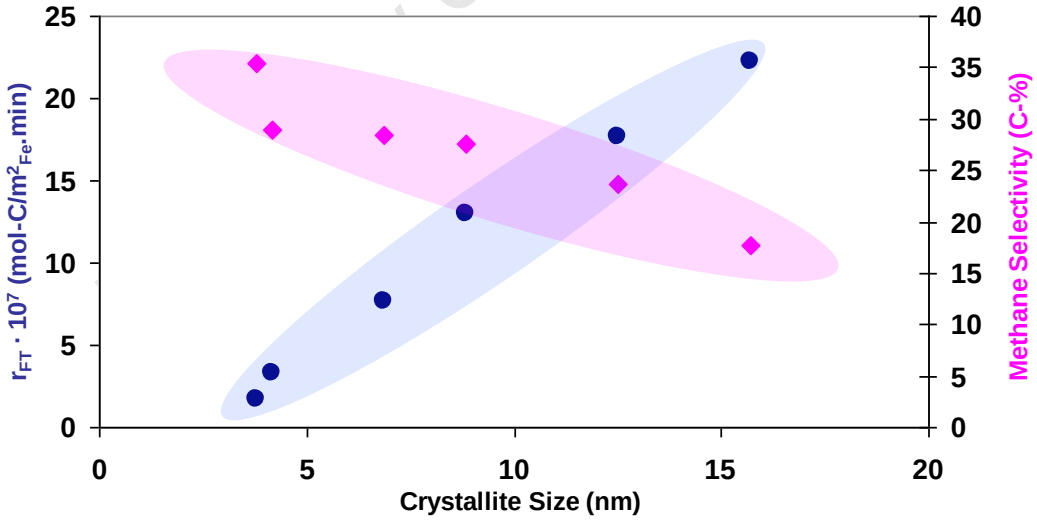

Figure 2.7: Methane selectivity as a function of Fe crystallite sizes for Fe/Al_2O_3 catalysts - 240°C, 10 bar and $H_2/CO = 2$ (Cheang, 2009)

Due to the occurrence of many different reactions that take place in the Fischer-Tropsch synthesis process, it is suggested that there is a need for a cluster of atoms,

"ensembles", in order for the formation of higher hydrocarbons, "FT activity", to take place. This means that when the crystallite sizes are smaller, less such ensembles are available, and the FT activity will decrease (see Figure 2.8). Assuming that the methane formation, which is less demanding as no chain growth is involved, can occur on simpler sites, higher methane selectivity on smaller crystallites can be explained. It has been mentioned by Bezemer et al. (2006) that the methane production is a result of the abundant amounts of dissociated hydrogen readily interacting with the limited adsorbed carbon. Therefore, smaller crystallites contain less active sites for chain growth and require a higher CO adsorption energy than the larger crystallites resulting in a much higher hydrogen to carbon ratio on the catalyst surface. This is confirmed by Welker (2007) and Cheang (2009) where they observed that the larger hydrocarbons do not form as easily as methane on the smaller crystallites due to the reduced CO adsorption on the catalyst (Schulz et al., 2002; Mabaso, 2005; Bezemer et al., 2006; Welker, 2007; Cheang, 2009). Other than the above four studies, there have not been many more studies investigating the activity effects of nano-sized catalysts. A schematic of a required ensemble is shown in Figure 2.8.

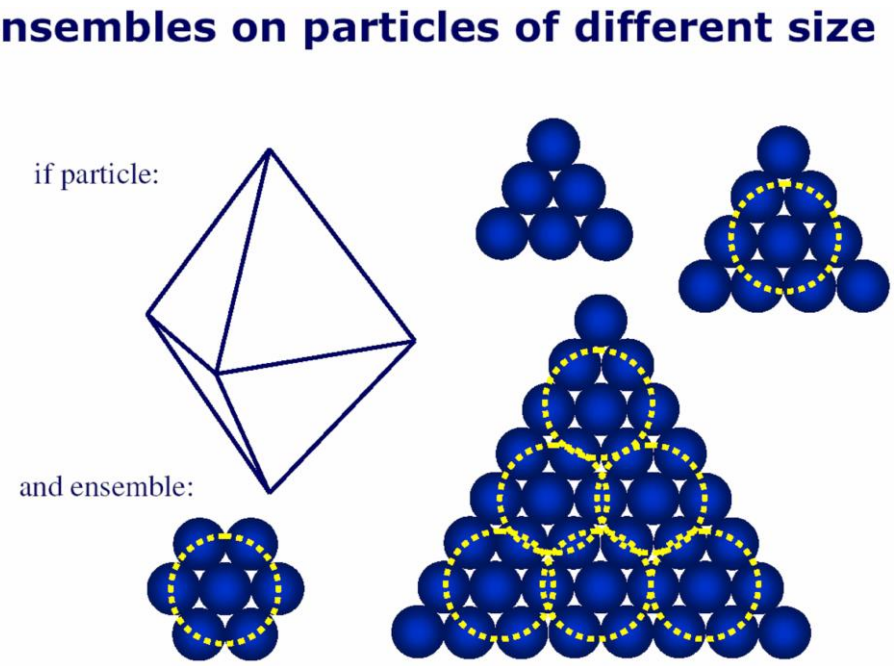

Figure 2.8: Schematic of 'The Ensemble Theory' (Niemantsverdriet et al., 1980)

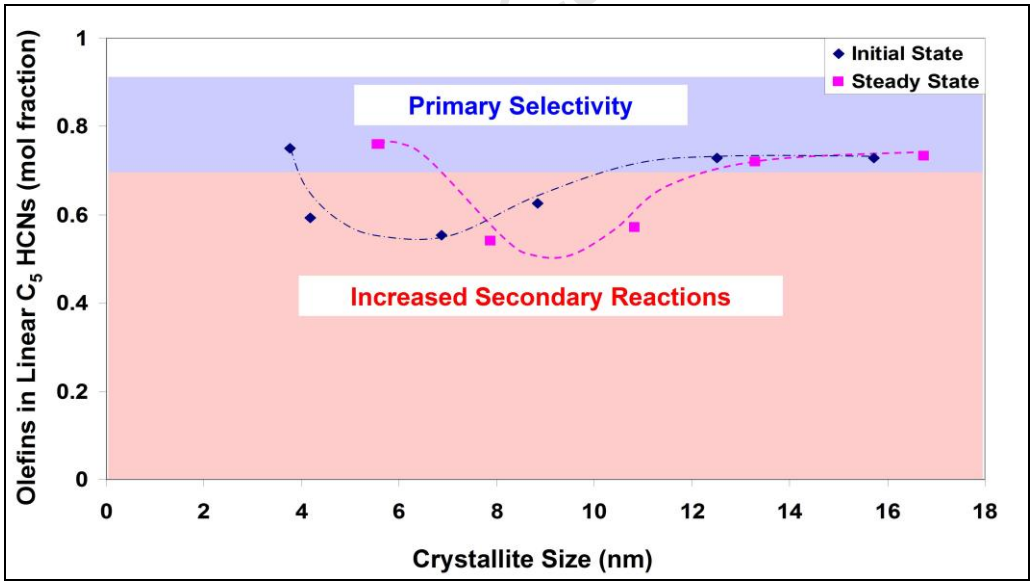

Figure 2.9: Olefin fraction as a function of Fe crystallite sizes (Cheang, 2009)

Furthermore, a decrease in the crystallite size resulted in increased paraffin to olefin ratios over supported cobalt (Bezemer et al., 2006) and ruthenium (Barkhuizen et al., 2006; Welker, 2007) catalysts. The authors suggested that increased relative hydrogen availability may cause this, in line with the increased methane contents

obtained on smaller crystallites. Alternatively, smaller crystallites may expose surfaces and sites that allow preferred secondary olefin reactions including hydrogenation (Welker, 2007). Work conducted by Hayashi et al. (2002) showed that as the iron crystallite size decreased (on a Fe/SiO_2 catalyst), the amount of oxygenates increased and the amount of methane decreased. No clear trends in this regard were obtained in studies dealing with supported iron crystallites of different sizes (Mabaso, 2005; Cheang, 2009).

While Mabaso's results may be clouded by effects of uneven potassium promotion, Cheang (2009) observed an anomaly in the production of linear olefins around the '7 nm' range when using unpromoted alumina supported iron crystallites (Figure 2.9). The author explained this anomaly to be a result of two opposing trends where the dominance of the crystallite atoms is different. This means that at the lower crystallite sizes the edge atoms prove to be dominant and there are less secondary reactions. Cheang (2009) observed that the trend is opposed to what has been viewed by previous authors (Schulz et al., 2002, Welker, 2007) as it has been expected that as the crystallite sizes decrease, there will be an increase in the number of edged atoms which in turn results in an increase in secondary reactions. However, it is also suggested that the flat area atoms are required for secondary reactions (Cheang, 2009). This means that '7 nm' crystallite sized atoms feel the effect of both, the edged and flat area atoms.

The other explanation put forward was discussed by Cheang (2009) and van Steen (2008) where the anomaly that was observed is a result of the electronic effects between the α-olefin and catalyst surface. The relationship is known to be a HOMO-LUMO (Highest Occupied Molecular Orbital – Lowest Unoccupied Molecular Orbital) interaction type. The smaller crystallite sizes are said to be less co-ordinated resulting in an increase in the localization of free electrons. This means that the Fermi energy level of these crystallites are lowered nearing the HOMO of the atom. The adsorption of the α-olefins is said to be a HOMO-LUMO process and different Fermi levels result in bond strength differences. The greater the energy differences

between the HOMO and LUMO energy levels, the weaker the bonding interaction resulting in weaker adsorptions.

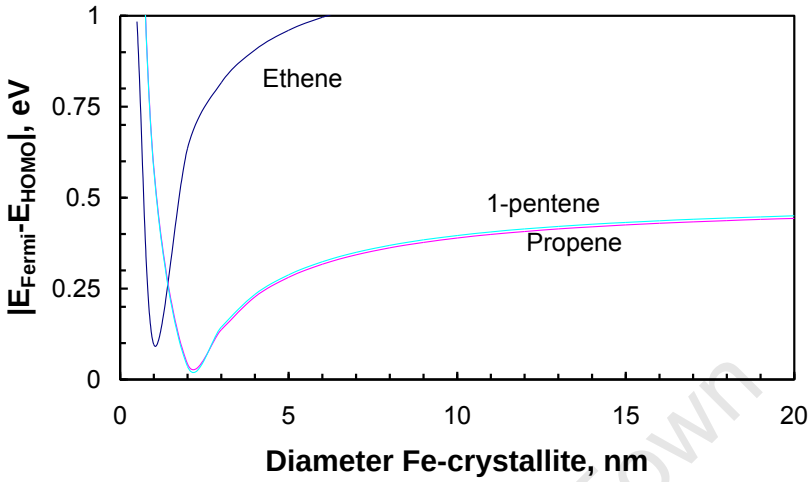

Figure 2.10: Olefin HOMO energy & Fe fermi level versus size (van Steen, 2008)

Figure 2.10 shows that the smallest difference in the HOMO and Fermi level (i.e. LUMO level) is around '3 nm' for the iron catalyst. This suggests that at this point, the bond strength of the metal and the adsorbing species (CO) is at a maximum. With regards to the phenomena observed by Cheang (2009), this interaction explains the behavior of the smaller crystallite sizes as they can easily (easier than the '7 nm' crystallites) re-adsorb the olefin to incur further reactions (van Steen, 2008; Cheang, 2009).

This provided the foundation of this research project where 3 sizes within the size range outlined in Cheang's and Mabaso's research (range of 2 to 16 nm) are synthesized and the successfully reduced catalysts are tested. However, in contrast to previous studies, this study utilizes unsupported crystallites in order to avoid any effects that may occur due to metal support interaction, which may vary with crystallite size. In further contrast to the studies by Mabaso (2005) and Cheang (2009), the reduction of the oxidic crystallites were to be studied using H_2 or CO, the latter potentially resulting in the corresponding carbides of different size.

2.3.5 Iron Catalyst Deactivation

Sintering

Sintering is said to have occurred if there is a structural change in the catalyst that results in the growth of small crystallites, normally resulting in a loss of active sites. The major factor that results in sintering is the temperature; meaning that the higher the temperature, the greater the sintering. There are other contributing factors such as promoters, catalyst pore sizes, supports, metal and the environment (species such as H_2O present) which could also accelerate the sintering of the catalyst (Forzatti and Lietti, 1999; Bartholomew, 2001; Dry, 2004). Moreover, smaller crystallites are believed to be more prone to sintering than larger ones. Effects of sintering during reaction studies can be minimized by using mild reaction conditions.

Phase Transitions

Phase transitions occur when the reaction between the vapor phase and the catalyst results in the occurrence of the transformation of the surface and bulk materials. This is known as the vapor-solid phase transitions. When active carbides are transformed into inactive carbides, this is known as the solid-state transition. It is possible for both these phase transitions to occur on the iron catalyst during the FT synthesis. Here, the formation of iron-oxides and carbides can occur which can even be inter-converted depending on the reaction conditions. The presence of water and carbon dioxide, for example, act as oxidizing agents resulting in undesired vapor-phase transformations (Forzatti and Lietti, 1999; Bartholomew, 2001; Dry, 2004; Ning et al., 2006; Pendyala et al., 2010).

Water Effects

Water is a major concern in the deactivation of the iron catalyst because if the water partial pressure in the FT reactor feed increases, the catalyst's rate of deactivation increases. This could be due to oxidation and/or hydrothermal sintering or kinetic inhibition effects caused by the water (Bartholomew, 2001; Dry, 2004). Due to the increased production of water down the reactor bed, there will be an increase in water content.

$$r_{CO} = \frac{m.P_{CO}.P_{H_2}}{(P_{CO} + a.P_{H_2o})}$$ Equation 2.2

Where $a = \frac{k_{H_2O}}{k_{CO}}$ (Dry, 2004)

The rate expression above (Equation 2.2) for iron provides an understanding of the water effects mathematically. It can be seen that an increase in the water partial pressure reduces the rate of reaction which decreases the conversion (Dry, 2004). A study conducted by Ning et al. (2006) showed that the oxidation of the Fe carbides by H_2O vapor results in Fe catalyst deactivation. Therefore, to reduce the water effects in fundamental studies, it is desired to carry out the experiments at low synthesis gas conversion (< 10%) (Cheang, 2009).

Poisoning

Poisoning occurs when an undesired species is adsorbed (chemisorbed) strongly on the surface and blocks the active sites needed for the catalytic reactions. In the case of iron; sulphur can be considered to be a poison. Although iron has a greater resistance to sulphur than the cobalt catalysts, sulphur is still known to cause poisoning in the FT synthesis when there are sufficient amounts present (Forzatti and Lietti, 1999; Bartholomew, 2001; Dry, 2004). The sulphur deactivates the iron catalysts quickly and the typical sulphur contents allowed in the iron-based Fischer-Tropsch process are less than 5 ppb in the syngas (Ferdous and Demirel, 2010). A schematic of how sulphur poisoning works is provided in Figure 2.11. The figure shows that the sulphur molecule chemisorbs onto the catalyst surface and blocks the adsorption sites hindering the adsorption of hydrocarbons and further reactions from taking place.

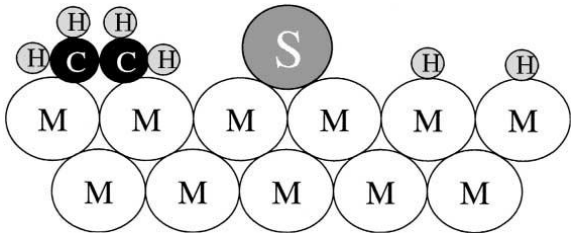

Figure 2.11: Sulphur poisoning model on a metal catalyst (Bartholomew, 2001)

Carbon Formation

This form of catalyst deactivation occurs when there is pore plugging or deposition of inactive carbonaceous compounds on the catalyst. The reactions between the syngas and the active catalyst sites are hindered by these compounds (graphite and amorphous carbon coke).

A study conducted by Pour et al. (2010) showed that there are three paths that occur in the deactivation of the iron catalyst. The three paths are as follows:

- The transformation from the adsorbed α-carbon to amorphous β-carbon and then to the graphitic δ-carbon
- The ξ-carbon concentrated surface is transformed to the more stable but less active χ and θ iron-rich phases
- The imbalance of CO produces graphite-like species (represented in Reaction 2.7)

$$2CO \rightarrow CO_2 + C_{(s)} \qquad \text{Reaction 2.7}$$

(Ferdous and Demirel, 2010; Pour et al., 2010)

2.4 *Catalyst Preparation*

2.4.1 Concerns

To obtain an accurate understanding and determine the precise effect of the various nano-crystallite sizes, it is necessary to obtain a narrow crystallite size distribution (Barkhuizen et al., 2006). A schematic representation of the desired nano-sized crystallite distribution is represented in Figure 2.12.

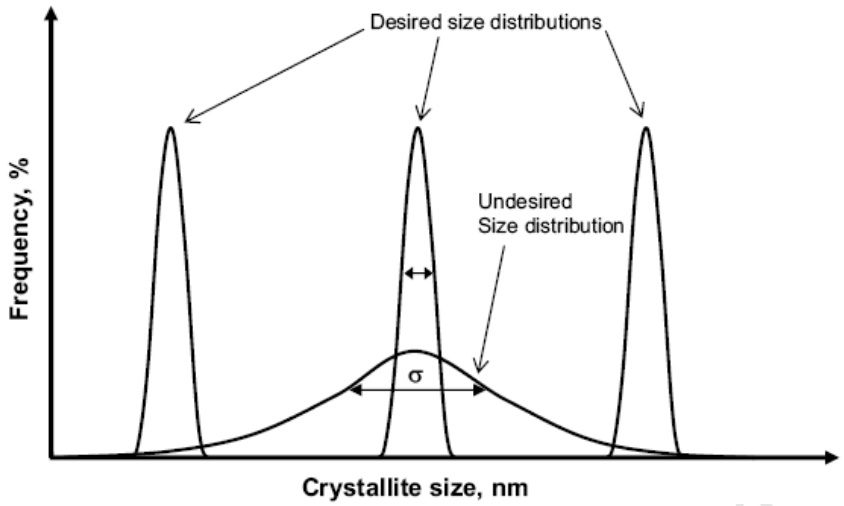

Figure 2.12: Desired size distribution of nano-sized crystallites (Mabaso, 2005)

2.4.2 Methods

Impregnation

This technique is considered to be the most commonly utilized catalyst preparation technique. It is a method that brings a support into contact with a solution of the active phase precursor. This is then dried; evaporating the impregnation solvent allowing the active phase to attach itself to the support's surface. Once the catalyst is distributed onto the support's surface, the catalyst is then converted to an active phase through a reduction process.

However, it is important to note that there are two different forms of impregnation; wet and dry impregnation. Wet impregnation is used when it is desired to have the active phase mainly on the surface of the support material and this is achieved by adding more of the active phase precursor than the support material's pore volume.

The other impregnation technique (dry impregnation) is usually utilized when friction is expected during the process which will result in the damage of the support's outer surface. This method is achieved when the amount of the active phase precursor added is equal to the pore volume.

The impregnation method is fast but it is difficult to prepare a catalyst with high loadings and narrow crystallite size distributions (Lensveld, 2003, Mabaso, 2005; van Steen, 2009).

Precipitation

In this process, the active catalyst's component in its salt form is dissolved (normally) in water to form a homogeneous solution. The pH of the homogeneous solution is then adjusted until the metal precipitates out of the solution. This process allows for higher loading of the active metals and provides narrow crystallite distributions, but variation of average crystallite size is generally difficult to obtain (Mabaso, 2005; van Steen, 2009).

Microemulsion Technique (Reverse Micelle Systems)

This process is used to obtain a much narrower distribution of the nano-sized crystallites; importantly it also presents a method to control crystallite size. It is a process whereby a thermodynamically stable system is created between a polar solvent, a non-polar solvent and an amphilic surfactant. The surfactant is a substance that consists of a non-polar end and a polar end. It allows for a link between the polar and non-polar solvents because the surfactants' polar end can bond to the polar solvent and the non-polar end to the non-polar solvent. These systems are temperature sensitive and it has been seen that the solubility of the surfactant in the water increases as the temperature increases. This temperature increase destroys the oil droplet and a decrease in the temperature destroys the water droplet (Schwuger and Stickdorn, 1995; Eriksson et al., 2004; Mabaso, 2005; Welker, 2007; Cheang, 2009).

A microemulsion system containing water as the polar solvent and oil as the non-polar solvent is shown in Figure 2.13.

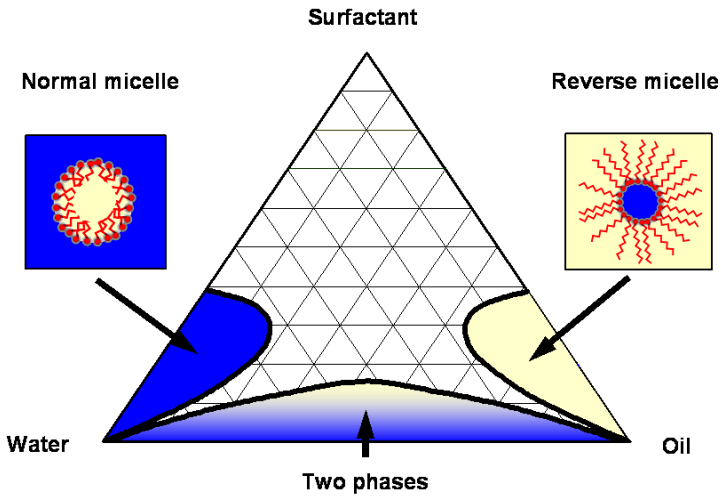

Figure 2.13: Phase diagram of surfactant-oil-water system (Mabaso, 2005)

When an aqueous solution incorporates a soluble metal salt, the nano-sized droplets can be used as nano reactors and precipitation or reduction of the catalyst precursor can be conducted therein. Importantly, the size of these 'nano reactors' and therefore the size of the resulting nano crystallites can be synthesized. When there is a decrease in the water to surfactant ratio, it is expected that smaller metal crystallites will be synthesized after precipitation (Schwuger and Stickdorn, 1995; Eriksson et al., 2004; Mabaso, 2005). This is expected as more surfactant is required to wrap more of the smaller water droplets (i.e. there is a greater total surface area of the droplet).

For the preparation of iron based nano crystallites, Mabaso (2005) and Cheang (2009) used iron nitrate in one reverse micelle system and a precipitating agent in a second reverse micelle system with the same water to surfactant to oil ratios. These were then combined and the micelles are then allowed to collide continuously; and precipitation took place. The precipitate was then washed, dried and calcined (in an Air/Air-Argon mixture) (Mabaso, 2005; Cheang, 2009). The supported catalyst can be produced by addition of a suitable support after the precipitation step. This collision process is represented in Figure 2.14.

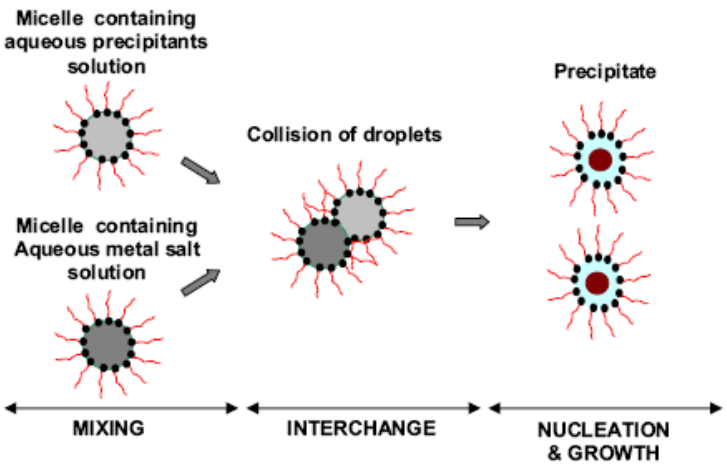

Figure 2.14: Crystallite formation mechanism from micro-emulsions (Mabaso, 2005)

This method is simple and provides the narrow nano-sized distribution desired in this study. Moreover, different crystallite sizes can be prepared. To obtain the information about whether the objective of catalyst preparation is achieved, it is necessary to analyze the catalyst and its products. The methods used to analyze the catalyst and its products are discussed in section 4.

This technique will be utilized in this research project to synthesize the desired nano-sized iron crystallites which will be studied in this FT investigation to determine the carbidisation of the various crystallites sizes and the effect of crystallite size on the FT activity and selectivity.

3 Aim, Objectives, Key Questions and Hypotheses

The main aim in this study is to advance the understanding of the carbidisation of nano-sized iron oxides crystallites of different sizes and the catalytic performance of differently sized iron carbides. This research project will look at preparing three nano-sized iron oxide crystallites with narrow size distributions. Phase change and composition analysis during reductive pre-treatment will be conducted (by means of in-situ XRD analysis) in order to provide a greater understanding of size dependent reduction or carbiding behavior. The focus is also to determine the Fischer-Tropsch activity and product selectivity as a function of the size of the crystallites formed. The key questions associated with this research project are:

- Will hydrogen reduction of unsupported nano-sized iron oxide crystallites result in the sintering of the crystallites (i.e. increase the crystallite sizes and distort the distribution)?
- Will CO reduction of unsupported nano-sized iron oxide crystallites result in the sintering of the catalyst (i.e. increase the crystallite sizes and distort the distribution)?
- Do the smaller sized crystallites transform to iron carbides at a faster rate than the larger crystallites?
- Does the size of the iron oxide crystallite have an effect on the type of phases formed during carbiding?
- Is there a decrease in the catalyst activity at lower iron carbide crystallite sizes?
- Will the CH_4 selectivity increase as the iron carbide crystallite sizes decrease?
- Will the crystallite size reduction affect the hydrocarbon products selectivity?

This research project's hypotheses are as follows:

Hypothesis 1

Hydrogen reduction of unsupported nano-sized iron oxide crystallites leads to sintering.

Hypothesis 2

CO reduction of unsupported nano-sized iron oxide crystallites does not lead to sintering.

Hypothesis 3

In analogy to other Fischer-Tropsch metals and metallic iron, Fischer-Tropsch activity will increase with increasing iron carbide crystallite size while methane selectivity decreases.

Hypothesis 4

The amount of olefin synthesized shows a minimum in the medium nano-sized crystallite class.

4 Experimental Methodology

4.1 Catalyst Synthesis Technique

The catalyst preparation method utilized in this research project is the reverse micelle technique which allowed the synthesis of narrowly distributed iron oxide crystallites, approximately 3 ('small'), 7 ('medium') and 15 ('large') nm.

4.1.1 Unsupported Iron Catalyst Synthesis

This research project requires for strict control on the size distribution of the various different sized crystallites. This is allowed by using the reverse micelle technique which requires the use of a ternary system (shown in Figure **4.1** below). The initial stage of obtaining the ternary diagram is to mix the surfactant and the oil. This is done in duplication, one set is for the precipitating agent and the other is for the iron metal precursor. Berol 050 (PEGDE, Penta-ethyleneglycol-dodecylether – Akzo Nobel) is utilized as the surfactant and n-hexane (Kimix, 98% purity) as the oil (Mabaso, 2005; Cheang, 2009).

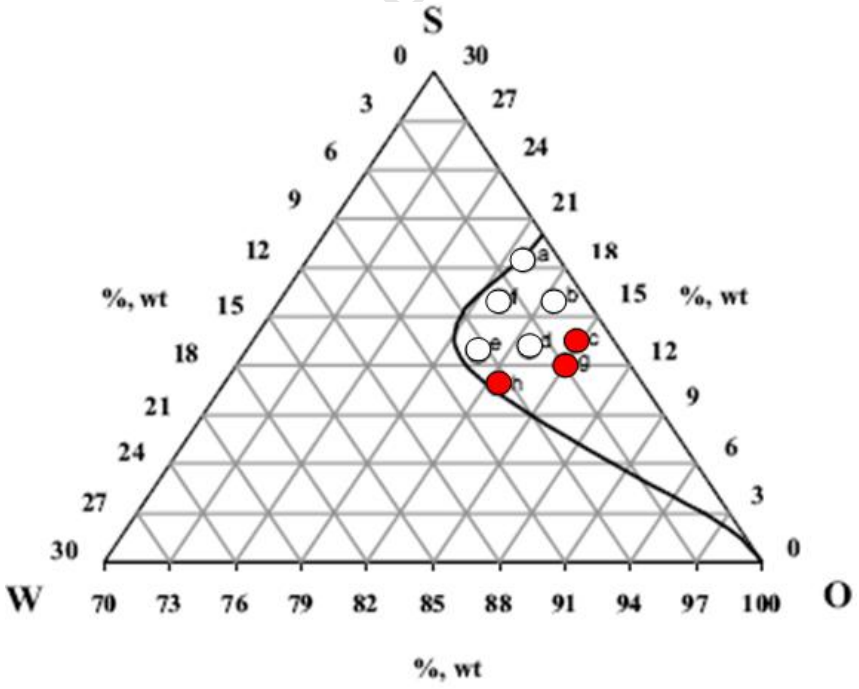

Figure 4.1: Ternary phase diagram of reverse micelle (water, Berol, n-hexane), indication of stability region and composition of reverse micelle systems used in this study (red circles) (Mabaso, 2005)

Once the excess Berol is filtered, the iron metal precursor, aqueous iron nitrate solution, (0.5M, $Fe(NO_3)_3.9H_2O$; Sigma-Aldrich, 99%) is added to the one set of the filtered solution and the precipitating agent (ammonium carbonate, 2M, $(NH_4)_2CO_3$; UniVAR, ex Merck-Saarchem, 30–34%) being added to the other filtered set. The molar concentrations (4:1 $\propto$ $[(NH_4)_2CO_3]$:$[Fe^{3+}]$) of the aqueous precursors were chosen to ensure quantitative precipitation (Mabaso, 2005). The metal precursor and precipitating agent reverse micelle systems are left to reach equilibrium and stabilize overnight before the reaction stage where the two ternary systems are combined (and stirred) for the precipitation to take place.

From the work conducted by Mabaso (2005), the sample micelles (a – h) shown in Figure 4.1 correspond to the following water-to-surfactant ratios with the concerned 3 sizes highlighted:

Table 4.1: Ternary system, water-to-surfactant ratios

Sample Micelle Letter	Ratio ($g_{aqueous}/g_{surfactant}$)
a	5:40
b	5:48
c	**5:58**
d	12:40
e	20:40
f	13:50
g	**9:35**
h	**20:33**

The desired crystallite size variation is obtained by keeping the amount of oil (n-Hexane) constant and varying the water-to-surfactant ratio. With a decrease in the water-to-surfactant ratio, the size of the micelles and therefore the size of the resulting crystallites will decrease as there will be more water droplets that can form when more of the surfactant is in the system. The water-to-surfactant ratios were obtained utilizing the stability region within the ternary diagram. This region was initially established by

Abrevaya and Targos (1987) and then by Mabaso (2005) to form the desired reverse micelles.

Table 4.2: Water-to-surfactant ratios used to yield desired sizes of iron oxide nano-crystallites (Mabaso, 2005)

$g_{aqueous}/g_{surfactant}$	Desired Size Ranges - d_{TEM} (nm)	Volume Based Size - d_{XRD} (nm)
5/58	2 ± 0.6	-
9/35	7.75 ± 1.6	7.1
20/33	15.7 ± 2.5	18.7

The water-to-surfactant ratio and the expected corresponding sizes (as obtained via TEM and XRD characterization according to Mabaso, 2005) of the resulting iron oxide crystallites (i.e. after drying and calcinations) are provided in Table 4.2. The table provides the water-to-surfactant ratios only for the sizes utilized in this research project which are also reflected on the ternary diagram in red. A ratio 5/58 suggests that there are 5 grams of the aqueous phase (iron nitrate or ammonium carbonate respectively) and 58 grams of the surfactant phase (Berol 050) with a constant mass of 250 grams of oil (n-Hexane) (Mabaso, 2005; Cheang, 2009).

The expected crystallite sizes are based on and are a replica of the work conducted by Mabaso (2005) and Cheang (2008). This research project required a scale up of the amount of catalyst produced, hence, the amount of the aqueous, surfactant and oil phases were increased appropriately. The details as to the reaction and calcination procedures are discussed in the following sections.

4.1.2 Micelle Reactions

The reaction process takes place in a 2 liter beaker where equivalent amounts of the iron and the precipitating agent reverse micelle precursors are combined. The color of the mixed micelles becomes darker indicative of the precipitation reaction to take place (the color is dependent on the desired size targeted) and it is left to react for 3 hours at 800 rpm in a rotary stirrer.

After the 3 hours, the reaction system is flocculated with acetone (Kimix, 99%) for approximately an hour while stirring. The addition of the acetone washes off the surfactant from the catalyst and the catalyst decants into fine particles suspended in the liquid. The next and most crucial process is the washing of the catalyst as this reduces the likelihood or severity of ignition of the catalyst in the calcination process. By reducing the ignition, which is due to excess surfactant which has not been washed off properly, there is less sintering that occurs which allows for better control of the crystallite size distributions. A schematic of the catalyst preparation process is being displayed in Figure 4.2 below:

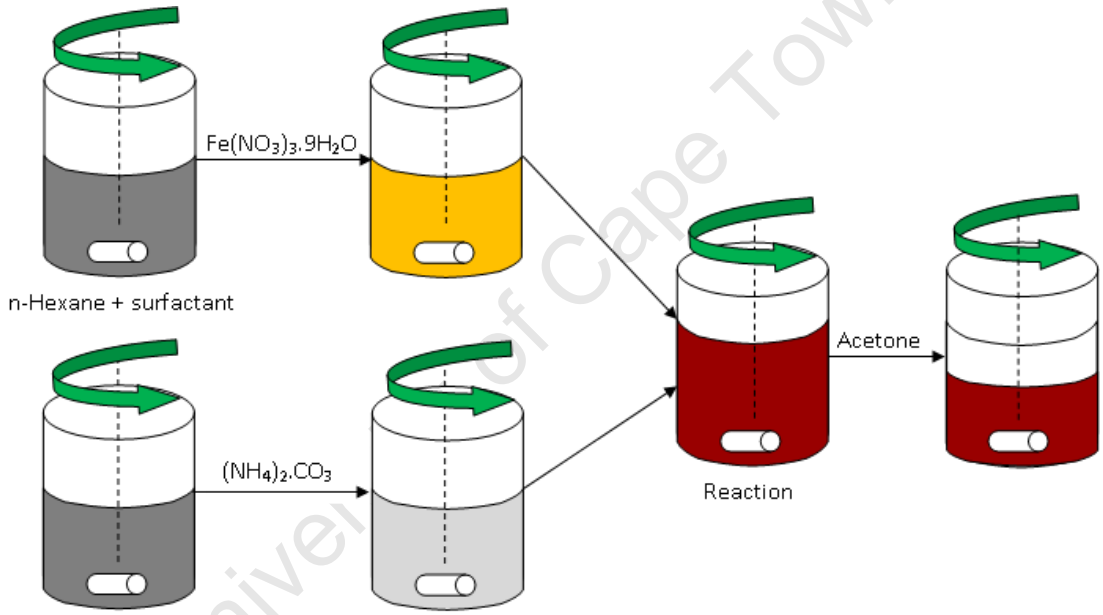

Figure 4.2: Catalyst preparation flow sheet

The precipitate is then left to dry in a fume cupboard at room temperature for 3 hours and then in a drying oven at 120°C for 12 hours. The material is then placed in a high temperature environment to form the crystallites (Mabaso, 2005, Cheang, 2009).

4.1.3 Calcination Procedures

The calcination step is a critical part of the crystallites' synthesis, whereby controlling this step will assist in controlling the final crystallite size distribution. By

restricting the ignition (due to residual surfactant) and runaway temperature of the catalyst, the sintering of the unsupported crystallites is minimized.

The standard procedure (Method 1) for the calcinations step is as follows:

- The precipitated material (iron hydroxides $FeO(OH)_x$) is placed in a fluidized bed reactor and air is allowed to flow (330 ml(NTP)/min·g) into the reactor tube until the bed is fluidized
- This calcination takes place at 300°C with a ramp of 1°C/min and left at 300°C for an hour
- During these calcinations, iron hydroxides are converted to iron oxides (Fe_xO_y)

For the lower crystallite sizes, an alternative calcination process was developed in order to reduce the amount of sintering of the catalyst. This was necessary as it was more difficult to remove the surfactant, which is also due to the fact that more surfactant was used in preparing this size faction. An observation was made that the calcination of the smaller crystallites (using Method 1) resulted in runaway temperatures. This procedure (Method 2) utilized an air/argon mixture, therefore allowing lower oxygen concentrations, and a modified temperature program for the smaller sizes which is outlined below:

- The material was heated from 25°C to 200°C with a ramp of 1°C/min with a composition of 40 ml(NTP)/min Ar and 60 ml(NTP)/ min Air
- At 200°C the air is increased from 60% to 100% air at a rate of 1 ml/min
- The temperature is then increased from 200°C to 250°C at 1°C/min
- Next, the system is kept constant at 250°C for 3 hours and then cooled to 25°C

4.1.4 Reduction Procedures

The reduction processes were conducted in the calcination or the FT reactor and in an in-situ XRD chamber. The former was done to prepare samples for subsequent TEM analysis, and the latter was done to characterize the phase and size changes during the reduction/carbiding procedure.

Reduction in the Calcination or the FT Reactor

The only type of reduction conducted in the calcination reactor was in an H_2 (Afrox, 99.999% purity) atmosphere because pure iron was to be initially utilized as the active phase. This reduction takes place at 300°C with a ramp of 1°C/min and then the system is kept at 300°C for an hour. The H_2 is flowed through the tube at a space velocity of 330 ml(NTP)/min.g. After the reduction, the samples were passivated in flowing CO_2 at room temperature in order to protect them from oxidation in air. CO treatment of samples for subsequent TEM analysis was conducted in the actual FT reactor (see section 4.2.1). Pure CO (Afrox, 99.5% purity) was used at the same space velocity of 330 ml(NTP)/min·g. The temperature program was as follows; the temperature was raised to 300°C with a ramp of 1°C/min and kept at this temperature for an hour. This is then cooled to room temperature in half an hour. However, further XRD analysis was conducted in order to obtain the final reduction temperature.

After this carbiding process the samples were again passivated under flowing CO_2 at room temperature and unloaded from the reactor for further analysis. For FT runs, the samples were treated in the same manner but the passivation step was only done after the actual FT experiment.

Reduction in in-situ XRD Chamber

Two different target temperatures were used to investigate the reduction behavior of the iron oxide nano-crystallites. The first target temperature (400°C) was used to determine the optimum reduction temperature (i.e. the second target temperature). The gas flows for hydrogen and carbon monoxide were kept constant at 132 ml(NTP)/ min with 0.4 g of sample loaded (space velocity of 330 ml(NTP)/min·g). All the temperature runs were started at 30°C with a ramp of 1°C/min. The final temperatures are mentioned next with the gases utilized for each specific setting.

- *Reduction to 400°C Settings*

  The XRD scan times were divided into 20 scans where scans 1 to 15 and 20 are run for 20 minutes with scans 16 to 19 being run for 1 hour and 25 minutes. During these scans the corresponding temperature was kept constant. The gases used with this configuration are hydrogen and carbon monoxide (Afrox, 99.5%).

- *Reduction to 350°C Settings*

  The XRD scan times were divided into 15 scans where scans 1 to 13 and 15 are run for 20 minutes with scan 14 run for 40 minutes. The gas used with this configuration is carbon monoxide.

After the XRD characterization, the sample passivation was conducted in 1% O_2 in N_2 (Air Liquide, 99.999%) for 1 hour at room temperature.

4.2 Fischer-Tropsch Experimental Set-up

4.2.1 Fischer-Tropsch Reactor Set-Up

The catalyst testing was conducted in a fixed-bed Fischer-Tropsch reactor following the experimental set-up shown in Figure 4.3.

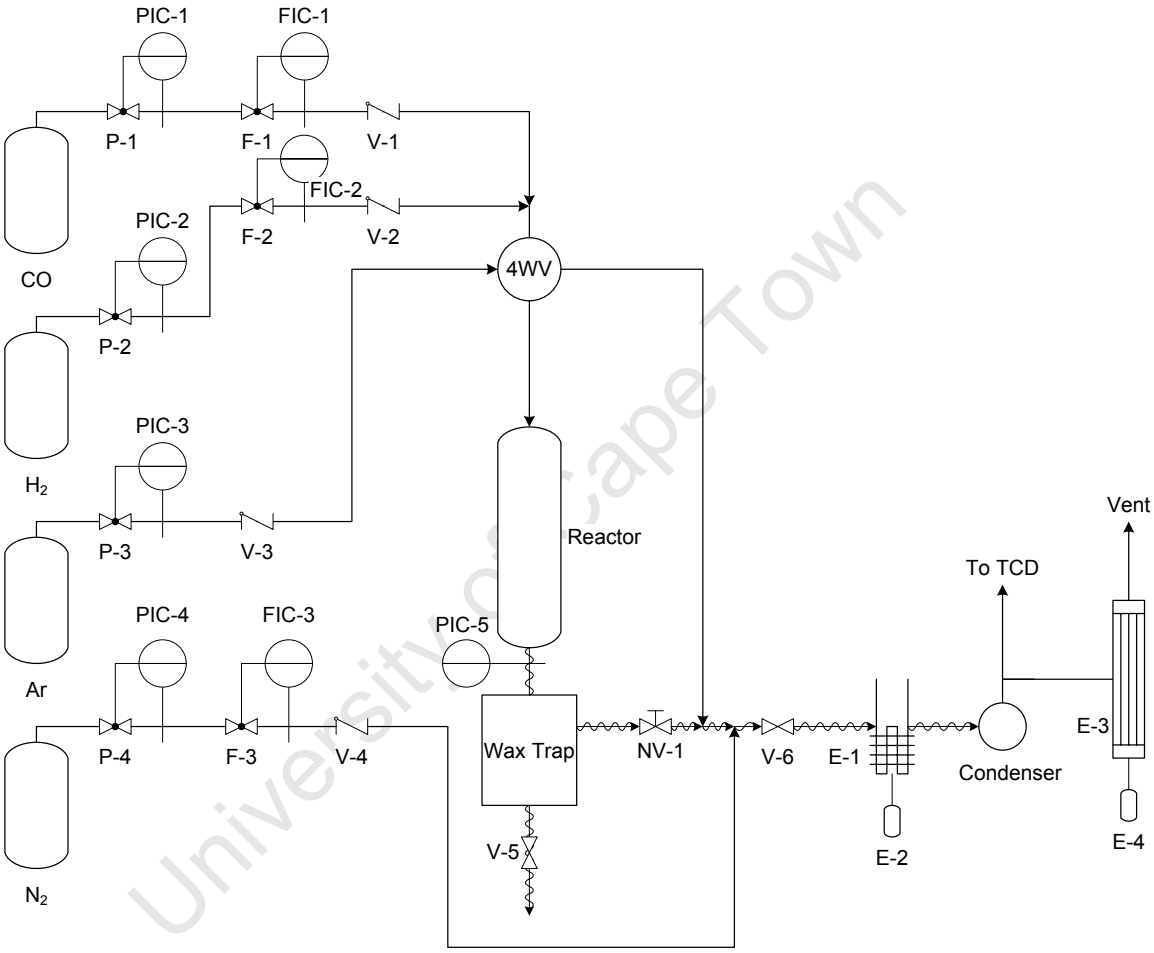

Figure 4.3: Fischer-Tropsch reactor set-up

The gases required for the reactions were all supplied in cylinders (with pressure regulators, PIC 1-4) using mass flow controllers (FIC 1–3, Brooks Instruments) to control the gas flow rates. Argon (Afrox, 99.999%) is used as a pressure control gas in this system. The gas lines were all fitted with on-off valves (V 1–4) and were tested for leaks regularly. The four way valve (4WV) is used to switch the gas flow between the reactor and the bypass. The outlet pressure gauge (PI-5) is used to

determine the reactor pressure. The reactor temperature is controlled by a temperature controller which uses a heating element wrapped around the reactor. This is insulated in order to keep the reactor temperature constant. The reactor exit lines are heated using heating wires so that the temperature could be maintained at no less than 180°C. The wax trap is heated to 180°C and was also insulated. An on-off valve (V-5) was used to remove the wax products.

N_2 gas is used as a reference gas for GC analysis and is fed directly into the reactor exit stream after pressure reduction, NV-1. The flow of the reactor exit stream, which includes the pressure controlled argon stream, is controlled by the needle valve (NV-1) and the product sampling is conducted using the ampoule breaker (E-2). A schematic representation of the ampoule breaker is shown in Figure 4.4.

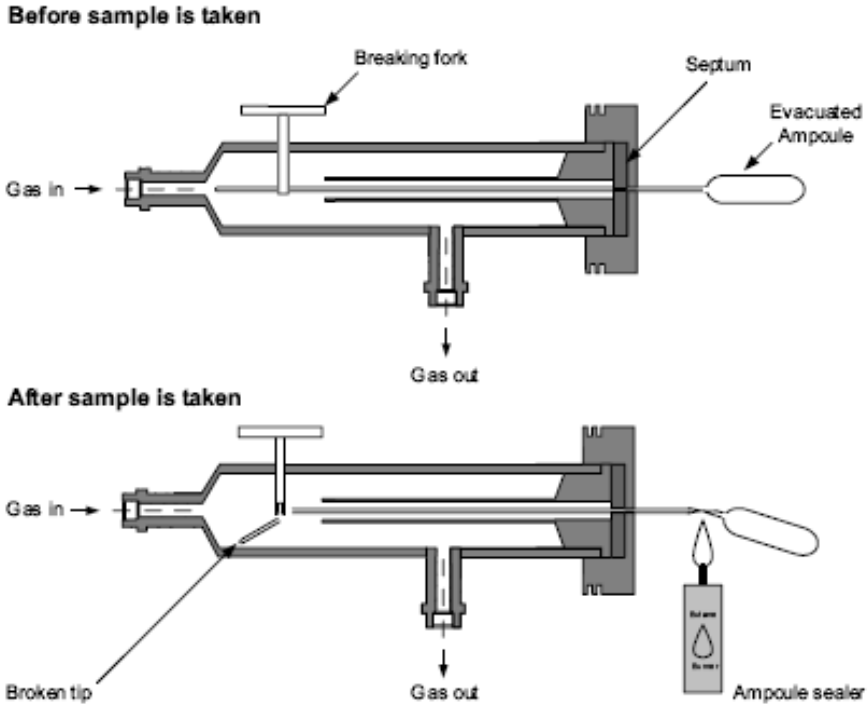

Figure 4.4: Ampoule sampling procedure (Mabaso, 2005)

After the ampoule breaker, there is a bubble flow meter (E-3) which indicates the flow in the exit stream and helps when sampling (explained further in section 4.2.4). All tubes and fittings were supplied by Swagelok.

4.2.2 Loading of Catalyst

The reactor is a fixed bed reactor (FBR) and a schematic of the reactor is shown below:

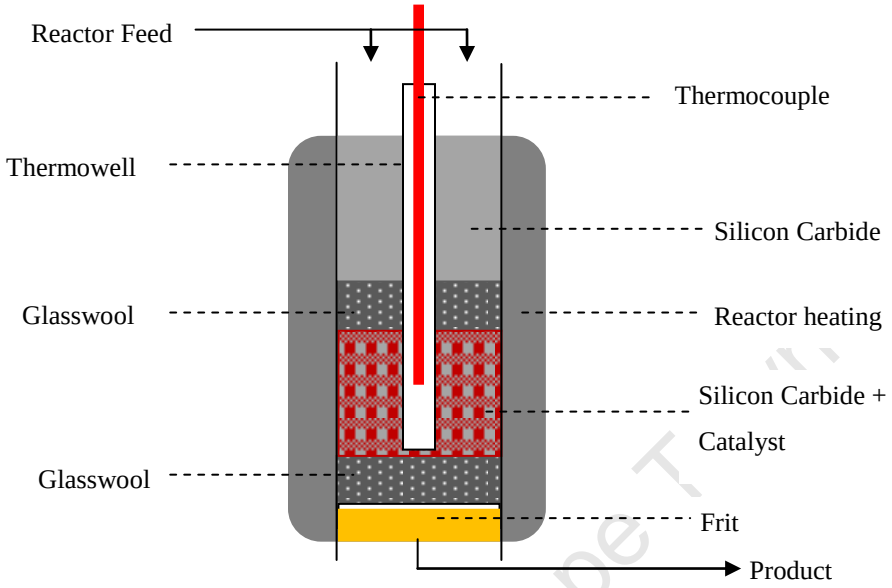

Figure 4.5: Schematic of fixed bed reactor for FT testing

The reactor is made of stainless steel (OD 12.5 mm, ID 9.5 mm) and it has a 3 mm thermowell placed inside which houses a movable thermocouple. The amount of catalyst and silicon carbide that was placed in the reactor is 0.12 g and 6.5 g, respectively. This was mixed well and iso-propanol was added to this mixture in order to distribute the catalyst evenly. The silicon carbide was utilized as it is an inert in the reactor and lowers the amount of heat released per catalyst volume due to its high thermal conductivity (Mabaso, 2005).

The frit is placed at the bottom of the reactor in order to plug the exit hole so the catalyst does not fall through. Glasswool (Silane coated) is then placed above the frit to act as the catalyst bed support. A thermowell is used to guide the thermocouple which is placed in the middle of the reactor. The catalyst is added carefully such that the thermowell is fully surrounded, with extra glasswool and silicon carbide being used to secure the catalyst from movement during the experiments. The feed to the

reactor enters at the top and the products leave at the bottom of the reactor (Mabaso, 2005).

4.2.3 Experimental Process

The Fischer-Tropsch tests were only done on samples which were pre-treated in CO (see section 5). For pre-treatment, the carbon monoxide control valve (V-1) and the four way valve (4WV) was opened to reduce the catalyst with the CO at 40 ml/min. The needle valve (NV-1) and on-off valve (V-6) is opened to the vent. The heating was programmed to increase the temperature to 350°C with a ramp of 1°C/min and the temperature is kept at 350°C for 1 hour. The heating program was then used to drop the temperature to 250°C (the desired reaction temperature). When the reaction temperature is obtained, the four way valve is changed to bypass.

The hydrogen control valve (FIC-2) is then opened to set the desired flows (i.e. to obtain the syngas ratio of 2) for the reaction. The H_2 flow rate was set to 40 ml(NTP)/ min and the CO rate was set to 20 ml/min. The N_2 gas (reference gas) was also then set at 40 ml(NTP)/ min using the FIC-3 flow controller. The system is then pressurized again by argon to 20 bars. A total flow of the product stream is controlled by the needle valve (NV-1) which is determined from the bubble flow meter (E-3). The chosen exit flow is 120 ml(NTP)/ min (Mabaso, 2005).

The flow rates are confirmed by using the micro-Gas Chromatograph (mGC) and bypass samples are taken until the flow rates and the syngas feed ratio of 2 is achieved. After ratio confirmation, the four way valve is switched to the reactor and the clock is started (i.e. the Fischer-Tropsch reaction process has begun). A stop watch is used to measure the length of the experiment and the sampling intervals.

The reaction is monitored via an online micro GC with Thermal Conductivity Detectors (TCD) (see section 4.2.4 for equipment conditions). N_2 is used as the internal standard to quantify the amounts of H_2, CO, CO_2 and CH_4. The online TCD sampling was conducted in the first 2 hours: the first hour, a sample was taken after

10, 30 and 45 minutes and after the second hour, every 30 minutes. Thereafter, sampling was only conducted every hour until the reaction time was complete (i.e. 5 hours). There were 3 samples taken during each sample time and results were averaged.

The organic products are collected in ampoules from the ampoule sampler. These collected products are analyzed using an offline gas chromatograph equipped with a Flame Ionization Detector (FID) (see section 4.2.4 for equipment conditions). The product was analyzed using a GC equipped with an FID (analysis duration: 45 min). The methane produced is utilized as the reference point for both, the TCD and FID, in order to link the results and determine formation rates of each compound (Mabaso, 2005; Cheang, 2009).

4.2.4 Product Sampling/Analysis

On-line Gas Chromatograph (GC) with a Thermal Conductivity Detector (TCD)

The instrument used for this analysis is the Varian CP-4900 Micro-GC and the detector temperature is set to 200°C. The relative errors for the TCD analysis are usually ± 3% (Mabaso, 2005). The following table provides the conditions at which the on-line thermal conductivity detector (TCD) was used.

Table 4.3: On-line gas chromatograph TCD conditions

Micro Gas Chromatograph Varian CP-4900	
Channel A	
Detector	Thermal Conductivity Detector (TCD)
Column Type	Molsieve 5Å PLOT
Carrier Gas	H_2
Analysis Temperature	80°C
Analysis Pressure	150kPa
Analysis Time	180s
Channel B	
Detector	Thermal Conductivity Detector (TCD)

Column Type	Pora PLOT Q
Carrier Gas	H_2
Analysis Temperature	60°C
Analysis Pressure	100kPa
Analysis Time	180s
Channel C	
Detector	Thermal Conductivity Detector (TCD)
Column Type	Molsieve 5Å PLOT
Carrier Gas	Ar
Analysis Temperature	80°C
Analysis Pressure	150kPa
Analysis Time	180s

The programming of the GC allows for data capture and analysis in automatic sequences. The TCD was calibrated regularly using a gas mixture of known composition (shown in Table 4.4). From the areas obtained in the analysis, the calibration factors (shown in Table 4.5) were normalized to the reference gas (N_2).

Table 4.4: Known gas mixture composition

Gas	mol-%
H_2	40.1
CO	20.0
CO_2	9.6
Ar	10.2
CH_4	14.9
N_2	5.20

Table 4.5: Calibration factors for TCD

Gas_i	Calibration Factor ($f_{TCD,i}$)
H_2/N_2	0.11 ± 0.003
CO/N_2	1.00 ± 0.030
CO_2/N_2	1.52 ± 0.030
Ar/N_2	0.99 ± 0.046
CH_4/N_2	1.10 ± 0.033

As seen in the tables, the on-line micro-GC is used to analyze the feed gases, as well as carbon dioxide and methane. Before an experiment, the syngas ratio is measured in reactor bypass mode as being:

$$H_2 / CO = \frac{A_{H_2} * f_{TCD,H_2}}{A_{CO} * f_{TCD,CO}} \quad \text{Equation 4.3}$$

The flow rates are obtained from the following equation:

$$\left(\frac{n_i}{n_{N_2}}\right) = f_{TCD,i} * \left(\frac{A_i}{A_{N_2}}\right) \quad \text{Equation 4.4}$$

$$n_{N_2} = \frac{x_{N_2} * v_{ref}(NTP)}{V_A} \quad \text{Equation 4.5}$$

n_i is the molar flow rate and A_i is the area of species i; x_{N2} is the molar concentration of nitrogen in the reference gas; V_{ref}(NTP) is the volumetric reference gas flow rate and V_A is the Avogrado volume. The gas conversion can be calculated from using the following equations:

$$X_{H_2} = \frac{n_{H_2,IN} - n_{H_2,OUT}}{n_{H_2,IN}} \quad \text{Equation 4.6}$$

$$X_{CO} = \frac{n_{CO,IN} - n_{CO,OUT}}{n_{CO,IN}} \quad \text{Equation 4.7}$$

A relatively high space velocity was applied in order to ensure low conversion levels as to minimize possible oxidative effects due to H_2O and CO_2 formed.

Off-line Gas Chromatograph (GC) with a Flame Ionization Detector (FID)

The instrument utilized for the analysis of organic compounds is a Varian CP-3800 GC. The relative error for the FID is typically ±1% (Mabaso, 2005).

Table 4.6: Off-line gas chromatograph FID conditions

Gas Chromatograph Varian CP-3800	
Detector	Flame Ionization Detector (FID)
Column Type	Capillary Column, Varian, 5CB (25m x 0.25 mm, d_f = 2.0 μm)
Detector and injector temperature	250°C
Ampoule Breaker Temperature	200°C
Injector	Split injector
Carrier Gas	H_2
Coolant	CO_2
Temperature Program	
Program	-55°C, 1.5 min isothermal Increased to 280°C
Duration of analysis	45 min

The product samples are collected in the vapour phase in heated glass ampoules (discussed in section 4.2.1). The tubular end of the ampoule is placed in the ampoule breaker (E-3) through a septum. Some of the products stream gas is drawn into the ampoule when the breaking fork breaks the tube. A butane flame is then used to seal the ampoule. An ampoule crusher next to the GC is used to crush the sample ampoules and the product gases are introduced to the split injector of the GC (see GC chromatogram example in Appendix D).

Table 4.7 shows the equations utilized to obtain the various desired yields and selectivities. Once the product flow rates are calculated, the selectivity's and yields are obtained utilizing equations 4.8 to 4.10 (Cheang, 2009).

Table 4.7: Yield and selectivity equations (Mabaso, 2005; Cheang, 2009)

Equation	**Information Determined**	**Equation**
$Y_{i,C} = \frac{n_{i,out}}{n_{CO,in}}$	Yield of i	4.8

$S_{i,C} = \frac{Y_{i,C}}{X_{CO} - Y_{CO_2}}$	Selectivity of i	4.9
$S_{CO_2,C} = \frac{Y_{CO_2,C}}{X_{CO}}$	CO_2 Selectivity	4.10

The rate of formation of Fischer-Tropsch products can be determined as follows:

$$r_{FT} = \frac{n_{CO,in} - n_{CO,out} - n_{CO_2}}{SA_{total}} \qquad \text{Equation 4.11}$$

Where:

$n_{CO,in}$ is the molar flow rate of carbon monoxide into the reactor; $n_{CO,out}$ is the molar flow rate of carbon monoxide leaving the reactor; n_{CO_2} is the molar flow rate of carbon dioxide leaving the reactor and SA_{total} is the total crystallite surface area.

The SA_{total} can be determined as follows using the equations shown in Table 4.8 (Cheang, 2009). The reduced catalysts' TEM average diameter values are utilized for the following calculations with the sample mass (m_{Fe}) being kept constant at 0.12 grams as mention in section 4.2.2.

Table 4.8: FT rate supporting equations (Mabaso, 2005; Cheang, 2009)

Equation	Information Determined	Equation
$V_{Crystal,Total} = \frac{m_{Fe}}{\rho_{Fe}}$	Volume of all crystallites	4.12
$V_{Crystal} = \left(\frac{1}{6}\right) * \pi * d^3$	Volume of single crystallite with diameter d	4.13
$N_{Crystals} = \frac{V_{Crystals,Total}}{V_{Crystal}}$	Total number of crystallites in sample	4.14
$SA_{Crystal} = \pi * d^2$	Single crystallite surface area	4.15
$SA_{total} = SA_{Crystal} * N_{Crystals}$	Total crystallite surface area	4.16

Formation rates of individual organic products analyzed using FID detection can be determined as follows:

$$n_i = \left(\frac{f_i * A_i}{f_{CH_4} * A_{CH_4}} \right) * \left(\frac{CN_{CH_4}}{CN_i} \right) * n_{CH_4} \qquad \text{Equation 4.17}$$

Where:

f_i is the response factor of substance i (explained in Equation 4.18); A_i is the peak area of substance i obtained from the FID chromatograph; CN_i is the carbon number of substance i; n_{CH_4} is the molar flow rate of methane obtained from the TCD.

$$f_i = \frac{N_{C,i}}{N_{C,-O} + 0.55(N_{C,C-O})} \qquad \text{Equation 4.18}$$

Where:

$N_{C,i}$ is the total number of carbon atoms in the substance; $N_{C,-O}$ is the number of carbon atoms not bonded to an oxygen atom (≈ 1); $(N_{C,C-O})$ is the number of carbon atoms bonded to an oxygen atom (≈ 0.55) and a carbon atom attached with a double bond to oxygen has no response $(N_{C,C=O})$ (Kaiser, 1969).

The Anderson-Schulz-Flory distributions were utilized to determine the chain growth probability. The mol% is obtained from the following equation (Cheang, 2009).

$$mol\% = \frac{\left[\frac{A_i * f_i}{N_i} \right]}{\sum \frac{A_i * f_i}{N_i}} \qquad \text{Equation 4.19}$$

The logarithmic plot of the mol % as a function of the carbon number will result in the modified plot shown in Figure 2.2. The chain growth probability (α) is obtained (from the slope) as it is equal to the logarithm of α shown in equation 2.1.

4.3 Catalyst Characterization

4.3.1 Transmission Electron Microscopy (TEM)

4.3.1.1 Standard Transmission Electron Microscopy (TEM)

The crystallite size distributions, average weighted size and the shape of the crystallites at their different states, i.e. oxidic, reduced and spent, were obtained from utilizing the LEO 912 OMEGA Transmission Electron Microscope (TEM) operated at 120 keV. The TEM short focal magnification range is from 3,125x to 500,000x and long focal magnification range is 80x to 2,000x. Two catalyst preparation techniques are available to prepare the metal catalyst: the solvent and slicing technique.

This slicing method required the samples to be placed initially in a vial with a liquid resin. The resin is left in an oven at 60°C for 48 hours and then it is cut into very thin slices (within the nanometer range) using an Ultramicrotome LEICA cutting machine.

The slices are then transferred to a carbon coated copper grid. The copper grid is then covered with formvar (also known as polyvinyl formal), support film for grids, to prevent crystallites from falling off the copper grid and the contamination of the condenser. Before analysis, the samples are allowed to dry in air at room temperature.

The solvent method first allows the crystallites to be suspended in methanol to disperse the particles; then transferred to the carbon coated copper grid and finally dried before using it in the TEM chamber.

The analysis of the TEM data for crystallites size determination was conducted utilizing the ImageJ processing software (ImageJ, 1997). To determine the mean volume diameter of the crystallite's distribution, $đ_{cv\text{-}TEM}$ is calculated using the

equation 4.20. This equation will allow for comparison with the results obtained from the XRD data.

$$d_{c,v-TEM} = \frac{\sum n_i d_{c,1-TEM}^4}{\sum n_i d_{c,1-TEM}^3} \qquad \text{Equation 4.20}$$

đ$_{cv\text{-}TEM}$ is the number or length based crystallite diameter as directly obtained from TEM micrographs. To obtain statistically relevant information, a minumum of 300 (n = 300) crystallite were measured from the ImageJ pictures (Bergeret and Gallezot, 1997).

4.3.1.2 High Resolution Transmission Electron Microscopy (HRTEM)

The instrument used for HRTEM was a Philips Tecnai F20 FEGTEM (Field Emmission Gun TEM) and relative to the standard TEM, it allows for higher resolutions. This machine was operated at 200keV and has an extremely high-resolution imaging and characterisation analysis feature (FEI Company and Philips, 1999).

4.3.2 X-Ray Diffraction (XRD)

4.3.2.1 Standard X-Ray Diffraction (XRD)

The weighted crystallite sizes and crystallite phases were determined using the Bruker D8 Advance X-Ray Diffractometer (XRD). In this instrument, a cobalt radiation source (Co; Kα 1.7889Å) is used to generate high voltage X-rays. The instrument consists of a Theta-Theta assembly; a position sensitive detector (PSD) and 9 position sample changer.

The mathematical model that represents the generated diffractograms (usually displayed as wavelength versus 2θ) is shown in equation 4.21.

$$\lambda = 2d_{hkl}\sin\theta \qquad \text{Equation 4.21}$$

This is known as Bragg's law and is normally used for crystalline structures due to the atoms being placed in parallel planes. λ is the wavelength of the radiation source

and is constant; d_{hkl} is the distance between the parallel planes providing the diffraction data and θ is the specific angle observed at each atomic position (Niemantsverdriet and Chorkendorff, 2003; Birkholz, 2006). A schematic of this process is shown in Figure 4.6.

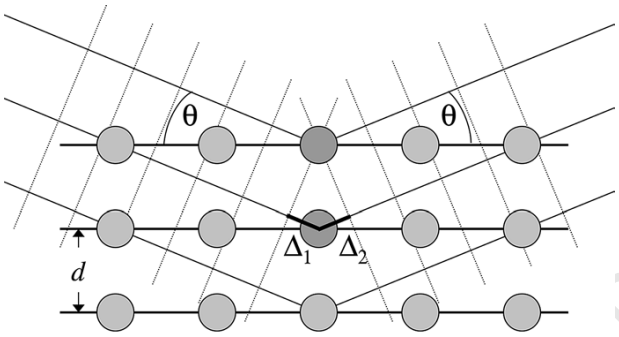

$$\Delta_1 + \Delta_2 = 2d\cos(90° - \theta) = 2d\sin\theta$$

Figure 4.6: Bragg equation visualization (Birkholz, 2006)

There are various uses for the XRD as it allows for the determining of the phase compositions, unit cell parameters, crystallite structure and size. The phase compositions are determined by referencing each component's relative peak intensities. The relative composition of the phases can also be calculated with Rietveld refinement using the Topas-4 program (du Plessis, 2009).

For analysis, the samples are placed in sample plate holders and the powder is loaded on the top of the holder. The sample is pressed into the holder and the surface is kept smooth as certain problems can arise which could result in preferred orientation (non-random distribution of the crystallites) (Scintag, 1999; Niemantsverdriet and Chorkendorff, 2003; Birkholz, 2006).

The peaks are matched with an X-ray diffraction peak database, Topas-4 Structural Database. Since each scan provides a distinct 'fingerprint' of the sample being analyzed, the phases present in a sample can be identified. Once the sample is identified, then the average weighted crystallite sizes are obtained from the Debye-Scherrer equation (equation 4.22).

$$D_{P,XRD} = \frac{0.94\lambda}{\beta_{1/2}\cos\theta}$$ Equation 4.22

Where: $D_{p,\,XRD}$ is the mean volume diameter of the crystallite; β is the compound's major peak broadness and θ is the angle at the maximum point of the peak (Niemantsverdriet and Chorkendorff, 2003; Birkholz, 2006). The schematic (Figure 4.7) below shows a graphical representation of how the peak broadness (used in equation 4.23) was obtained.

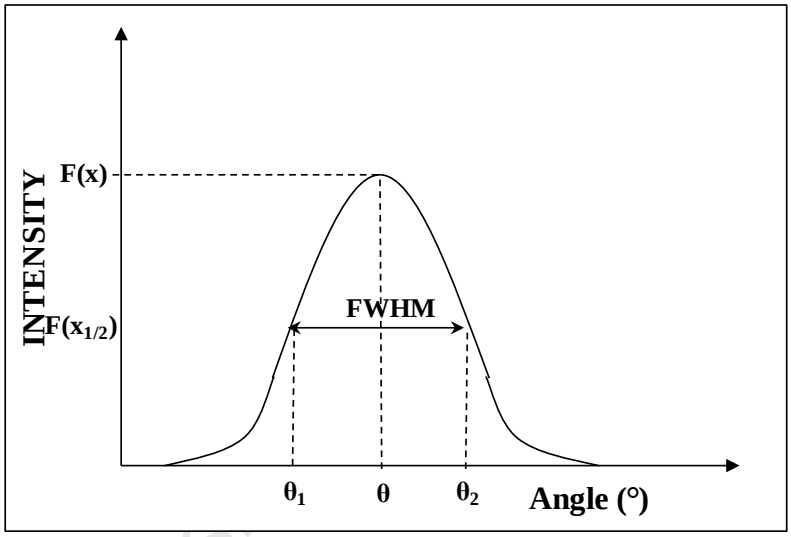

Figure 4.7: Full-width half maximum schematic representation

The following equation is used to consider the instrument broadening error by taking into consideration the broadness of a reference sample that has the least preferred orientation. In this study, corundum was used as the broadness reference sample and the actual $\beta_{1/2}$ is calculated from equation 4.23 below:

$$\beta^2_{1/2} = \beta^2_{sample} - \beta^2_{korundum}$$ Equation 4.23

Using Bragg's law; the Debye-Sherrer equation and the full width at half maximum technique; the average weighted crystallite size of a phase is calculated. All non in-situ scans were completed in an hour.

4.3.2.2 In-Situ XRD

The Bruker D8 Advance XRD instrument allowed for an in-situ chamber to be mounted on it (XRK 900, Anton Paar; Figure 4.8). The following gases were connected to the cell: O_2, N_2, CO & H_2 and the cell design is such that these gases flow through the samples as it rotates. The system temperature (maximum of 900°C) could be programmed and linked to the XRD scans. This set-up is used to study the behavior of the nano-crystallites, under a controlled environment, i.e. under flow of H_2 or CO. Based on these studies, reactions conditions were chosen for the samples that were in the FT reactor set-up. No FT experiments could be conducted in this set-up as the formation of hydrocarbons and water can contaminate the cell.

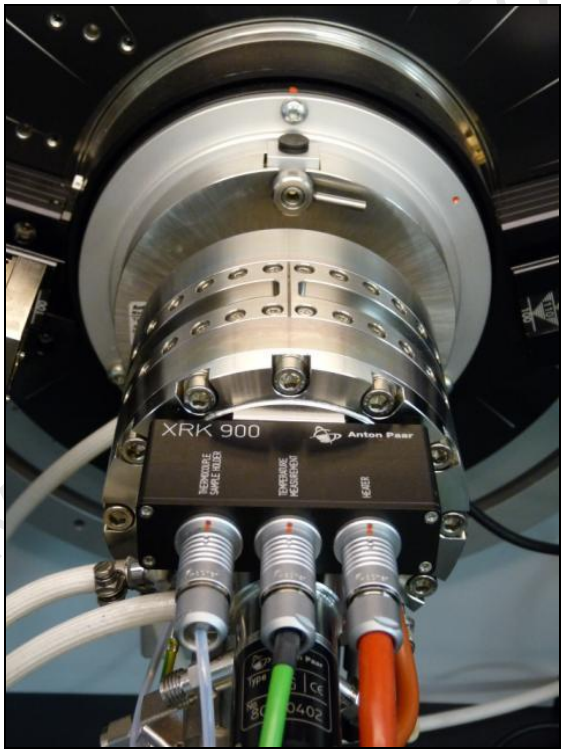

Figure 4.8: Picture of in-situ XRD chamber

The settings used on the XRD instrument are shown in Table 4.9.

Table 4.9: TEM Bruker D8 advance characteristics

Settings	Value
Diffractometer Type	D8
Goniometer Diameter	500 mm
Primary Soller Slit	4°
Tube Element	Cobalt (Co)
Generator Voltage	35 kV
BEAM Optics	
Divergence Slit	1.0°
Antiscattering Slit	0.5°
Scan angles (2θ)	20° to 85°

4.3.2.3 Topas-4

Topas-4 (supplied by Bruker AXS GmbH) is a tool utilized in analyzing XRD scans by fitting the scan mathematically according to the contribution of the different crystalline phases present and provides, inter alia, the following useful information (Bruker, 2008; du Plessis, 2009):

- Crystallite sizes and composition
- Rietveld structure analysis
- Refinement models for peak broadening, shifts, temperature and preferred orientation
- Fit error calculations and peak de-convolution
- Amorphous phase quantification

Due to peak broadening, a corundum sample was initially utilized as the base scan for the analysis of the catalyst XRD results. This sample is used to establish the optimum instrument correction settings by determining the functions that will fit the sample XRD profile. The Gaussian and Lorentzian functions are used for the crystallite size and the full width half maximum strain calculations are convoluted into the peak. The Hat function is utilized to incorporate the detector slit into the

convolution of the peaks and the Axial Divergence functions are integrated by using the Circles function (Bruker, 2008; du Plessis, 2009).

Each sample's XRD scan (in Topas-4) was used to replace the settings used in the corundum scan keeping the optimum convolution and instrumental settings. The Topas settings and optimum convolution functions are shown in Appendix A.

4.3.3 Nano Surface Electron Microscopy (NanoSEM)

The Nova NanoSEM instrument (FEI Company) was used to view the surface and morphology of the crystallite particles and to obtain the average particle size. This characterization technique also allows for the elemental analysis of the material using an EDX detector. The field emission gun SEM (FEGSEM) instrument can magnify the image up to 500 000x resulting in ultra-high resolution. The detector used is known as Oxford X-Max and the software is called Inca. The equipment has the following instrumental specifications:

- In-lens immersion detector
- Low vacuum secondary and back scatter electron (BSE)

The in-lens part of the detector is placed in the chamber that emits the electrons onto the sample's surface and deflects the electrons directly into the chamber. This allows for more electrons to be captured after impact with the sample and provides a better image. The immersion component of the detector allows for obtaining high resolution images by using a magnetic field to trap most of the electrons that the sample emits and send them into the chamber (Dufek, 2008).

To prepare the sample, the catalyst is sprayed on glue-like paste which is placed on a plastic/metallic sample holder with some carbon paste on top. The sample images are taken at a High Voltage of 19 kV; Working Distance of 5.5 mm and a scale of 200 nm (Dufek, 2008).

4.3.4 Mössbauer Spectroscopy

To analyze the phases of the CO reduced and spent catalysts Mössbauer Spectroscopy was utilized. This technique, which is complimentary to XRD analysis, is named after the discoverer, Rudolf Mössbauer, and the Mössbauer effect is obtained from the sample's nuclear absorption, depending on the recoil absorption and emission, of gamma (γ) rays (Seidel, 1967; Fisher and Barron, 2009). This characterization technique is utilized because the gamma rays provide greater energy levels (and shorter wavelengths than the x-rays) that allows for a deeper analysis of the metal crystallites. This will allow us to observe whether there are any phases present on the catalyst surface that were not observed by the X-ray Diffraction equipment.

When exposing a sample to a γ-ray source, the atom nucleus will either absorb or emit those γ-rays in order to allow the nucleus to stabilize. The nuclear transition is considered to be the stable energy point of the nucleus and when the energy of the γ-rays interrupts this transition, the recoil energy (absorption or emission) can be calculated. This is mathematically represented below (Fisher and Barron, 2009):

$$E_{recoil} = E_{Nuclear\_Transition} - E_{\gamma - ray} \qquad \text{Equation 4.24}$$

The spectral data were collected at room temperature over an approximate velocity of ±12 mm/s. These spectra are analyzed utilizing a spectrum modeling program called "Normos" which uses least squares to plot a quadruple doublets and sextets based on a Lorentzian model profile (Cheang, 2009; Fisher and Barron, 2009).

The crystalline phases are identified by matching these unique profiles with the specific adsorption features of various doublets and sextets. This matching is conducted through the matching of the profiles' on the isomer shift (δ), quadruple splitting (Δ) and magnetic hyperfine field (B_{hf}). The quantification of the phases was obtained from the absorption spectral area. The reference (metallic iron, α-Fe) spectrum was used by calibrating the velocity scale and the isomer shift values relative to the sample's spectra (Cheang, 2009; Fisher and Barron, 2009).

5 Results and Discussion

5.1 Uncalcined Catalyst

An uncalcined sample of the large iron oxide crystallites is analyzed using the XRD and TEM characterization techniques to understand whether the crystallites form before or after the calcination step.

XRD Analysis

The X-ray diffractometer was utilized to determine the phase of the uncalcined catalyst and the result is that the catalyst appears as the Goethite phase (FeO(OH)). Since the catalyst is not in crystalline form, it was not possible to determine any particle sizes. When the background is removed, the XRD scan looks almost flat. The x-ray scan is shown in Figure 5.1.

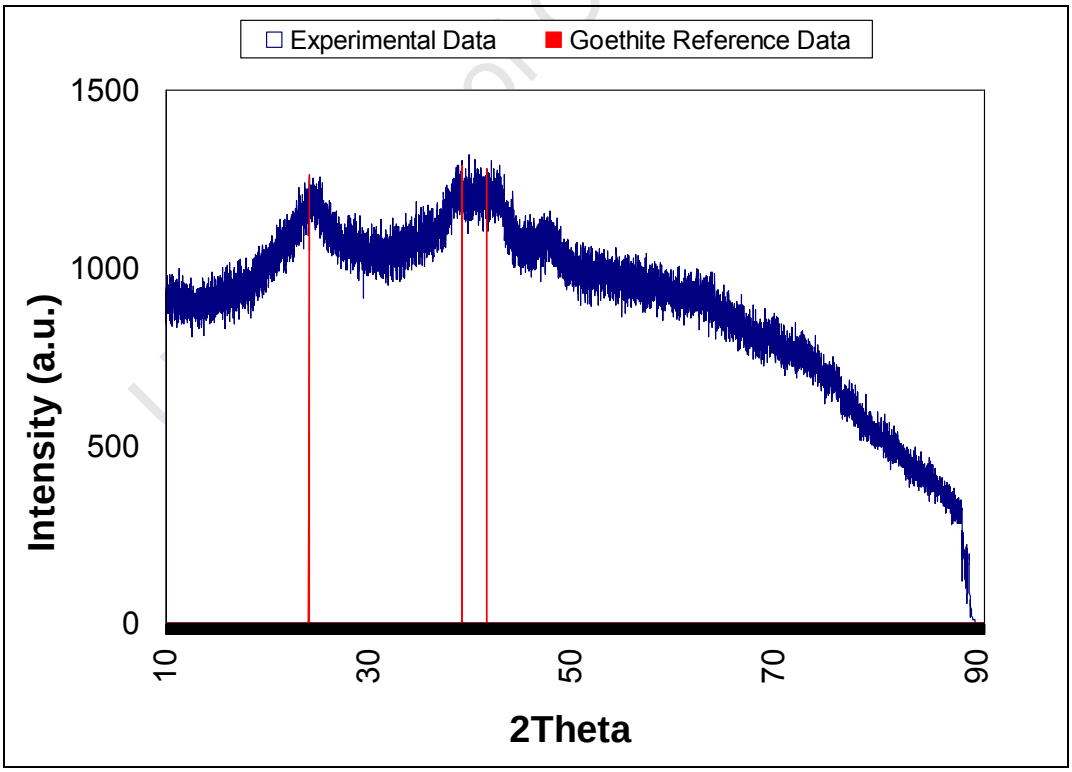

Figure 5.1: XRD scan of uncalcined sample (dried at 120°C, 12 hours)

TEM Analysis

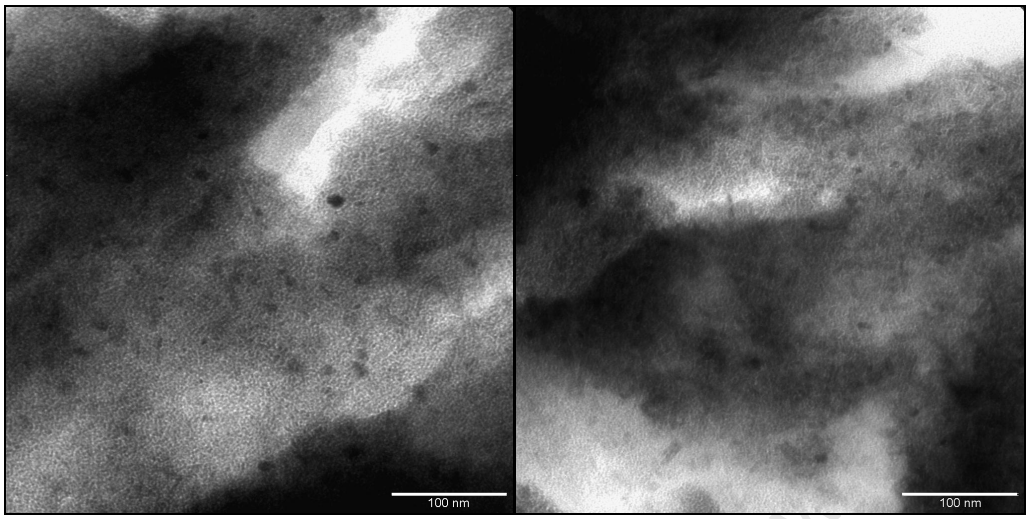

Figure 5.2: TEM pictures of uncalcined sample (dried at 120°C, 12 hours)

Representative TEM images of the uncalcined sample are shown in Figure 5.2. It can be seen that the uncalcined material indeed appears to be largely amorphous.

5.2 Calcined Catalyst

After the calcination process (small crystallites: 250°C; medium and large crystallites: 300°C), the catalysts were analyzed using the XRD, TEM and NanoSEM characterization instruments. However, the first observation recorded is the recovery of the material (on an iron basis) from the reverse micelle preparation technique, i.e. after calcination.

5.2.1 Catalyst Recovery

Table 5.1: Averaged recovery results of reverse micelles

Size Class	Mass (g)	% Recovered
Small	0.67	32
Medium	1.17	39
Large	1.44	42

Several batches were synthesized and Table 5.1 provides the average amount of catalyst that was recovered. It can be seen that it is easier to recover from the larger

micelles than the smaller micelles. This is because the smaller catalyst particles are lighter and suspended in the acetone much more than the larger catalysts which make it more difficult to decant the acetone without losing the catalyst.

5.2.2 XRD Analysis

The phases obtained in the calcined samples are the hematite (α-Fe_2O_3) and maghemite (γ-Fe_2O_3) phases for all the crystallite sizes. The following figure and table (Figure 5.3 and Table 5.2) show the XRD scans (with the major peaks associated to their respective phases) of the various anticipated crystallite sizes (based on Mabaso's study) with the average crystallite sizes obtained using the Scherrer equation from measuring peak widths and Topas calculations; the latter also yielded the phase composition of the samples.

Table 5.2: XRD and topas results of calcined samples

Size Class	XRD FWHM (nm)		Topas Phase(s), Sizes (nm) and Percentages		
	γ-Fe_2O_3	**α-Fe_2O_3**	**γ-Fe_2O_3**	**α-Fe_2O_3**	**Rwp ***
Small	7.7	4.8	7.9 ± 0.1 (98 wt-%)	4.0 ± 0.4	8.92
Medium	11.6	7.7	11.3 ± 0.4 (94 wt-%)	14 ± 0.4	9.39
Large	15.8	11.1	14.7 ± 0.1 (84 wt-%)	33.4 ± 0.2	9.87

* R_{wp} = weighted profile R-factor

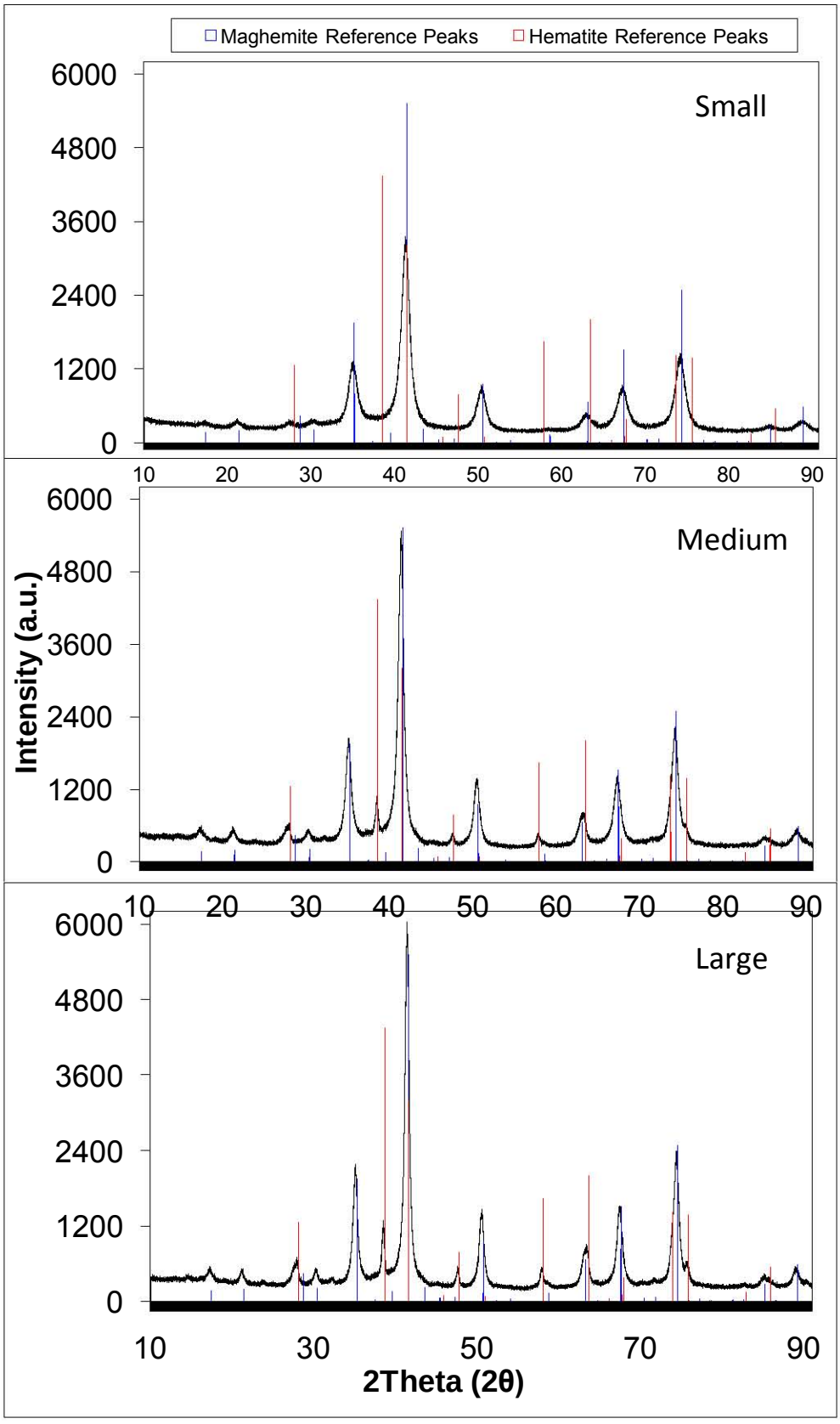

Figure 5.3: XRD scans of calcined samples

The sizes obtained (from the XRD calculations) provide the average volume weighted crystallite sizes and not the number based mean crystallite size as obtained directly via TEM analyses.

The Rwp value represents the errors regarding the fit between the mathematical convolution models and the experimental scans. With the Rwp number < 10 the calculated results are considered of acceptable quality. The size results, correlate closely with the weighted results obtained from the manually done full-width half maximum calculations. All the sizes form the γ-Fe_2O_3 and α-Fe_2O_3 phases with the γ-Fe_2O_3 being the predominant one. The amount of α-Fe_2O_3 phase increases from 2 to 16 wt-% (seen in Table 5.2). This is in qualitative agreement with the findings by Mabaso (2005). The large crystallites contain large sized α-Fe_2O_3 crystallites and the volume based results shown in Figure 5.3 are larger than the desired sizes. However, the main concern regarding the sizes is the crystallite size distributions and this is provided by the TEM results which will also explain the reason as to the large volume based crystallite sizes.

5.2.3 TEM & HRTEM Analysis

This characterization technique proved to be the most useful as it provided the crystallite distributions which is the major concern when working with specific sizes. The TEM images, size distributions and crystallite sizes of the calcined samples are shown in the following figure and table (Figure 5.4 and Table 5.3).

Figure 5.4: Calcined samples TEM pictures & size distribution graphs

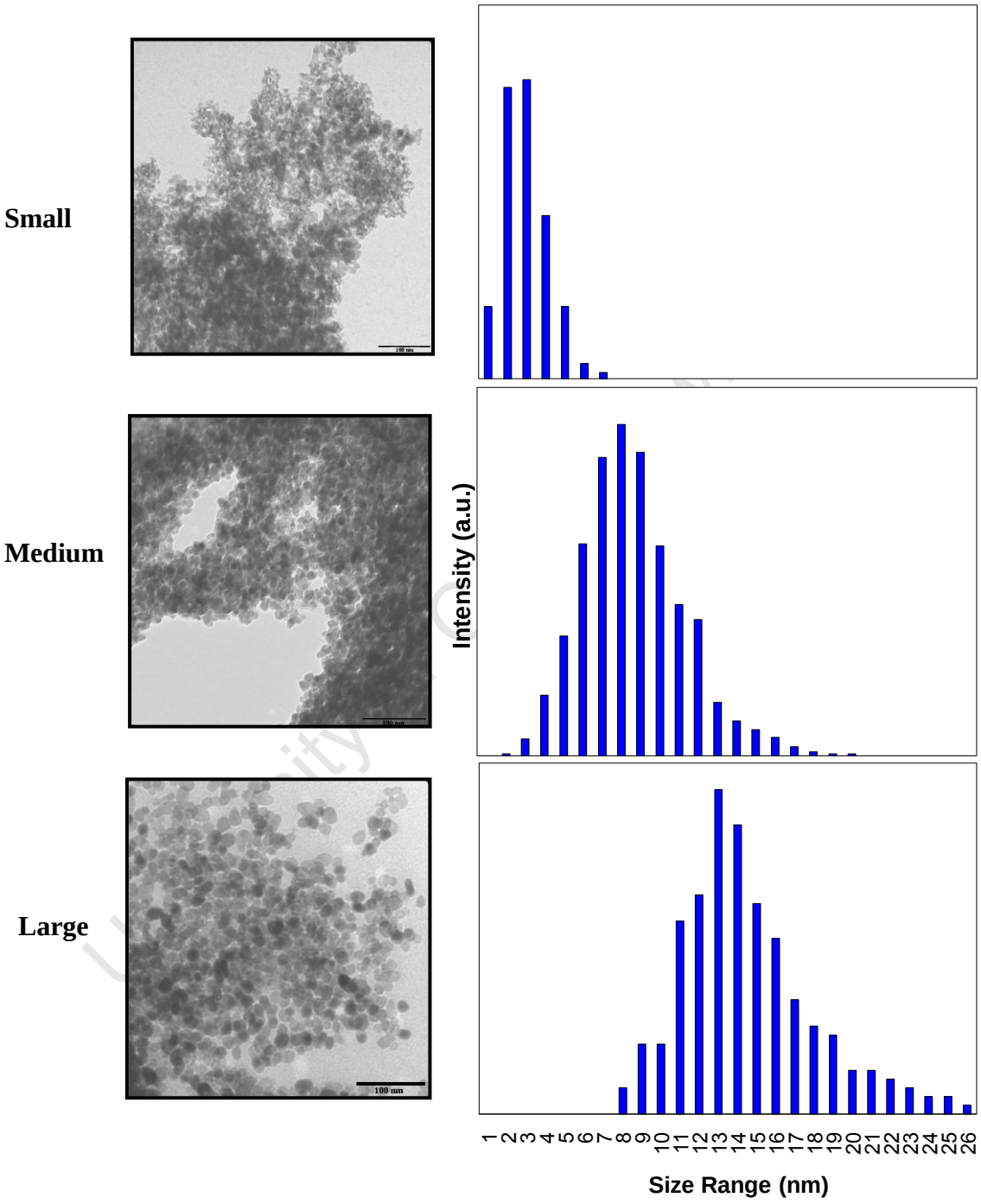

Table 5.3: TEM & HRTEM calcined samples results

Size Class	TEM		HRTEM	
	Volume based size	Average Size	Volume based size	Average Size
	nm			
Small	6.7	3.4 ± 1.1	7.1	3.8 ± 1.0
Medium	11.9	8.3 ± 1.9	12.2	8.5 ± 1.4
Large	16.4	13.4 ± 2.8	16.2	15.0 ± 2.5

From the images (scale of 100 nm), it can clearly be seen that the crystallite sizes indeed increase when the size class increases. For all 3 size classes, the standard deviations are below 3 nm, suggesting that the distributions are reasonably narrow which can also be seen in the size distribution graphs in Table 5.3.

5.2.4 Characterization Techniques Size Comparison

The analysis of the sizes obtained from the different characterization techniques is compared to decide as to whether the desired sizes have been synthesized.

Table 5.4: Comparison of the different characterisation techniques

Size Class	XRD FWHM (nm)		Topas (nm)		TEM	HRTEM
	γ-Fe_2O_3	α-Fe_2O_3	γ-Fe_2O_3	α-Fe_2O_3	đc (nm)	
Small	7.7	4.8	7.9	4.0	6.7	7.1
Medium	11.6	7.7	11.3	14	11.9	12.2
Large	15.8	11.1	14.7	33.4	16.4	16.2

Table 5.4 shows the correlation in the average volume based crystallite sizes obtained from the different characterization techniques and that the closeness (in the results) between these techniques implies that the average sizes obtained from the TEM and HRTEM calculations are feasible and represent the crystallite sizes reasonably. For the large crystallites, the weighted sizes seem to be very close to the actual desired crystallite size compared to the other 2 crystallite sizes (small and medium). The α-Fe_2O_3 sizes do not correspond closely when comparing the Topas and XRD FWHM calculations. The Topas α-Fe_2O_3 size result is not likely to be the most accurate results because the background noise could have been considered in the calculations.

Therefore, since the 3 distinct size distributions and the narrowness of the distributions reflect the desired sizes closely, it can be stated that the synthesis of 3 narrowly distributed crystallite sizes has been established. The small class size was not characterized by Mabaso (2005) using the XRD characterization technique, however, the TEM results showed that Mabaso (2005) synthesized smaller crystallites (2 ± 0.6 nm) compared to that synthesized in this project. The same observation can be made for the medium (7.75 ± 1.6 nm) and large crystallites (15.7 ± 2.5 nm) synthesized by Mabaso (2005).

5.2.5 Mössbauer Analysis

The Mössbauer spectrometer (MS) is used to analyze the fresh catalyst and Table 5.5 provides the MS results.

Table 5.5: Mössbauer spectra results summary for the 3 different calcined crystallites

Size Class	δ (mm/s)	Δ (mm/s)	B_{hf} (T)	Area (%)	Phase
Small	0.34	0.02	46.6	81	γ-Fe_2O_3
	0.34	0.74	-	19	α-Fe_2O_3
Medium	0.34	0.02	47.5	88	γ-Fe_2O_3
	0.40	-0.18	51.4	7	α-Fe_2O_3
	0.38	0.83	-	5	α-Fe_2O_3 *
Large	0.33	0.00	48.5	81	γ-Fe_2O_3
	0.38	-0.17	51.5	10	α-Fe_2O_3
	0.37	0.82	-	9	α-Fe_2O_3 *

(*): α-Fe_2O_3 in superparamagnetic state

Both XRD and Mössbauer spectroscopy provide the same phases, with γ-Fe_2O_3 being the dominant phase. For the large crystallites and almost exact agreement of the XRD Mössbauer data was obtained, whereas Mössbauer characterization results in a larger fraction of α-Fe_2O_3 (i.e. 19% as opposed to 2%) in the smallest crystallites. This maybe due to the fact that some of these very small crystallites are not fully XRD visible. The Mössbauer characterization was conducted at low temperatures so that even very small crystallites can be characterized.

The Mössbauer data are therefore considered more accurate; however they do not provide crystallite sizes, which were obtained via XRD characterization. Overall it must again be stated that generally the Mössbauer and the XRD data are in relatively good agreement.

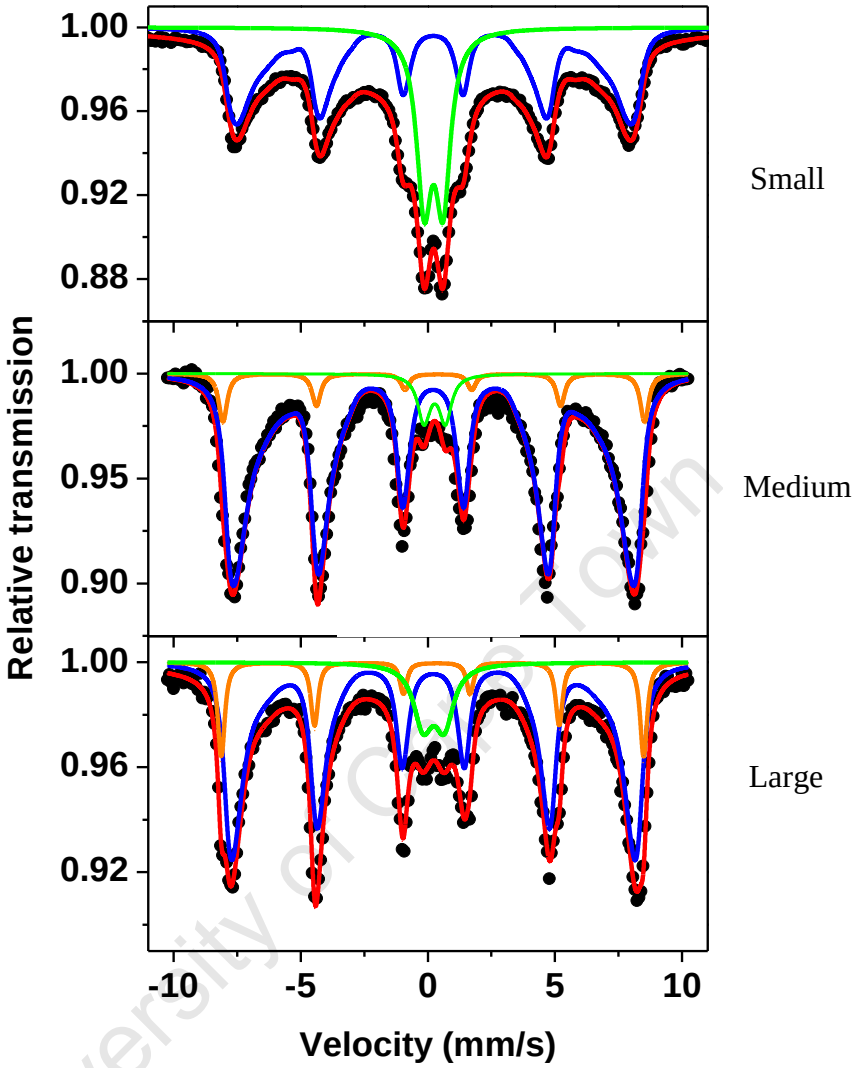

Figure 5.5: Mössbauer spectroscopy scans for the different calcined size classes

5.2.6 Calcination Methods 1 & 2 Comparison

The ignitions can be seen as sparks in the tubular glass reactor and this ignition was controlled/minimized by diluting the air in argon. This was utilized for the synthesis of the smaller sized crystallites because these sintered much easier and formed the undesired sizes shown in Table 5.6.

Table 5.6: Comparison of calcination methods 1 & 2

Method	TEM (nm)		XRD FWHM (nm)		XRD Topas (nm - %)	
	$đ_c$	Avg.	γ-Fe_2O_3	α-Fe_2O_3	γ-Fe_2O_3	α-Fe_2O_3
1-Air	9.0	5.3 ± 1.6	10.4	16.2	8.4 ± 0.2 (70.7)	17.0 ± 0.3
2-Air/Ar	6.7	3.4 ± 1.1	7.7	4.8	7.9 ± 0.1 (98)	4.0 ± 0.4

It can be seen that calcination method 1 does not synthesize the desired crystallite size range as the ignition is very severe. The ignition sparks can be seen when lifting the glass calcination tube out of the chamber. This is the ignition of the Berol that was not washed away by the acetone and usually occurs around 220°C and the temperature runs away to above 600°C before starting to cool down. The ignition takes place at 220°C for all the crystallite size classes.

The dilution of the air in argon (method 2) proved constructive as it did control the ignition of the Berol and reduced the space velocity of the O_2 still keeping the catalyst fluidized in the tube. After obtaining the three desired crystallite size ranges, the next logical step is the reduction/activation of the catalyst before the FT testing stage.

5.3 Reduced Catalyst

Reducing the catalyst proved to be the most difficult and crucial aspect of the catalyst synthesis process. Initially, the metallic iron phase was going to be the starting

catalyst; however, this required the reaction of the iron oxides with hydrogen to produce the metallic iron and water.

5.3.1 Reduction in H_2

As mentioned in section 4.1.4, the iron oxide catalyst is reduced in H_2 to 400°C and the reduction behavior of the catalyst was observed in the in-situ XRD instrument and the final distribution was obtained using the TEM instrument.

In-situ XRD and TEM

The following figure (Figure 5.6) shows the in-situ XRD scans in 3 dimensions with the intensities, scan number and the 2 theta diffraction values. It can be clearly seen that the catalyst sinters very quickly from 300°C onwards when forming the metallic iron.

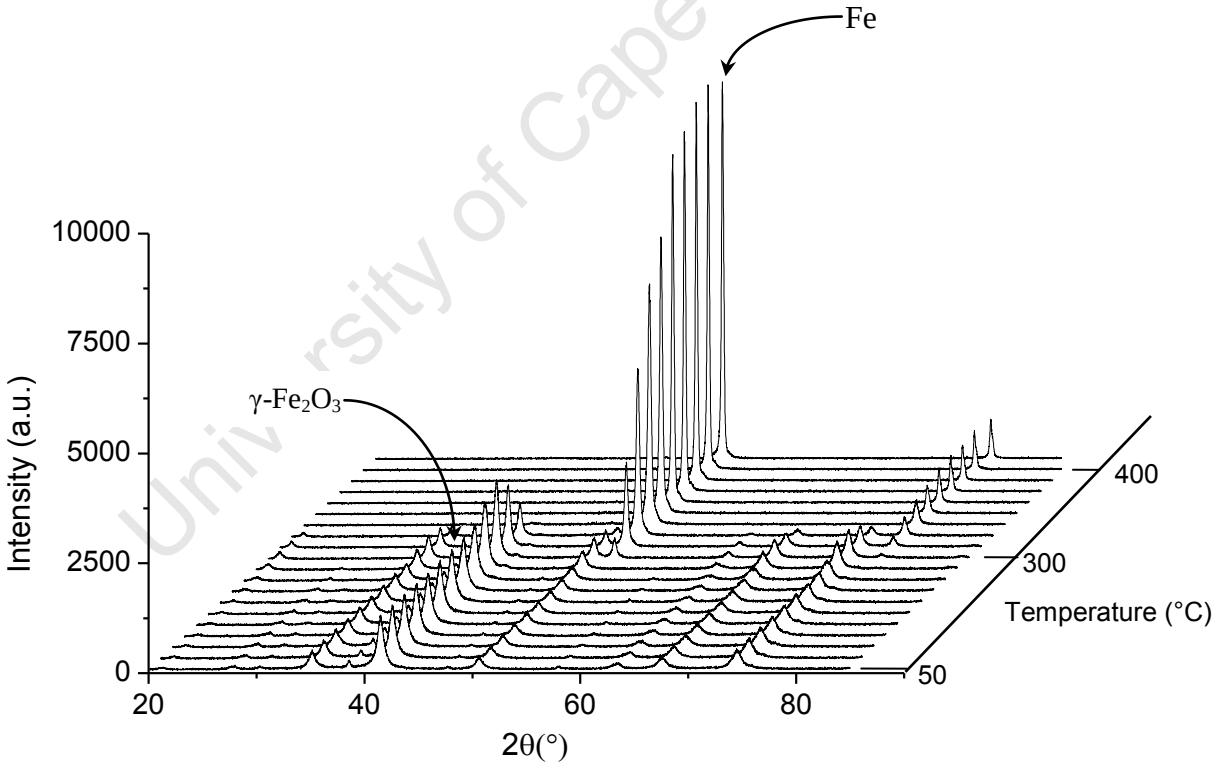

Figure 5.6: 3D reduction results of the medium catalyst in H_2

Table 5.7: Size results of the medium H_2 reduced catalyst

Characterization Technique	Size (nm)
XRD FWHM	120.2
Topas-4	128.3

Table 5.7 shows the crystallite size results obtained from the XRD calculations. Hence, it can be seen that reducing the catalyst in H_2 did produce the desired active phase but the desired crystallite size distribution was not preserved. This resulted in a shift from utilizing the metallic iron as the active phase to the iron carbides.

5.3.2 Iron Carbide Synthesis from CO

The carbidization of the iron catalyst is investigated by initially analyzing the catalyst's behavior in the in-situ XRD chamber to 400°C to obtain the required temperature for the catalyst CO activation. The sample utilized for this temperature determination is the medium-sized catalyst as it is the middle size within the desired range and is expected to provide a sufficient reduction temperature for the smaller and larger crystallite sizes.

In-situ XRD (400°C)

Table 5.8: In-situ XRD CO reduction scan results to 400°C

Scan No.	Temperature	XRD FWHM	Phase(s), Sizes (nm) and Percentages (%)		
	(°C)	(nm)	Fe_3O_4	Fe_3C	χ-Fe_5C_2
10	275	16.7	16.7 (48.2)		4.0 (51.8)
11	300	20.0	24.8 (24.7)	4.8 (21.7)	7.4 (53.6)
12	325	7.5	39.5 (1)	9.6 (11.1)	7.4 (87.9)
13	350	7.5		4.9 (54.7)	7.7 (45.3)
14	375	7.2		4.6 (61.8)	8.7 (38.2)

Table 5.8 shows the phases produced and crystallite sizes obtained in the CO reduction of the iron oxides. From the XRD results, it was observed that the optimum temperature for the catalyst CO activation process should be conducted at

350°C (scan 13). The 3D result of the full carbidisation process is shown in Figure 5.7.

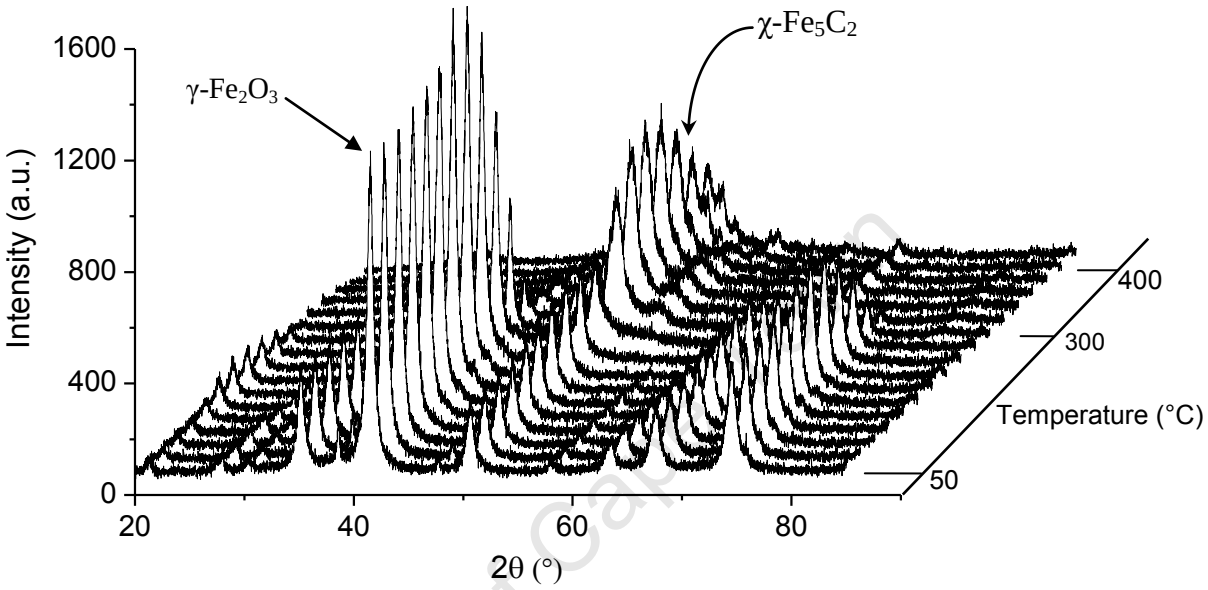

Figure 5.7: 3D reduction results of medium catalyst in CO

Since, this temperature proved reasonable (i.e. provides only carbides as seen in Table 5.8), the CO reduction of all the catalysts was conducted at 350°C and the following sub-section will provide the results.

In-situ XRD and TEM (350°C)

The catalyst is reduced utilizing the procedure explained in section 4.3.2.2 which uses the in-situ chamber settings. The 3D plots of the results are shown in Figure 5.8, Figure 5.9 and Figure 5.10.

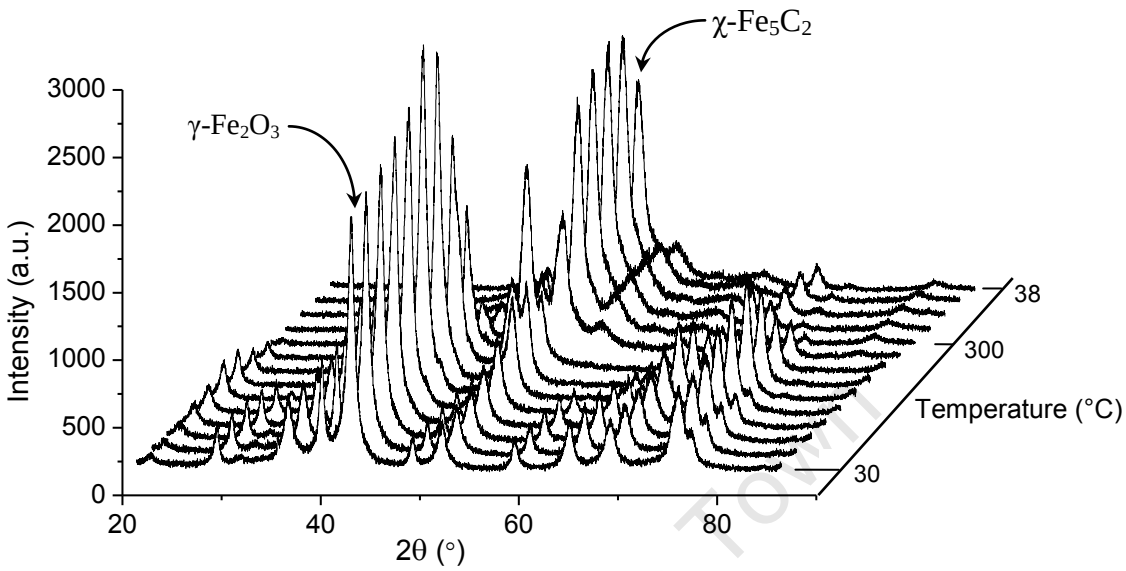

Figure 5.8: 3D results of small catalyst to 350°C

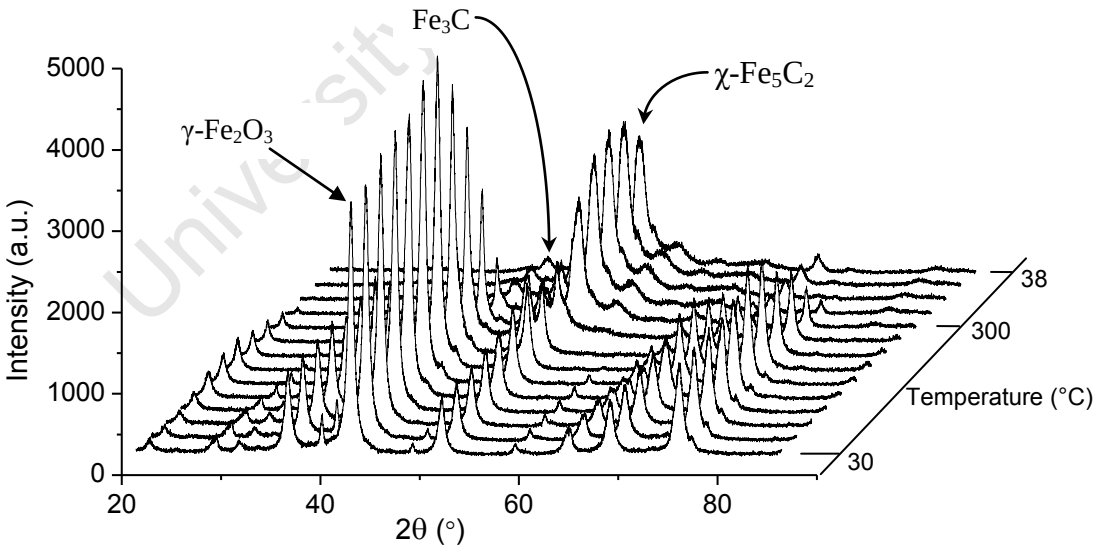

Figure 5.9: 3D results of medium catalyst to 350°C

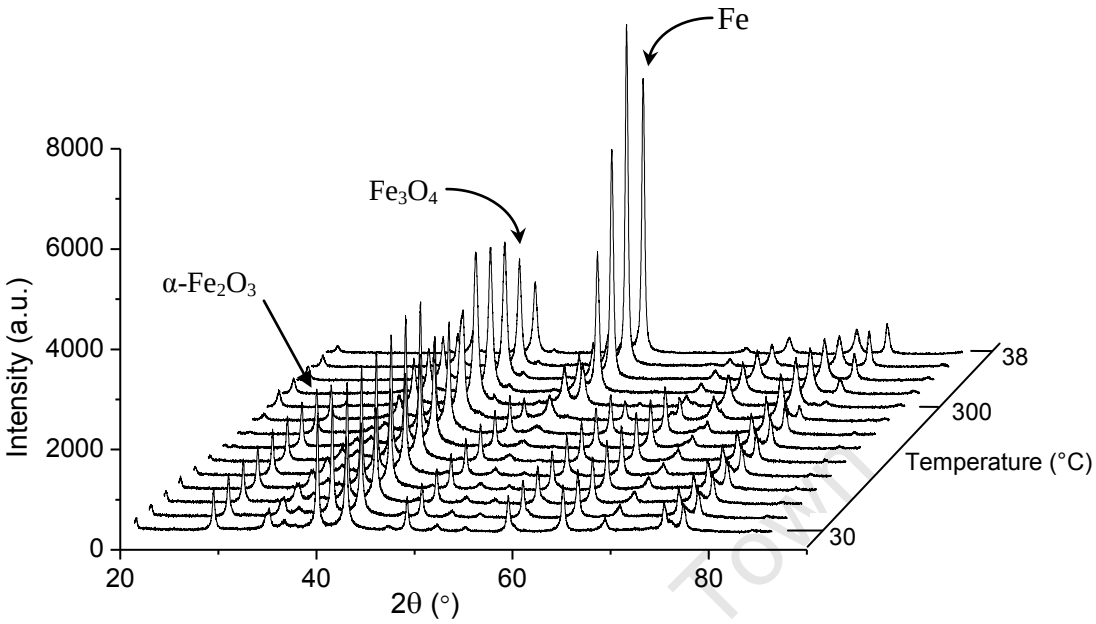

Figure 5.10: 3D results of large catalyst to 350°C

It can be seen from the final 3 XRD scans (shown in Figure 5.8, Figure 5.9 and Figure 5.10) that the size differences are distinct and as the size class peak intensities increase, the size class increases. The catalysts' size results are shown in Table 5.9 including the results obtained from using the NanoSEM characterization technique. The images obtained using this technique is shown in Figure 5.11. Figure 5.12 and Figure 5.13 show the TEM and HRTEM images, respectively.

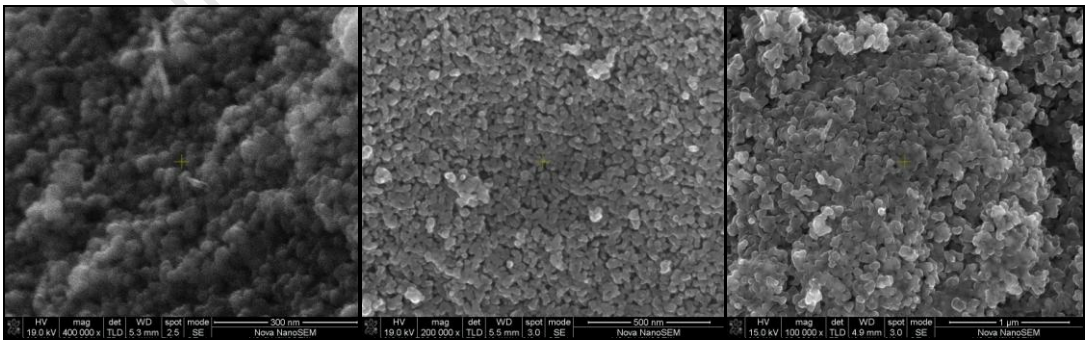

Figure 5.11: NanoSEM pictures of crystallites pre-treated in CO (350°C)

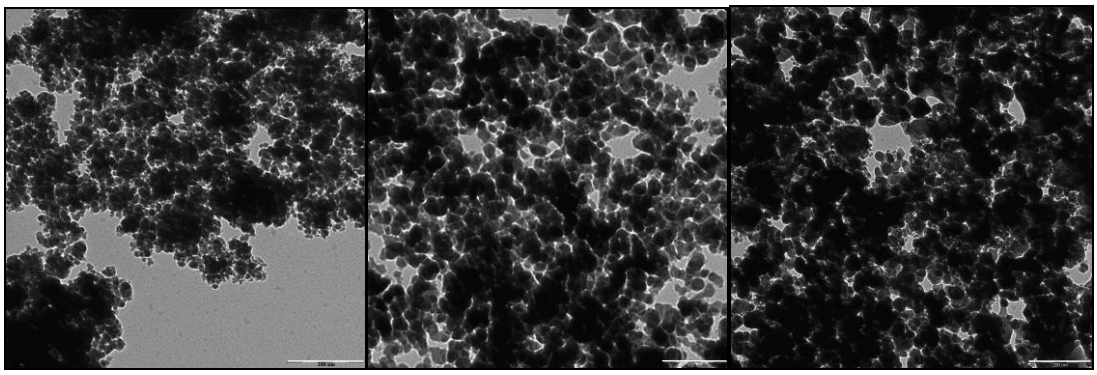

Figure 5.12: TEM pictures of desired crystallites pre-treated in CO (350°C)

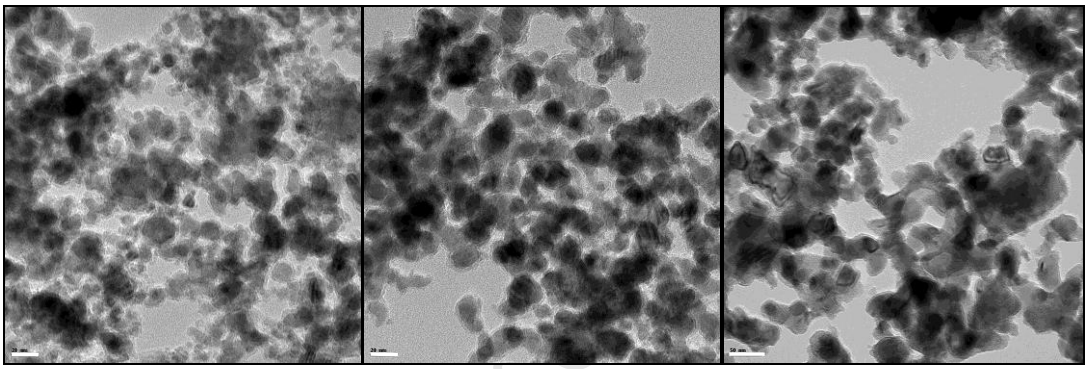

Figure 5.13: HRTEM pictures of desired crystallites pre-treated in CO (350°C)

Table 5.9: Crystallites sizes obtained after in-situ CO reduction at 350°C

Size Class	Units (nm)/Phases	Small	Medium	Large
NanoSEM	**đc**	11.0	14.2	83.0
	Avg.	8.5 ± 2.5	11.2 ± 3.4	58.0 ± 62.3
TEM	**đc**	8.8	11.0	28.4
	Avg.	3.9 ± 1.9	8.4 ± 2.4	17.3 ± 10.2
HRTEM	**đc**	7.5	10.2	36.9
	Avg.	4.1 ± 1.1	6.8 ± 2.1	28.1 ± 8.6
XRD FWHM	**χ-Fe_5C_2**	6.3	9.8	
	Fe			34.0
XRD Topas (nm - %)	**χ-Fe_5C_2**	8.0	9.3 (76.5)	
	Fe_3C		3.5	
	α-Fe_2O_3			29.7 (3.8)
	Fe_3O_4			23.0 (52.8)
	Fe			49.5 (43.4)
	Rwp	9.7	9.1	10.6

* Avg. = number based average

The sizes obtained from the NanoSEM characterization technique proved to be inefficient as they provided only a surface scan of the crystallites. Since the NanoSEM crystallite size results are much larger (25, 29 and 192 % for the small, medium and large crystallites respectively) than the TEM results, it should be noted that this suggests that the crystallite surface is covered with excess carbon.

It can be observed that the crystallite sizes of the reduced samples vary compared to the calcined sample but the size distributions are still reasonably preserved and the size differences are very low (except for the large catalyst). The weighted sizes obtained from the characterization techniques correlate closely for the two smaller crystallite sizes (small and medium crystallites) and the phases produced play a role in the crystallite sizes obtained (and/or vice versa). A study conducted by Sarkar and Davis (2007) showed that when the iron catalyst phase shifts from oxides to carbides; the crystallite sizes decrease.

However in this study, it was observed that during the reduction process from the XRD FWHM and Topas-4 calculations that the crystallite size trend varies as the different phases are formed. For the small sizes, the trends are shown in Figure 5.14 with Figure 5.15 containing the amounts of each phase.

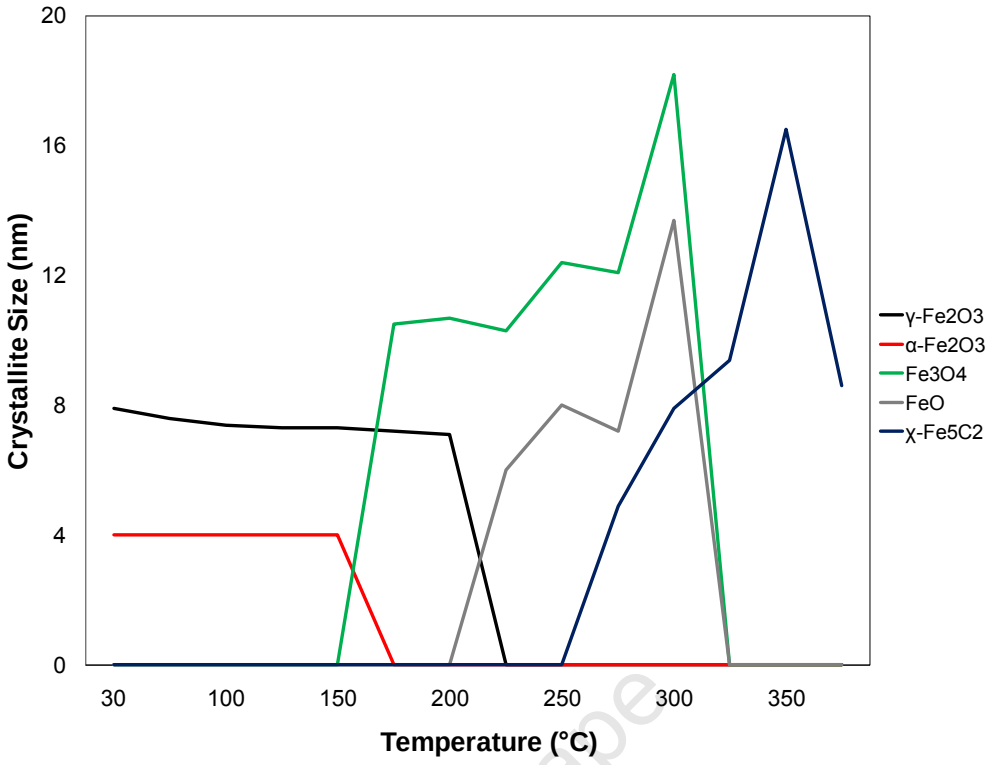

Figure 5.14: Small crystallites' phase changes

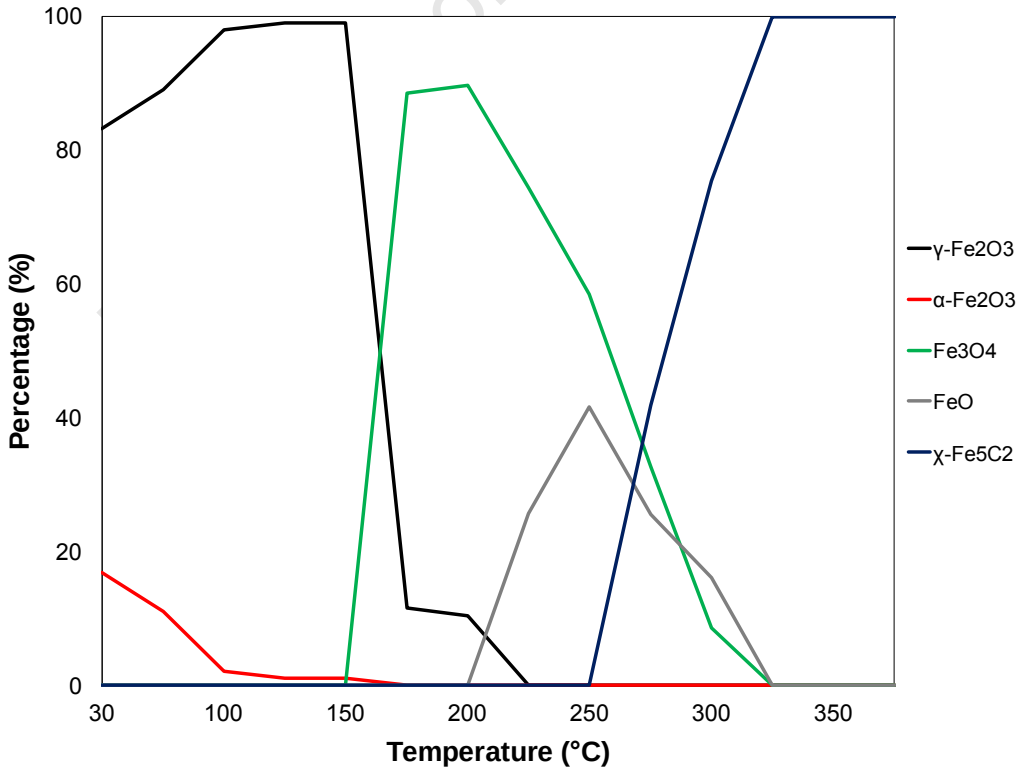

Figure 5.15: Small crystallites' phase content

It was observed that as the size of the γ-Fe_2O_3 crystallites and the α-Fe_2O_3 content decreased, the γ-Fe_2O_3 content increased. This suggests that the larger γ-Fe_2O_3 particles break up to form smaller γ-Fe_2O_3 particles and the α-Fe_2O_3 is converted to the γ-Fe_2O_3 phase. When the temperature is between 150°C and 175°C, the Fe_3O_4 phase begins to form as well as there is a decrease in the other oxide phases. Hence, between these temperatures, the dominant oxide phase is the Fe_3O_4 and the crystallite sizes begin to increase correspondingly. Between 200°C and 325°C, there are only small amounts of the wuestite (FeO) phase and it is observed that due to the formation of the χ-Fe_5C_2 carbide above 250°C, the FeO phase content decreases.

The major size trend observed is that as the χ-Fe_5C_2 carbide is formed from the conversion of the Fe_3O_4 and FeO phase, the average crystallite size decreases. When there are no oxides left, the size of the carbides begin to increase when the temperature is taken to 350°C. It should also be noted that the carbidisation of the oxides only takes place when the temperature is above 250°C in the case of the small crystallites.

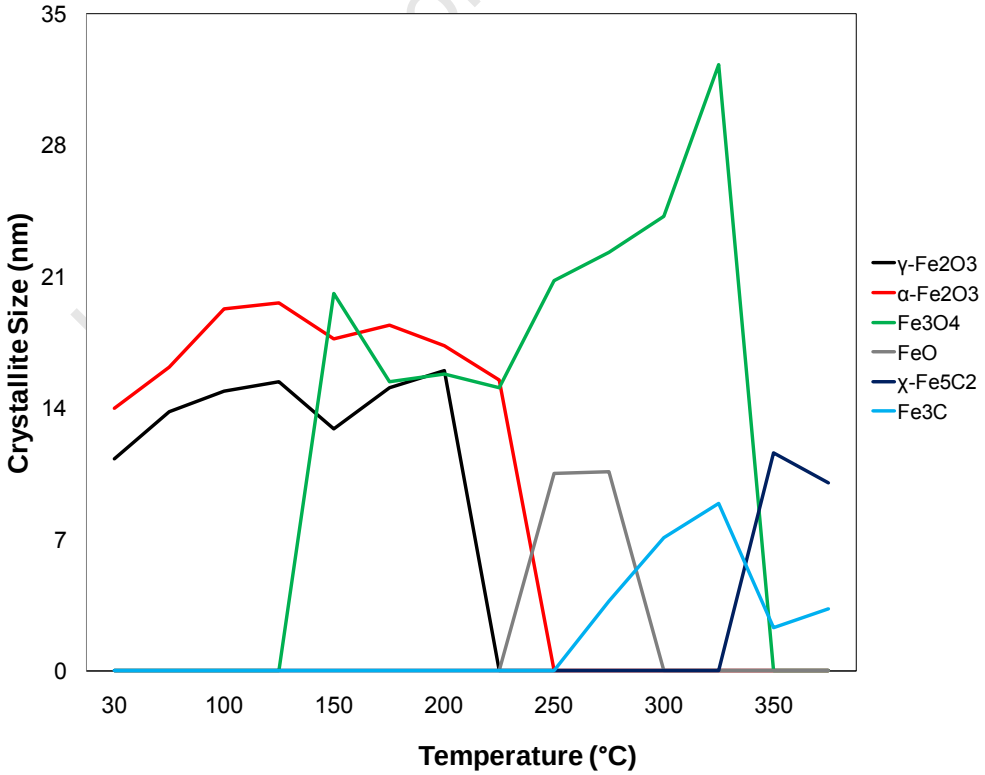

Figure 5.16: Medium crystallites' phase changes

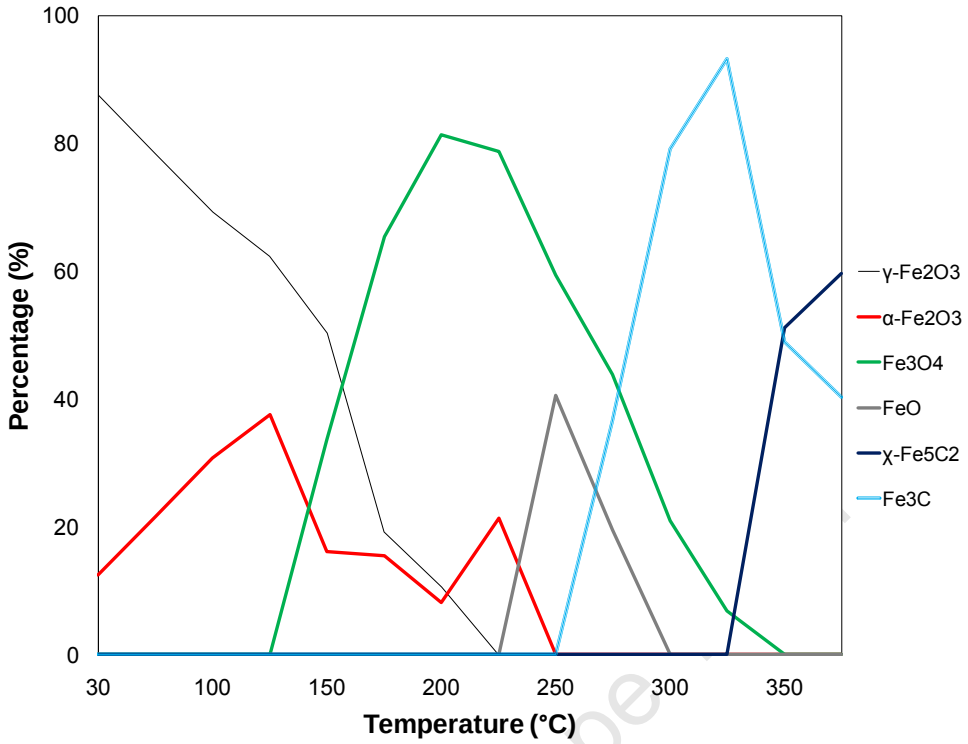

Figure 5.17: Medium crystallites' phase content

For the medium crystallite size range, the figures provide the crystallite size trend (Figure 5.16) and the phase content (Figure 5.17). The oxide phase change from the γ-Fe_2O_3 and α-Fe_2O_3 phases to the Fe_3O_4 phase following a similar trend to that shown in the small crystallite sizes. However, the Fe_3O_4 phase does form earlier (at a temperature just above 125°C) in the medium crystallite size.

The Fe_3O_4 crystallite size continues to increase but the amount of Fe_3O_4 decreases when the temperature is above 200°C. The FeO phase forms in the medium crystallites slightly later than the small crystallites but starts to convert to the Fe_3C phase after 250°C. Above 325°C, the χ-Fe_5C_2 carbide forms as the Fe_3C phase decreases. The χ-Fe_5C_2 carbide forms much later (by 75°C) in the medium crystallites due to the initial formation of the Fe_3C phase. The final phase compositions of the medium crystallites are a mixture of the χ-Fe_5C_2 and Fe_3C carbides unlike the small crystallites as it only formed the χ-Fe_5C_2 carbide. Hence, the size does have an effect on the phase that is formed and both, the small and

medium crystallites form carbides at the same time except that the phase type is different.

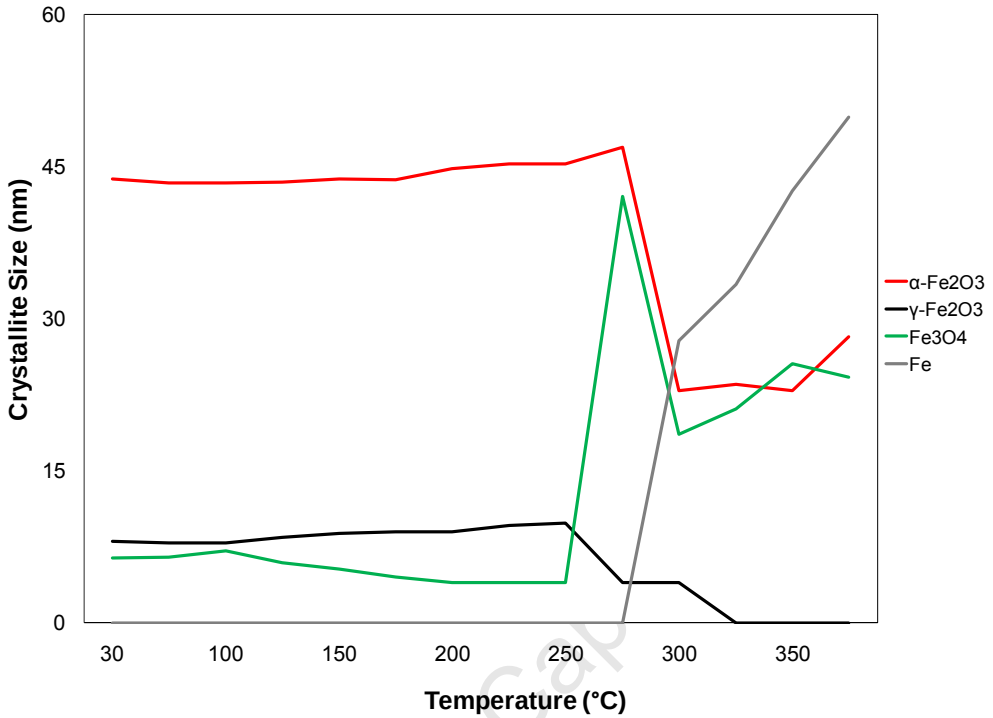

Figure 5.18: Large crystallites' phase changes

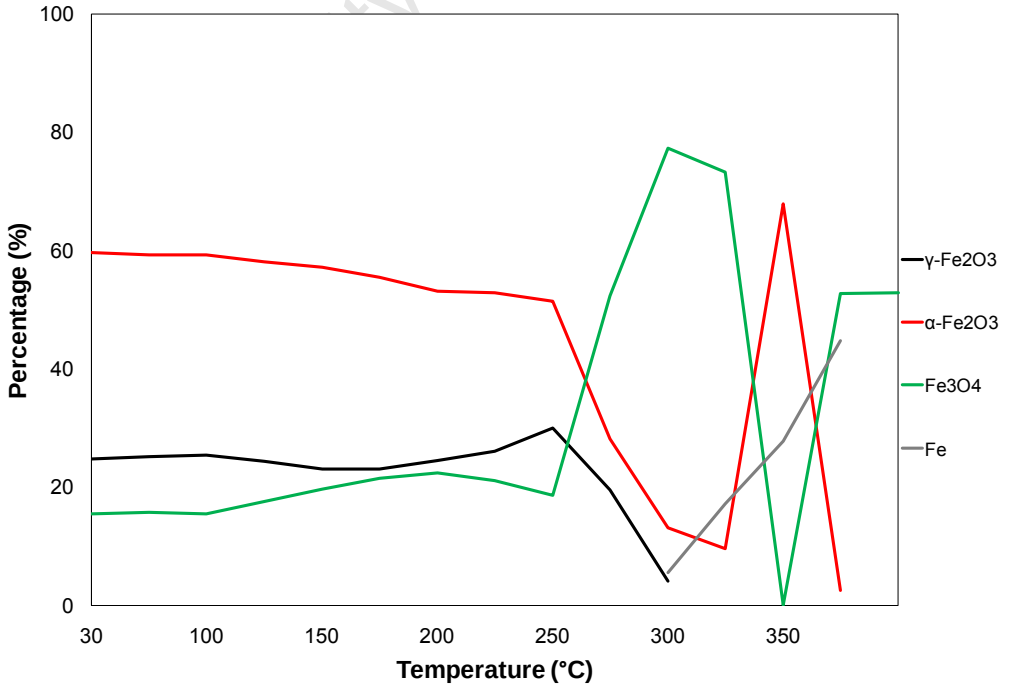

Figure 5.19: Large crystallites' phase content

From the above figures (Figure 5.18 and Figure 5.19) it can be seen that the carbidisation of the large crystallites did not form any iron carbides; however it did contain the metallic iron, α-Fe_2O_3 (trace amounts) and Fe_3O_4 phases. This could suggest that it is required to run the CO reduction of the catalyst for a longer time period above a certain crystallite size. The phase analysis is discussed further in the next sub-section.

5.3.3 Mössbauer Analysis

The MS analysis of the reduced catalyst confirmed most of the results obtained utilizing the XRD characterization technique. The small and medium crystallites result in similar carbides being synthesized with more χ-Fe_5C_2 found in the small crystallites than the medium crystallites. This corresponds to the findings from the XRD analysis. However, the Mössbauer spectroscopy results do not fully correspond to the results observed in the XRD instrument as the Mössbauer results show that some iron carbides do form on the large crystallites (seen in Table 5.10). This could be a result of the intensities caused by the Fe_3O_4 and iron peaks in the XRD results, and relatively small crystallites of χ-Fe_5C_2 carbide present in this sample. A schematic of the Mössbauer spectrograph for the three reduced crystallites is shown in Figure 5.20. It should also be noted that while no Fe_3C phases could be obtained with Mössbauer, the presence of metallic iron could clearly be confirmed in the large crystallites.

Table 5.10: Mössbauer spectra results summary for the 3 different reduced crystallites

Size Class	δ (mm/s)	Δ (mm/s)	B_{hf} (T)	Area (%)	Phase
Small	0.26	0.04	-	82	χ-Fe_5C_2
	0.23	-0.05	18.7		
	0.20	0.12	10.0		
	0.27	1.06	-	5	χ-Fe_5C_2 *
	0.15	0.13	17.4	13	ε'-Carbide
Medium	0.26	0.03	21.8	78	χ-Fe_5C_2
	0.24	-0.09	19.0		
	0.20	0.14	10.1		
	0.24	1.01	-	3	χ-Fe_5C_2 *
	0.15	0.12	17.7	19	ε'-Carbide
Large	0.30	-0.00	49.1	35	Fe_3O_4
	0.66	-0.01	45.7		
	0.00	0.01	33.2	25	Fe
	0.24	0.13	21.6	19	χ-Fe_5C_2
	0.28	-0.20	18.4		
	0.22	-0.13	11.8		
	0.34	0.99	-	16	χ-Fe_5C_2 *
	0.14	-0.04	19.1	5	Fe_3C

(*): χ-Fe_5C_2 in superparamagnetic state

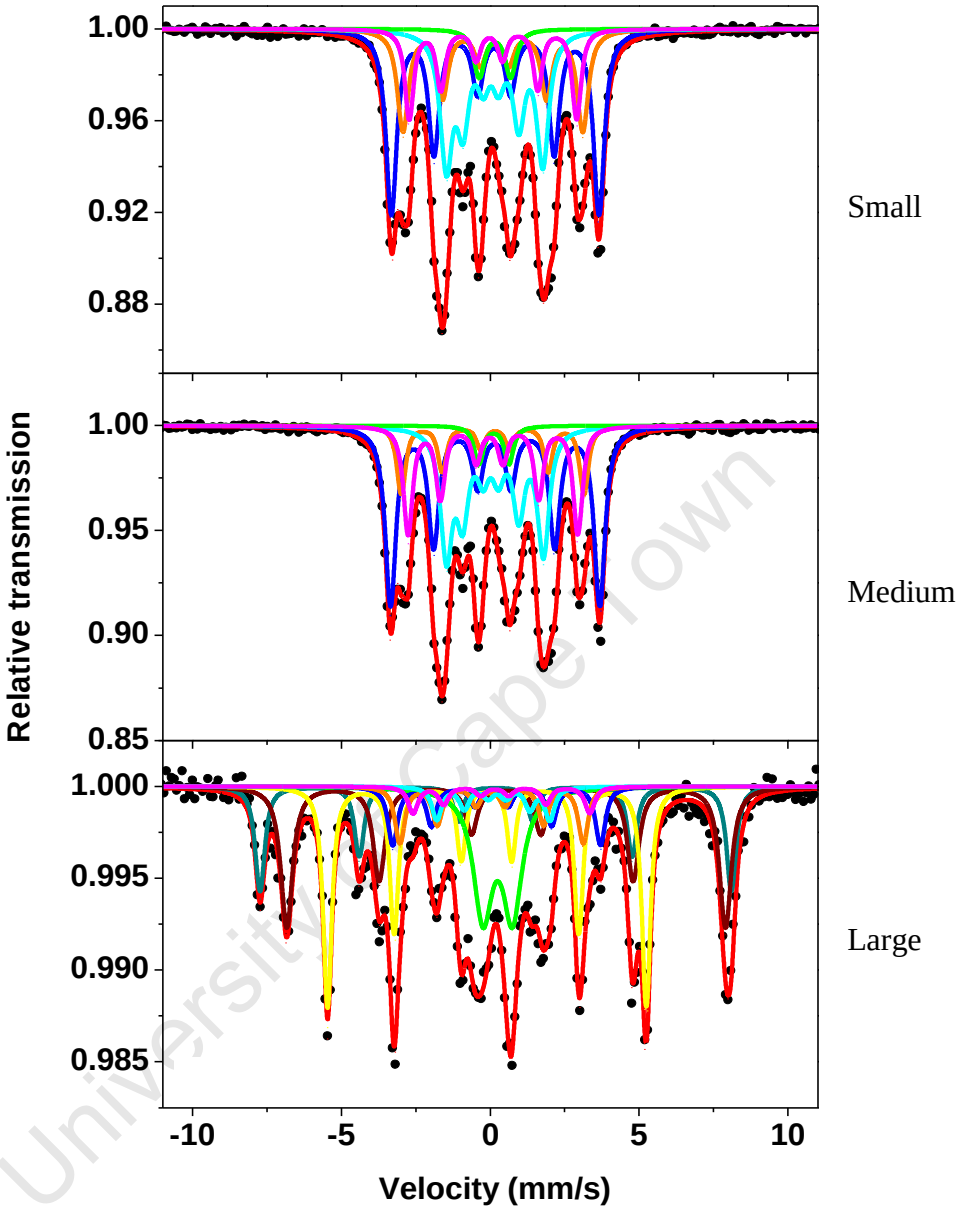

Figure 5.20: Mössbauer spectroscopy scans for the different reduced size classes

5.3.4 Characterization Size Comparisons for CO Reduced Catalyst

Again, it can be seen in Table 5.9 that the NanoSEM characterization technique provides large crystallite sizes and the other characterization techniques provide similar results for volume weighted average sizes. This suggests that the crystallite size distributions represent the catalysts' sizes reasonably except in the case of the large crystallites.

The large crystallites did not form any iron carbide phases and only formed the iron phase. Hence, the iron crystallites, with small and medium sized crystallites, have been activated in CO while maintaining the desired narrow size distributions. This allows for the next stage which is the analysis of the spent catalyst from the Fischer-Tropsch experiments.

5.4 Spent Catalyst

Since only two of the three desired iron carbides were synthesized, the small and medium crystallites were placed under Fischer-Tropsch conditions to determine the size effects of the iron carbides.

5.4.1 Phase and Size Analysis

The XRD, TEM, MS and Topas-4 characterization and analysis techniques are used to determine the spent catalyst's crystallite phases and size.

Table 5.11: Spent catalyst XRD, TEM and Topas-4 results

Size Class	Units (nm) / Phases	Small	Medium
TEM	**đc**	8.2	13.3
	Avg.	5.8 ± 2	10.3 ± 2.8
XRD FWHM	**χ-Fe_5C_2**	6.8	10.8
	SiC		108.1
	$(CH_2)_x$	13.4	26.6
	Glass Wool-Silane	73.4	
XRD Topas	**χ-Fe_5C_2**	7.5 ± 0.1	10.3 ± 0.1

	SiC		84.5
	$(CH_2)_x$	18.2	33.1
	Glass Wool-Silane	1231	
	Rwp	8.624	9.877

The spent small and medium catalysts both showed that the only iron phase present is the χ-Fe_5C_2 carbide and there is some wax deposited on the catalyst's surface.

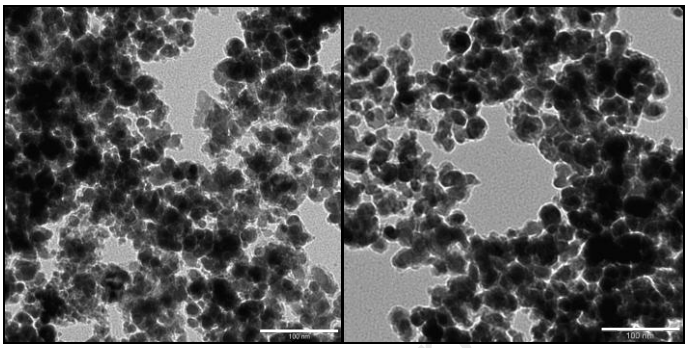

Figure 5.21: TEM pictures of spent catalysts

The sizes obtained from the characterization techniques are closely related and the distributions of the crystallites' remain reasonable as the standard deviations are below 3 nm. Due to the iron catalyst not re-oxidizing to form any iron oxides, it can be also established that the water production was kept sufficiently low because the water is considered to be a potential oxidizing agent. The larger sized crystallites show that there is more wax deposited on the smaller crystallites and this is explained further in the product analysis section (section 5.6).

5.4.2 Mössbauer Analysis

From Table 5.12, it can be seen that both the small and medium crystallites maintain their phases, however, the amount of ε'-Carbide slightly decreases for the medium crystallites and increases for the small crystallites during the Fischer-Tropsch synthesis step. These phase results do correspond to the phases obtained from the XRD characterization technique (shown in Table 5.11) and both the crystallite size classes contain the same phases. The results of the Mössbauer characterization for the two spent crystallites are shown in Figure 5.22.

Table 5.12: Mössbauer spectra results summary for the 2 different spent crystallites

Size Class	δ (mm/s)	Δ (mm/s)	B_{hf} (T)	Area (%)	Phase
Small	0.27	0.02	22.1	74	χ-Fe_5C_2
	0.24	-0.09	18.6		
	0.19	0.14	10.2		
	0.29	1.07	-	7	χ-Fe_5C_2 *
	0.16	0.12	17.6	19	ε'-Carbide
Medium	0.27	0.05	22.0	70	χ-Fe_5C_2
	0.25	0.05	18.3		
	0.17	0.05	10.4		
	0.28	1.06	-	15	χ-Fe_5C_2 *
	0.14	0.11	17.8	15	ε'-Carbide

(*): χ-Fe_5C_2 in superparamagnetic state

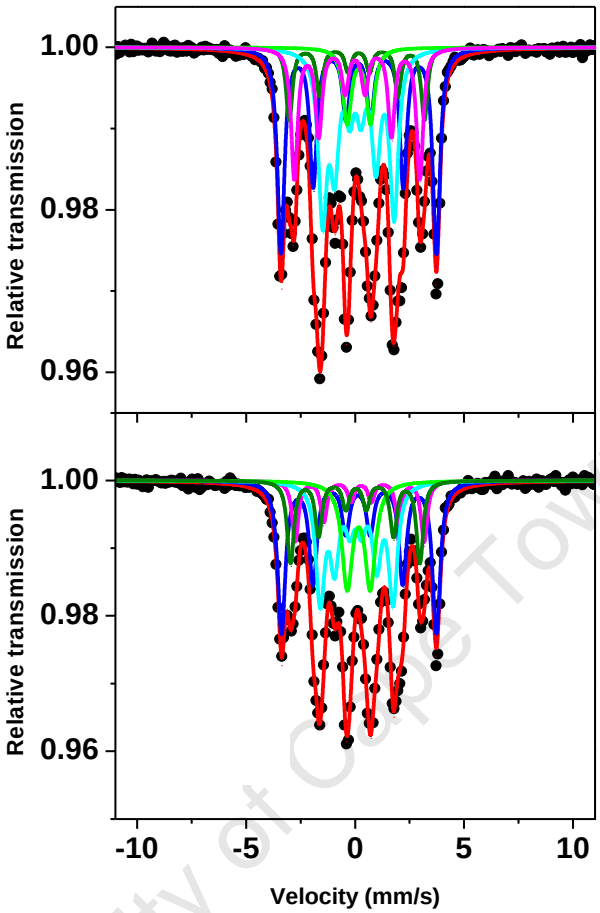

Figure 5.22: Mössbauer spectroscopy scans for the different spent size classes

5.5 Catalyst Sizes from Different Procedures

The TEM distributions of the small and medium sized crystallites at the various stages (calcination, reduction and FTS) are shown in Figure 5.23. The figure shows that there is a shift in the distribution as the various procedures take place. After reducing the catalyst, the crystallite sizes shift slightly in the reactor. When the catalyst undergoes the Fischer-Tropsch synthesis step; the crystallites sizes shift a bit more with a longer tail likely due to the exothermic reactions that take place in the reactor. However, it is important to note that the narrow distributions are still preserved.

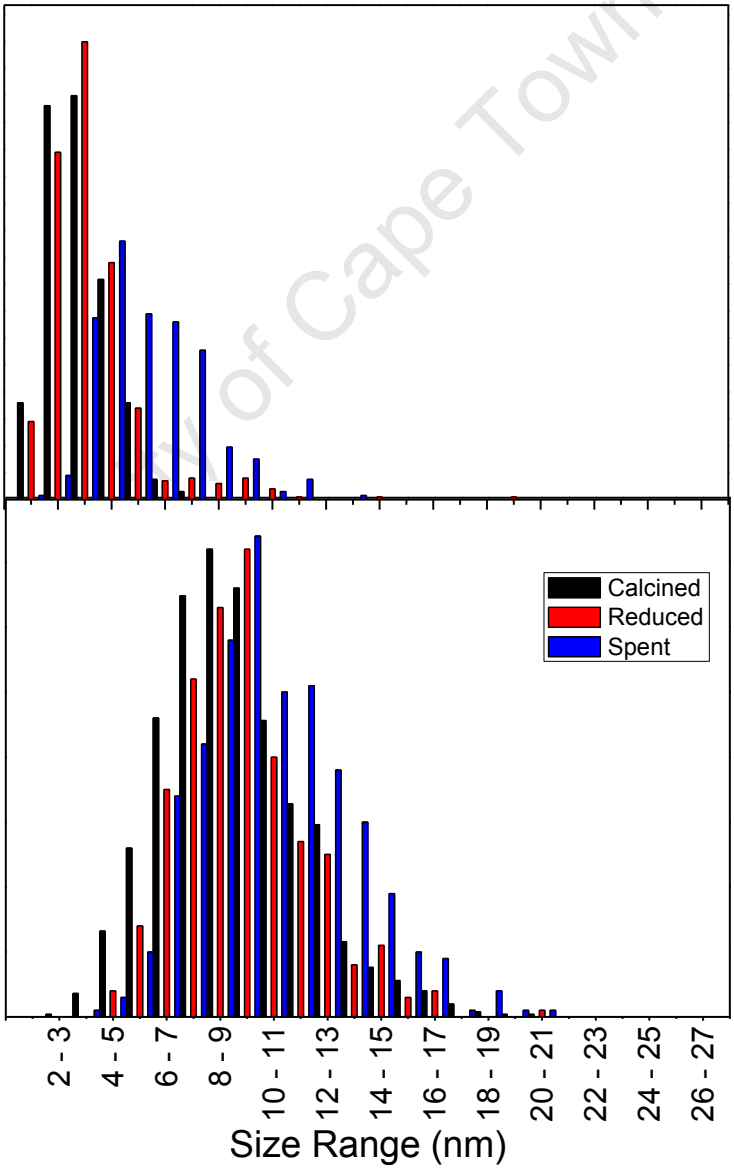

Figure 5.23: TEM distribution of crystallites at various states

The percentage growth of the catalyst was calculated in order to determine which iron crystallite size varies the most during the reduction and testing processes. The growth for the reduction step is determined with the reference as the calcined catalyst and the reduced catalyst is used for the FTS step. The results are shown in Table 5.13 and they are based on the average TEM distribution values.

Table 5.13: Percentage growth of crystallites during reduction and FTS

Size Class	Growth (%)	
	Reduction	**FTS**
Small	14.7	48.7
Medium	1.2	22.6

It can be seen that the growth of the crystallites for the smaller size class is much larger than the medium crystallites. This suggests that the smaller crystallite is much more sensitive to the reduction and testing processes than the larger crystallite. A similar trend was also observed by Cheang (2009). Although the conversion was maintained below 10%, the small crystallites still show sintering and clustering, particularly after the Fischer-Tropsch testing step.

5.6 FT Synthesis Analysis

5.6.1 Conversion and Catalyst Activity

Figure 5.24 and Figure 5.25 show the conversion and activities (per surface area of χ-Fe_5C_2 carbide) obtained in FT experiments using the two crystallite sizes (small and medium).

The steady state conversions were 9.5% and 6% for the small and medium crystallites, respectively. It should also be noted that the initial CO conversion for the medium crystallites (44%) is much greater than the small crystallites (7.6%) steady state is achieved after 180 minutes. For the iron catalyst, the previous studies conducted by Mabaso (2005) and Cheang (2009) show that as the crystallite size decreases, so does the catalyst activity per surface area of iron which corresponds to the findings in this research project where iron carbide was used in the catalysts after pre-treatment as opposed to the metal phase. The same trend is found on the cobalt catalyst by Bezemer et al. (2006) and on the ruthenium catalyst by Barkhuizen et al. (2006).

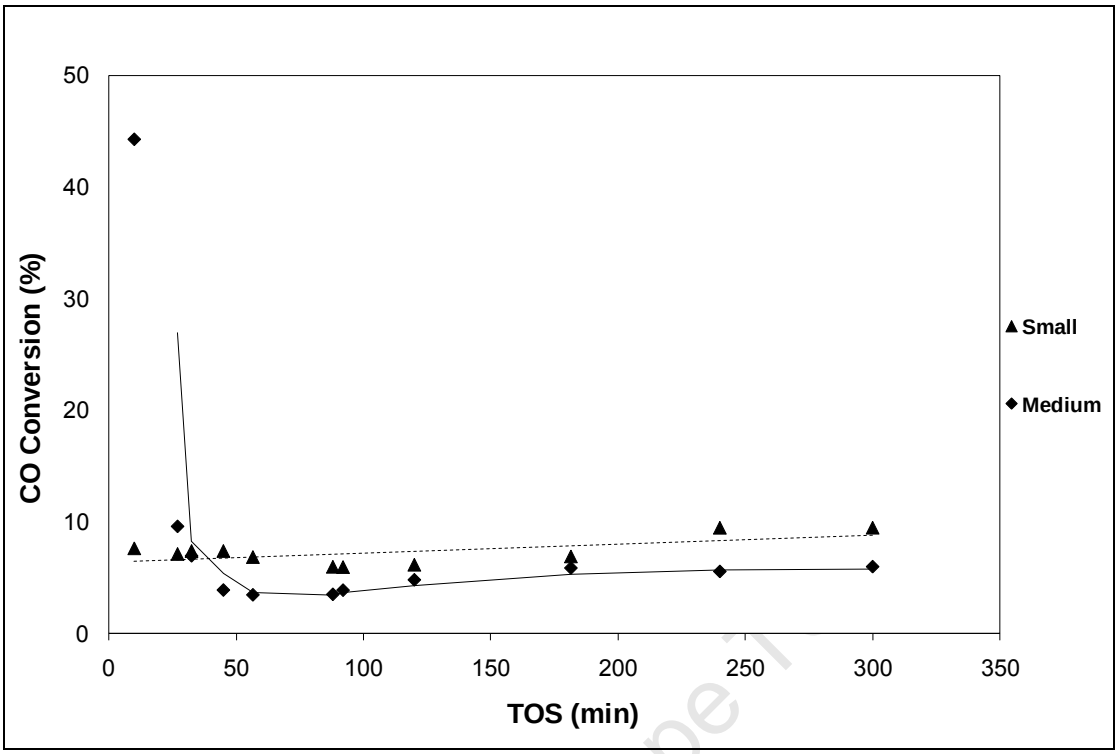

Figure 5.24: CO conversion for small and medium crystallites as a function of the TOS

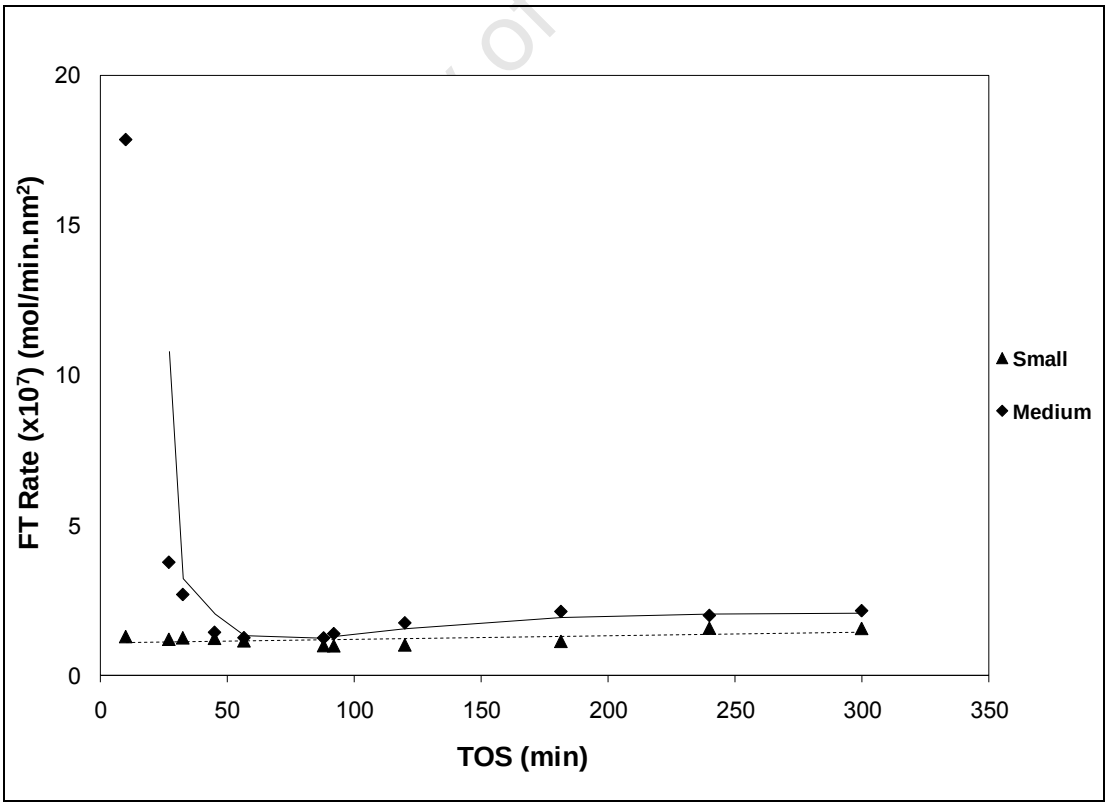

Figure 5.25: Fischer-Tropsch rate for small and medium crystallites as a function of the TOS

5.6.2 Methane Selectivity and CO_2 Formation

The methane selectivity provides a much deeper insight into the happenings on the surface of the crystallites. From Figure 5.26 it can be seen that as the crystallite size decreases, the methane selectivity increases. The trend is the same for both the sizes along the time on stream. The methane selectivity's increasing trend has been previously observed on the iron catalyst by Mabaso (2005) and Cheang (2009). This was also observed by Bezemer et al. (2006) on the cobalt catalyst and on the ruthenium catalyst by Welker (2007).

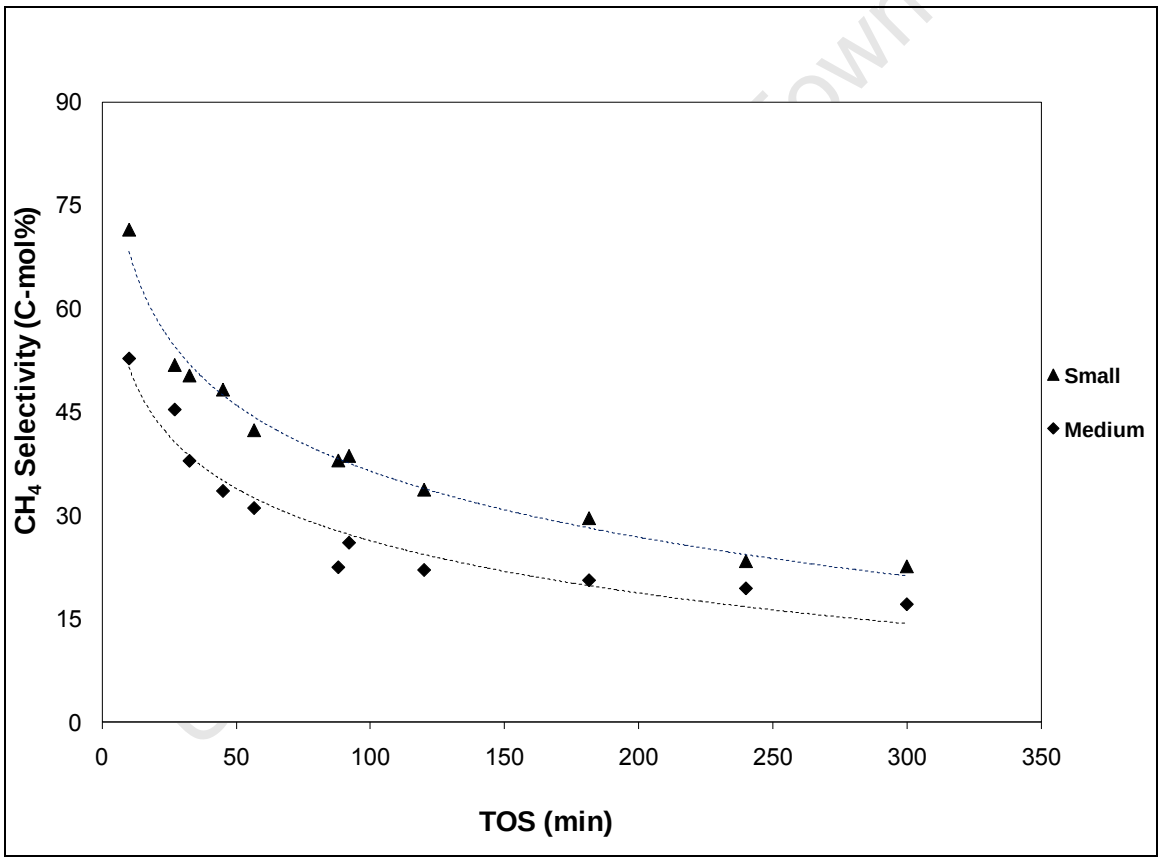

Figure 5.26: Methane selectivity for small and medium crystallites as a function of the TOS

From the 'ensemble' theory explained in section 2.3.4 the relatively increased production of the lower hydrocarbons is due to the reduced amount of active sites 'groups' on the surface of the smaller crystallites. Hence, the methane is much more dominant and selective than the higher hydrocarbons on small crystallites. The

carbon dioxide shows the inverse results of the methane selectivity meaning that a decrease in the crystallite size decreases the amount of carbon dioxide produced.

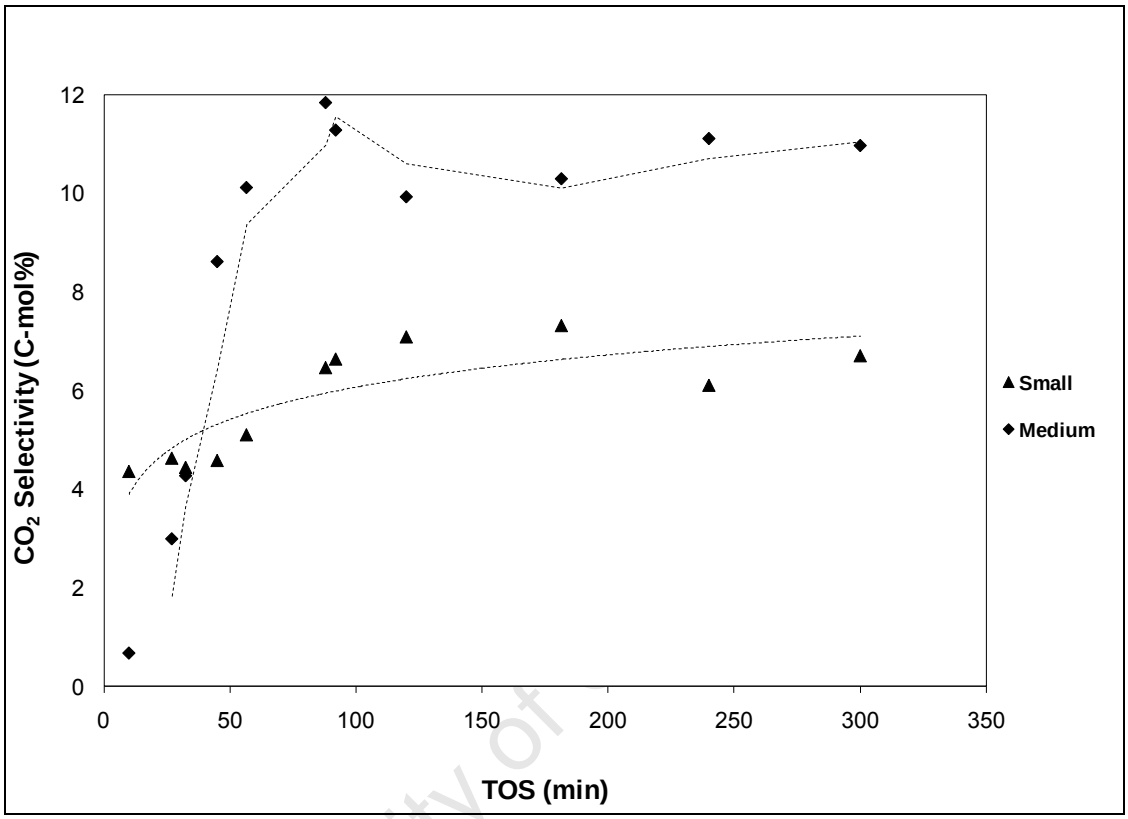

Figure 5.27: CO_2 selectivity for small and medium crystallites as a function of the TOS

The unsupported small crystallites show the same CO_2 trend by the work conducted by Mabaso (2005); however, the catalyst utilized by Mabaso (2005) was supported by carbon. The unsupported iron reduces (by approximately half) the CO_2 selectivity compared to the selectivity obtained by the carbon supported catalyst.

5.6.3 Chain Growth

Figure 5.28 shows the initial and steady state chain growth probability (determined from carbon number range C_3 to C_7) for the small and the medium crystallites (For a graphical representation of the Anderson-Schulz-Flory distributions, see Appendix C). It can be seen that the initial chain growth probabilities for both the crystallite sizes are lower than the steady state value. The small crystallites have a lower chain

growth probability than the medium crystallites; which is in accordance with the methane selectivities which show opposite trends. This can again be related to the 'ensemble' theory where it is explained that when the crystallite size increases, there is a greater possibility for the production of larger products (in this case longer chained hydrocarbons). It can also be seen that at steady state, the values are constant for the small and medium crystallites. These trends were also observed by Mabaso (2005) and Cheang (2009).

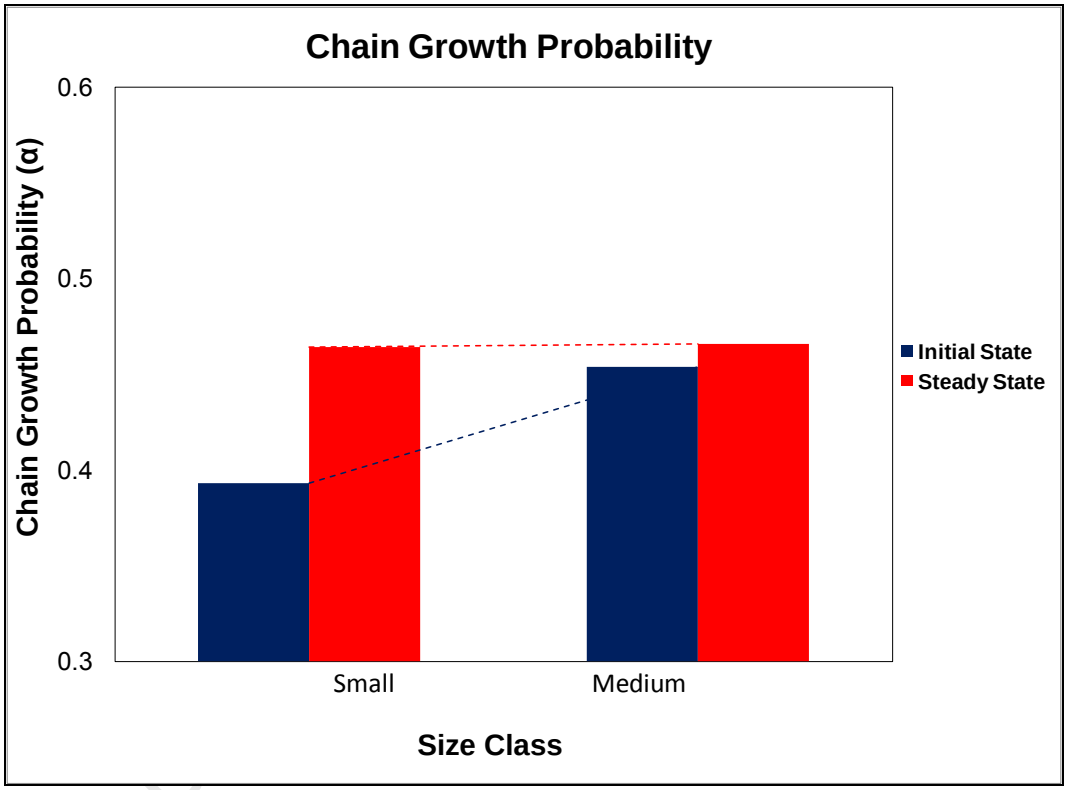

Figure 5.28: Chain growth probability for the initial and steady states of the small and medium crystallites

5.6.4 Hydrocarbon Product Formation

Olefin

Olefins are considered to be the main products synthesized in the Fischer-Tropsch process which have a market value that is seven times greater than petroleum (Schulz, 1999; Barthe and Gahier, 2009). The olefin re-adsorption step has been

noted to normally occur in the Fischer-Tropsch synthesis process A schematic of the olefin desorption and re-adsorption mechanism is shown in Figure 5.29.

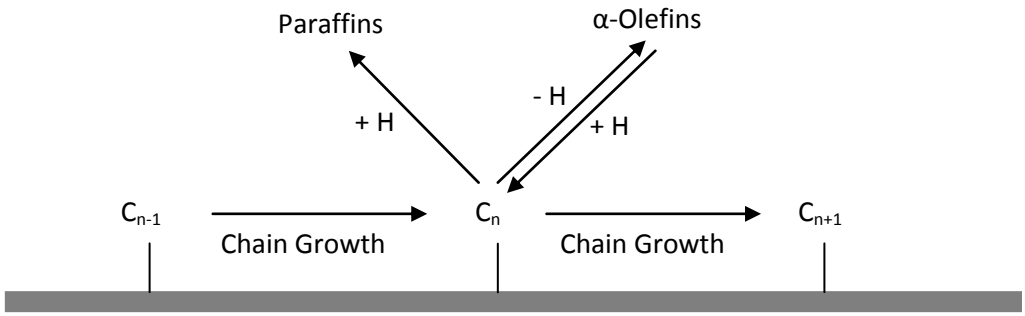

Figure 5.29: α-Olefins desorption and re-adsorption mechanism

It is expected that when testing the catalyst under mild conditions, the secondary reactions (paraffin formation step) are inhibited resulting in greater olefin production. Since the olefins are considered to be the main primary product, their selectivity is expected to be between 70% to 90% during the Fischer-Tropsch synthesis (Schulz and Claeys, 1999(b)).

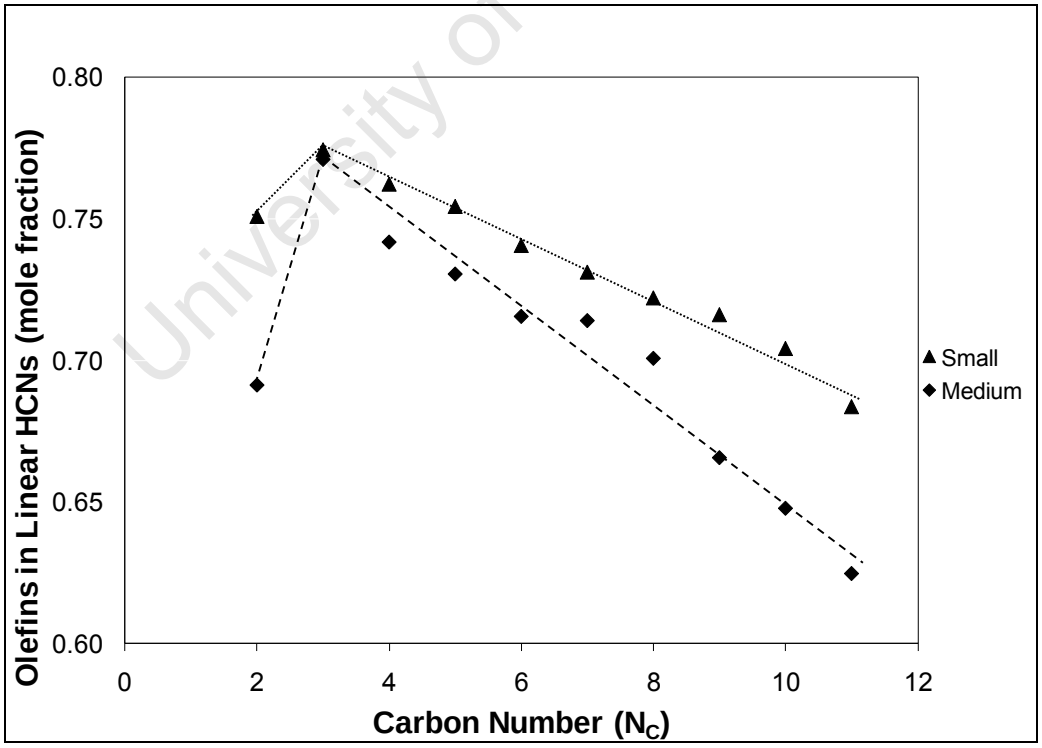

Figure 5.30: Mole fraction of Olefins in the corresponding linear hydrocarbon fraction as a function of the carbon number at steady state

In this study the average molar olefin content in the C_2 to C_{11} carbon number range was found to be 73% for the small crystallites and 70% for the medium crystallites. From Figure 5.30, the olefin production provides an understanding as to whether secondary reactions occur and to which hydrocarbon number this occurs to. The C_2 olefin (Ethene) seems to be the most reactive of the olefins as it has the lowest in the C_2 product fraction. This results in a maximum at carbon number C_3 and a steady decline in the olefin content as the carbon number increases due to increased residence time, hence increasing the re-adsorption probabilities of long chain olefins. Many previous studies have seen the same trend of the C_2 re-adsorption and the C_3 maximum (van der Laan, 1999; Claeys and van Steen, 2004; Mabaso, 2005; Cheang, 2009 Luo et al., 2009). The trend is observed for both, the small and the medium crystallites; however, the medium crystallites have a much steeper decline than the small crystallites which suggests that it is much easier for the olefins to re-adsorb onto the surface of the medium than the small crystallites.

This could be a result of the medium crystallites having much more 'ensembles' available for the re-adsorption of the olefins allowing the increased production of longer chained hydrocarbons. The re-adsorption (secondary reactions) on the medium crystallites corresponds to the findings observed by Cheang (2009). It was observed that there is an increased amount of secondary reactions in the 'middle' crystallite size range. This is also confirmed by the C_5 carbon number fraction shown in Figure 5.31 where the same trend, compared to the work conducted by Cheang (2009), show that the initial state is lower than steady state (stronger secondary hydrogenation!). However, it should also be noted that the initial C_5 olefin contents are larger for the medium crystallites than the small crystallites. The C_5 olefin content in the fraction of the linear C_5 hydrocarbons as function of time on stream is shown in Figure 5.32.

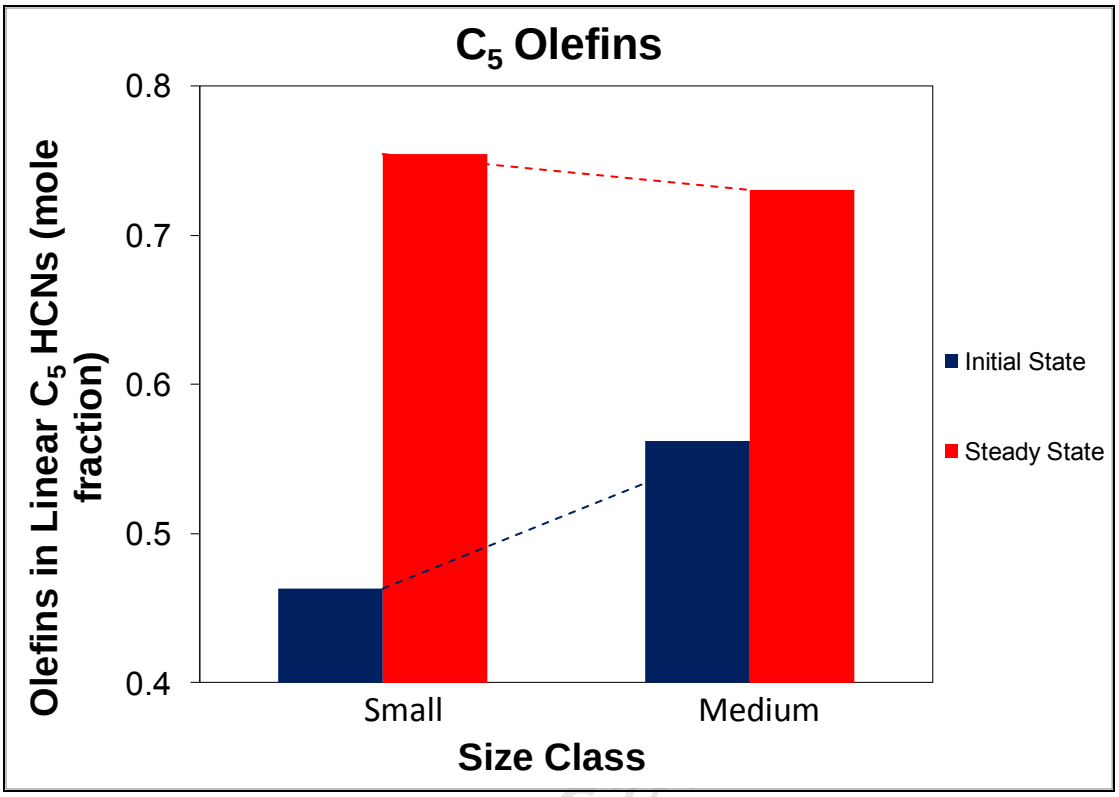

Figure 5.31: Mole fraction of Olefins in C_5 hydrocarbons as a function of the carbon number for the initial and steady states

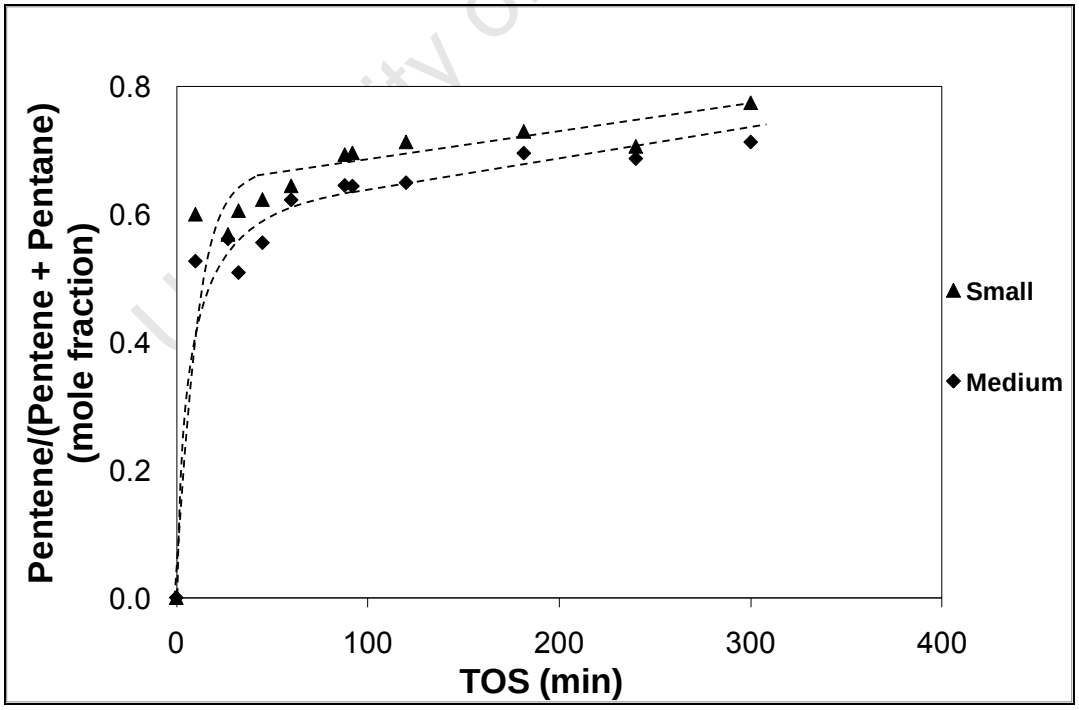

Figure 5.32: C_5 Olefins mole fraction in C_5 fraction for the small and medium crystallites as a function of the TOS

In addition to secondary hydrogenation, primarily formed α-olefins can undergo double bond shift isomerisation. In order to monitor the extent of this secondary reaction, the content of α-olefins in the fraction of linear olefins per carbon number can be monitored. Figure 5.33 shows the content of 1-pentene in the linear C_5 fraction as a function of time on stream for the two crystallite sizes that were tested. Both sizes display very similar behavior with lower α-olefin content at initial stages, indicative of severe double bond shift isomerisation and almost primary selectivity with no double bond shift isomerisation at steady state. This behavior was also observed by others (Barkhuizen et al., 2006; Welker, 2007; Cheang, 2009) and it was proposed that secondary reactions, such as hydrogenation and isomerisation are more facile at the initial stages of the experiments as here the surface of the crystallites is less covered, therefore, allowing re-adsorption of reactive products.

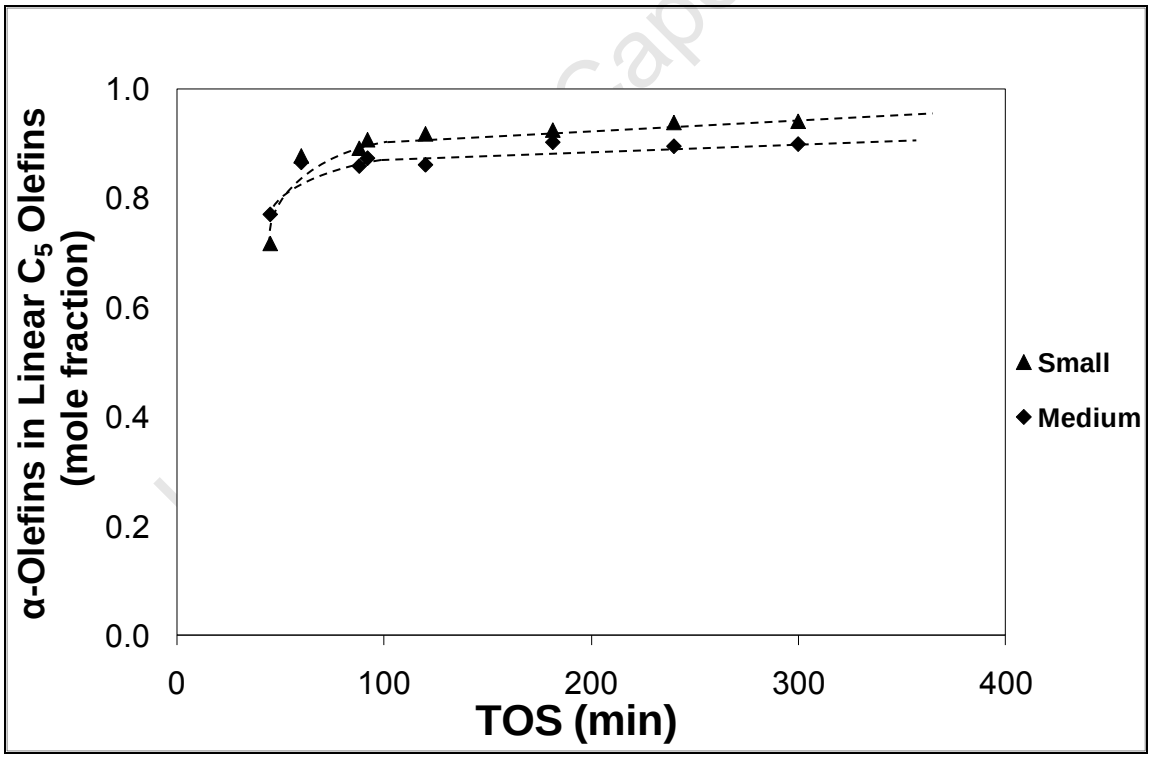

Figure 5.33: α-Olefins mole fraction in C_5 linear olefins for the small and medium crystallites as a function of the TOS

Oxygenates

Oxygenates (mainly alcohols and aldehydes) are common Fischer-Tropsch products but usually exists in small amounts with slight traces of ketones. There have been various mechanisms provided for the understanding of how oxygenates are formed. Pichler and Schulz (1999) mechanisms suggest that oxygenates form through a CO insertion step. The CO chemisorbs on single metal crystallites and dissociates to C and O, allowing the formation of water, CO_2 and the formation of oxygen containing products on the catalyst surface (Davis, 2001). Deluzarche et al. (1977) proposed that the CO is inserted between the O and H of an adsorbed OH species. Johnston and Joyner (1993) proposed that the formation or addition of hydroxyl species will result in the production of alcohols and aldehydes. A schematic of certain mechanisms are shown in Figure 5.34.

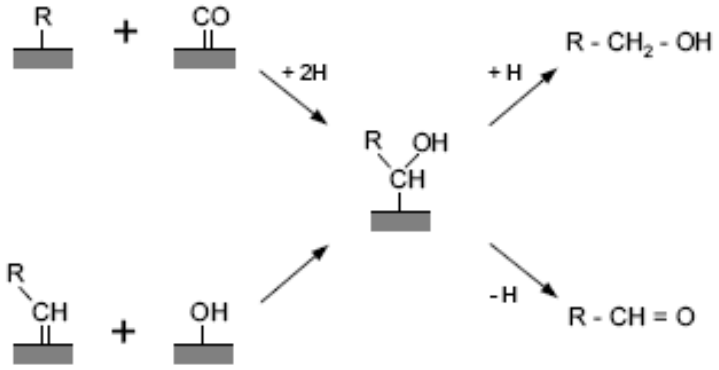

Figure 5.34: Oxygenates mechanisms (Mabaso, 2005)

The products in this work consist of very small amounts of oxygenates, 11 C% for the small crystallites and 13 C% for the medium crystallites. Figure 5.35 provides the mole fraction of oxygenates per carbon number produced in the Fischer-Tropsch synthesis step for both the small and medium crystallites. An increase of the amount of oxygenates was observed for increasing crystallite sizes by Mabaso (2005) and Cheang (2009). However, no clear trend in this respect was observed in this work.

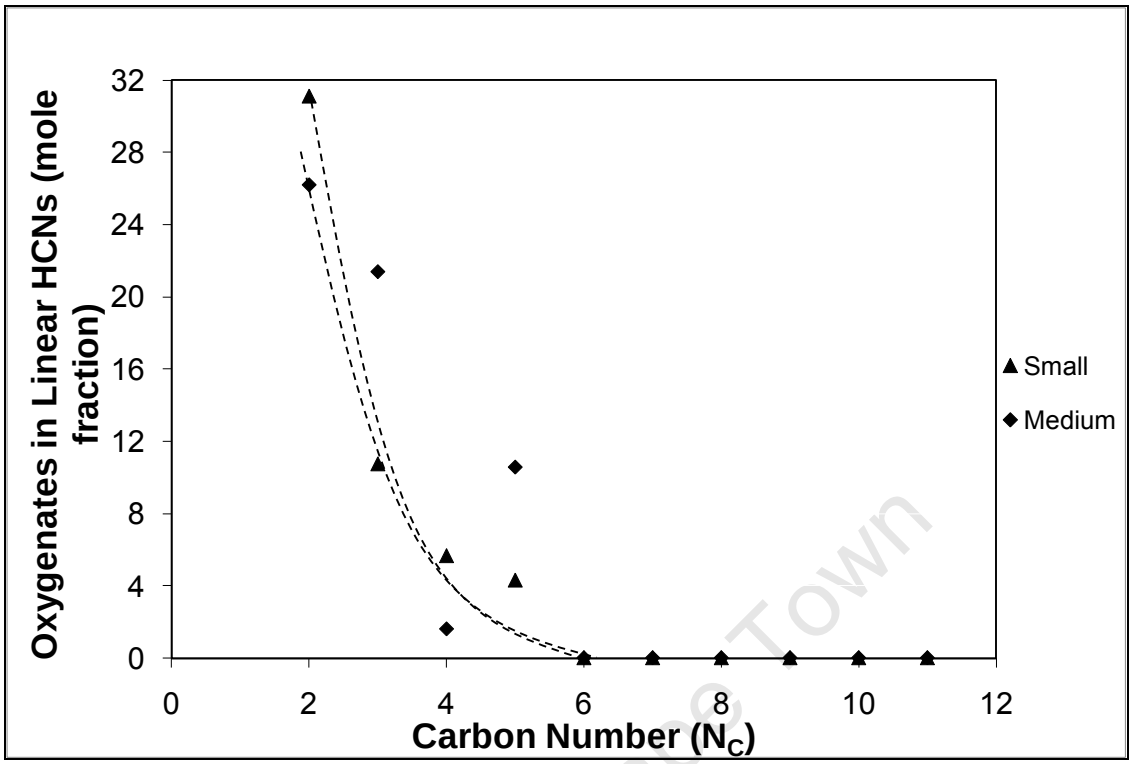

Figure 5.35: Oxygenates mole fraction in linear HCNs for the small and medium crystallites as a function of the carbon number at steady state

Branched compounds

The synthesis of tertiary carbon atoms is considered to be much more spatially demanding than the linear hydrocarbons (Schulz, 1999; Riedel et al., 2003). It is expected that as the carbon number increases (larger molecules); more space is needed on the crystallite surface in order for branched products to be synthesized resulting in the hydrocarbon branching probability being strongly dependent on the carbon number (van Steen and Schulz, 1999). Higher reaction temperatures are generally conducive for the formation of branched products (Schulz and Claeys, 1999; Riedel et al., 2003). Crystallite sizes may also impact on the selectivity of branched compounds as formation of branched compounds may be suspected to preferentially occur on corners and edges of crystallites and therefore be preferred on smaller crystallites (Welker, 2007).

A schematic of the mechanisms for the synthesis of branched hydrocarbons are shown in Figure 5.36. Figure 5.37 provides the ratio of branched to linear hydrocarbons in the C_5 fraction for the small and medium crystallites as a function of time. It can be seen that indeed more branched products form for the small crystallites than the medium crystallites. The total amounts of branched hydrocarbons ($C_4 - C_{15}$) in the products are 2.7 C-% for the small crystallites and 3 C-% for the medium crystallites. These values correspond closely to previously expected studies where the percentage of branched species in the products is between 1 – 10% (Riedel et al., 2003).

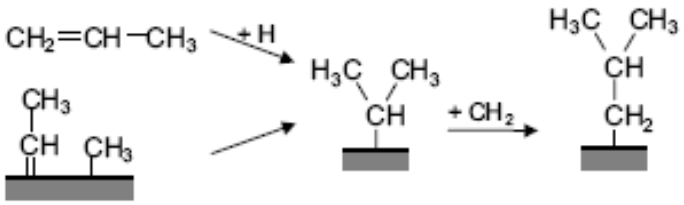

Figure 5.36: Branched products mechanisms (Mabaso, 2005)

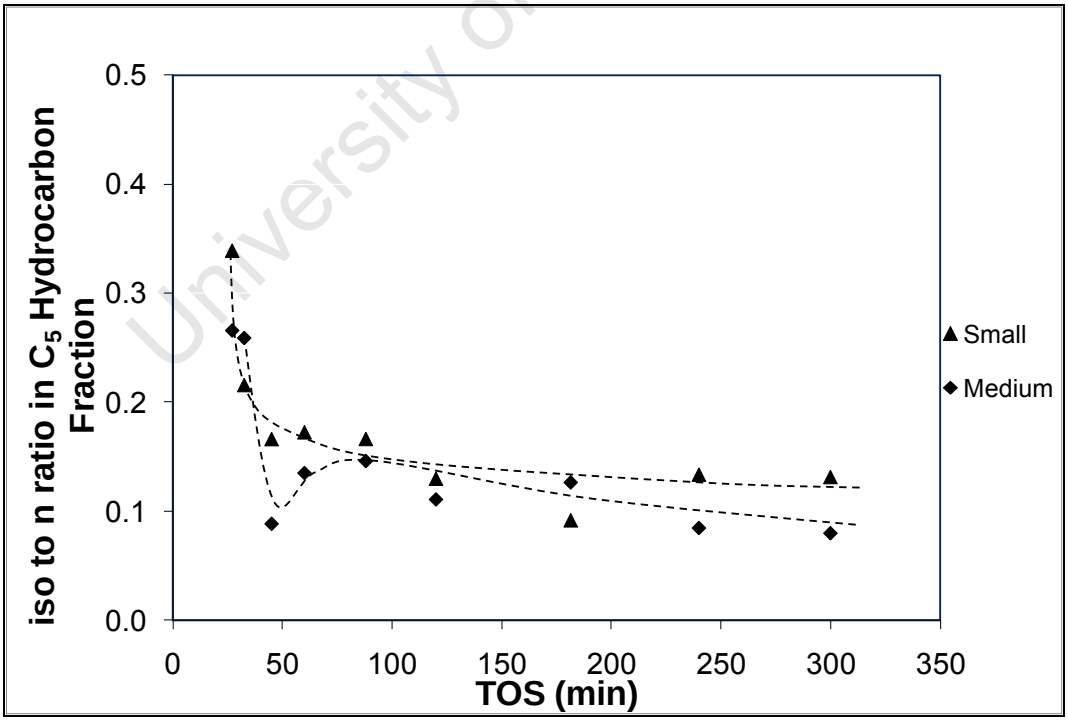

Figure 5.37: Mole ratio of iso(branched) and n(linear) hydrocarbons in C_5 fraction for the small and medium crystallites as a function of the TOS at steady state

6 Conclusion and Recommendations

Catalyst Synthesis

The focus of the study was to provide an understanding on the workings of the iron FT catalyst specifically about the CO-carbidisation of three distinct crystallite sizes. This research project has successfully achieved this objective by utilizing the reverse micelle technique and producing three narrowly distributed crystallite sizes.

The difficulty in producing the smaller crystallites resulted in the development of a different calcination procedure. The CO-carbidisation for the three crystallite sizes follows different carbidisation pathways and produces various phase compositions resulting in a change in crystallite size. The carbidisation of the crystallites also occurs at different temperatures for the various crystallite sizes. Nonetheless, two distinct crystallites sizes of mainly χ-Fe_5C_2 carbide could be achieved which were then tested for size dependency in FT synthesis.

Fischer-Tropsch Testing

The iron carbide crystallites showed a decrease in the metal surface specific Fischer-Tropsch activity as the crystallite size decreased, which is in line with observation made with metallic model catalyst systems reported in literature. It also showed that there is an increase in the methane selectivity as the crystallite size decrease corresponding to the understanding provided by the 'ensemble' effect. The crystallite sizes and narrow distributions were still maintained throughout the Fischer-Tropsch synthesis process.

From the FT-experiments it can also be concluded that the medium crystallites do form somewhat less amounts of olefins than the small crystallites.

Recommendations

Further recommendations based on the finding of the results obtained in this research project can be found on the next page:

- The carbidisation of the large crystallites should be further investigated, mainly considering an increase in the CO reduction time.
- Develop a method to synthesize three metallic iron crystallite sizes with even narrower distributions.

7 References

An, X., Wu, B., Wan, H., Li, T., Tao, Z., Xiang, H. and Li, Y., 2007, 'Comparative study of iron-based Fischer-Tropsch synthesis catalyst promoted with potassium or sodium', *Catalysis Communications*, issue 8, pp. 1957 - 1962

Arakawa, H. and Bell, A.T., 1983, 'Effects of potassium promotion on the activity and selectivity of Iron Fischer-Tropsch catalysts', *Industrial and Engineering Chemistry Process Design and Development*, issue 22, pp. 97 – 103, ACS Publications

Barkhuizen, D., Mabaso, I., Viljoen, E., Welker, C., Claeys, M., van Steen, E. and Fletcher, J.C.Q., 2006, 'Experimental approaches to the preparation of supported metal nanoparticles', *Pure Applied Chemistry*, vol. 78, pp. 1759 – 1769

Barthe, L. and Gahier, V., 2009, 'Ethane recovery processes evolve to meet market needs', Gas Department, Process Division, Technip France, *24th World Gas Conference*, Argentina

Bartholomew, C.H., 1990, 'Recent technological developments in Fischer-Tropsch catalysis', *Catalysis Letters*, issue 7, pp. 303 - 316

Bartholomew, C.H., 2001, 'Mechanisms of catalyst deactivation', *Applied Catalysis A: General*, issue 212, pp. 17 - 60

Bartholomew, C.H. and Farrauto, R.J., 2007, 'Chapter 6: Hydrogen production and synthesis gas reactions', *Fundamentals of Industrial Catalytic Processes*, edition 2, pp. 403 – 434

Bezemer, G.L., Bitter, J.H., Kuipers, H.P.C.E., Oosterbeek, H., Holewijn, J.E., Xu, X., Kapteijn, F., Dillen, A.J.V.D. and Jong, K.P.D., 2006, 'Cobalt particle size effects in the

Fischer-Tropsch reaction studied with carbon nanofiber supported catalysts', *Journal of American Chemical Society*, issue 12, pp. 3956 – 3964

Bian, G., Oonuki, A., Koizumi, N., Nomoto, H. and Yamada, M., 2002, 'Studies with a precipitated iron Fischer-Tropsch catalyst reduced by H_2 or CO', *Journal of Molecular Catalysis A: Chemical*, issue 186, pp. 203 – 213

Birkholz, M., 2006, 'Thin film analysis by x-ray scattering', Principles of X-Ray Diffraction, WILEY-VCH Verlag GmbH & Co. KGaA

Bruker, A.X.S GmbH, 2008, 'Topas 4 Whats New', Manuals, Bruker AXS GmbH, Karlsruhe, Germany

Cheang, V., 2009, 'Effect of crystallite size and water on Iron-based Fischer-Tropsch synthesis', *PhD presentation*, University of Cape Town

Claeys, M. and Schulz, H., 2004, 'Effects of internal mass transfer on activity and selectivity in iron based Fischer-Tropsch synthesis', *Preprints – American Chemical Society*, Division of Petroleum Chemistry, inc., vol. 49, no. 2, pp. 195 – 199

Claeys, M. and van Steen, E., 2004, 'Basic studies', *Studies in surface science and catalysis – Fischer-Tropsch Technology*, vol. 152, pp. 625 – 636, Elsevier B.V

Cornell, R.M. and Schwertmann, U., 2003, 'The Iron oxides: Structure, properties, reactions, occurrences and uses', 2nd edition, WILEY-VCH Verlag GmbH & Co. KGaA

Davis, B.H., Sarker, A., Seth, D., Dozier, A.K, Neathery, J.K. & Hamdeh, H.H., 2007, 'Fischer-Tropsch Synthesis: Morphology, phase transformation and particle size growth of nano-scale particles', *Catalysis Letters*, issue 117, pp. 1 – 17

Davis, B.H., 2001,'Fischer-Tropsch synthesis: current mechanism and futuristic needs', *Fuel Processing Technology*, issue 71, pp. 157 – 166

Deluzarche, A., Kieffer, R. and Muth, A., 1977, 'Reactions CO, H_2 – synthese du methanol sur chromite de zinc etude d'especes chimisorbees a la surface du catalyseur schemas reactionnels possibles', *Tetrahedron Letters*, issue 38, pp. 3357 – 3360

de Smit, E. and Weckhuysen, B.M., 2008, 'The renaissance of iron-based Fischer-Tropsch synthesis: on the multifaceted catalyst activation behavior', *The Royal Society of Chemistry*, Chemcial Society Reviews, issue 37, pp. 2758 – 2781

de Smit, E., Cinquini, F., Beale, A.M., Safonova, O.V., van Beek, W., Sauter, P. & Weckhuysen, B.M., 2010, 'Stability and reactivity of ε-χ-θ Iron carbide catalyst phases in Fischer-Tropsch synthesis: Controlling μ_C', *Journal of the American Chemical Society*, ACS Paragon Plus Environment

Dry, 2002, 'The Fischer-Tropsch process: 1950 – 2000', *Catalysis Today*, issue 71, pp. 227 - 241

Dry, 2004, 'FT catalysts' and 'Chemical concepts used for engineering purposes', *Studies in Surface Science and Catalysis – Fischer-Tropsch Technology*, vol. 152, pp. 534 – 600, Elsevier B.V

Dufek, M., 2008, 'The Nova NanoSEM user operating manual', *FEI Company*, 3rd edition

du Plessis, E, 2009, 'Topas Rietveld refinement lectures', Sasol, UCT

Eriksson, S., Nylén, U., Rojas, S. and Boutonnet, M., 2004, 'Preparation of catalysts from microemulsions and their applications in heterogeneous catalysis', *Applied Catalysis A: General*, issue 265, pp. 207 – 219

Farkas, A., 2002, 'Catalysis and Catalysts – Characterization of catalysts', *Ullmann's Encyclopedia of Industrial Chemistry*, edition 6

FEI Company and Philips, 1999, 'Tecnai F20/F30 operating manual', Transmission Electron Microscopes, 1st edition

Ferdous, D. and Demirel, B., 2010, 'Deactivation of Iron based Fischer-Tropsch catalyst – A critical problem', *2010 AIChE Spring Meeting & 6th Global Congress on Process Safety*, San Antonio, AIChE Conferences

Fisher, E. & Barron, A.R., 2009, 'Introduction to Mössbauer spectroscopy', *Connexions*, August 14, 2009, http://cnx.org/content/m22328/1.7/

Fischer, N., 2009, 'Rietveld Refinement with Topas', *Catalysis Group Seminar*, Department of Chemical Engineering, University of Cape Town

Forzatti, P. and Lietti, L., 1999, 'Catalyst deactivation', *Catalysis Today*, issue 51, pp. 165 – 181

Hayakawa, H., Tanaka, H. and Fujimoto, K., 2006, 'Studies on precipitated iron catalysts for Fischer-Tropsch synthesis', *Applied Catalysis A: General*, issue 310, pp. 24 – 30

Hayashi, H., Chen, L.Z., Tago, T., Kishida, M. and Wakabayashi, K., 2002, 'Catalytic properties of Fe/SiO_2 catalysts prepared using microemulsion for CO hydrogenation', *Applied Catalysis A: General*, issue 231, pp. 81 – 89

ImageJ, 1997, 'Image processing and analysis in Java', http://rsbweb.nih.gov/ij/index.html

Johnston, P. and Joyner, R.W., 1993, 'Structure-Function relationships in Heterogeneous Catalysis: the embedded surface molecule approach and its applications', *Studies in Surface Science and Catalysis*, volume 75, pp. 165 – 180

Kaiser, M., 1969, 'Chromatographie in der gasphase', Mannheim: Bibliographisches Institution

Kalakkad, D.S., Shroff, M.D., Köhler, S., Jackson, N. & Datye, A.K., 1995, 'Attrition of precipitated iron Fischer-Tropsch catalysts', *Applied Catalysis A*, issue 133, pp. 335 – 350

Kammermeier, B., 1998, 'Reduction – 4.5 Metals', *Ullmann's Encyclopedia of Industrial Chemistry*, release 2002, 6th edition

van der Laan, G.P., 1999, 'Kinetics, selectivity and scale up of the Fischer-Tropsch synthesis', *Thesis*, University of Groningen

Lensveld, D., 2003, 'On the preparation and characterization of MCM-41 supported heterogeneous nickel and molybdenum catalysts', Proefschrift University Utrecht, http://www.library.uu.nl/digiarchief/dip/diss/2003-0325-14324/inhoud.htm

Li, S., Krishnamoorthy, S., Li, A., Meitzner, G.D. and Iglesia, E., 2002, 'Promoted Iron based catalysts for the Fischer-Tropsch synthesis: Design, synthesis, site densities, and catalytic properties', *Journal of Catalysis*¸ issue 206, pp. 202 – 217

Li, S., Li, A., Krishnamoorthy, S. and Iglesia, E., 2001, 'Effects of Zn, Cu and K promoters on the structure and on the reduction, carburization and catalytic behavior of Iron based Fischer-Tropsch synthesis catalyst', *Catalysis Letters*, vol. 77, no. 4, pp. 197 – 205

Luo, M. and Davis, B. H., 2003, 'Fischer-Tropsch synthesis: activation of low-alpha potassium promoted iron catalysts', *Fuel Processing Technology*, issue 83, pp. 49 – 65

Luo, M., Hamdeh, H. and Davis, B.H., 2009,' Fischer-Tropsch synthesis: Catalyst activation of low alpha iron catalyst', *Catalysis Today*, issue 140, pp. 127 – 134

Mabaso, I., 2005, 'Nanosized Iron crystallites for Fischer-Tropsch synthesis', *PhD thesis*, Department of Chemical Engineering, UCT

Mahajan, D., Gütlich, P. and Stumm, U., 2003, 'The role of nano-sized particles in slurry phase Fischer-Tropsch synthesis', *Catalysis Communications*, pp. 101 – 107

Mogorosi, R.P., 2010, Verbal Discussions, *Centre for Catalysis Research (C*Change)*, Department of Chemical Engineering, UCT

Moodle, P., Scheijen, F.J.E., Niemantsverdiet, J.W. & Thüne, P.C., 2010, 'Iron oxide nanoparticles on flat oxide surfaces – Introducing a new model catalyst for Fischer-Tropsch catalysis', *Catalysis Today*, Article in Press

Niemantsverdriet, J.W., van der Kraan, A.M., van Dijk, W.L. and van der Baan, H.S., 1980, 'Behavior of metallic Iron catalysts during Fischer-Tropsch synthesis studied with Mössbauer spectroscopy, x-ray diffraction, carbon content determination and reaction kinetic measurements', *Journal of Physical Chemistry*, issue 84, pp. 3363 – 3370

Niemantsverdriet, J.W. and Chorkendorff, I., 2003, 'Solid catalysts' and 'Catalyst characterization', *Concepts of Modern Catalysis and Kinetics*, Wiley-VCH

Ning, W., Koizumi, N., Chang, H., Mochizuki, T., Itoh, T. and Yamda, M., 2006, 'Phase transformation of unpromoted and promoted Fe catalysts and the formation of carbonaceous compounds during Fischer-Tropsch synthesis reaction', *Applied Catalysis A*, issue 312, pp. 35 – 44

Pendyala, V.R.R, Jacobs, G., Mohandas, J.C., Ma, W., Gnanamani, M. and Davis, B.H., 2010, 'Study of the effect of water on Fischer-Tropsch synthesis over Iron based catalysts', *Centre for Applied Energy Research*, University of Kentucky

Pichler, H. and Schulz, H., 1970, 'Neue Erkenntinisse auf dem Gebiet der Synthese von Kohlenwasserstoffen aus CO and H_2', *Chemie Ingenieur Technik*, issue 42, pp. 1162 – 1174

Pour, A.N., Housaindokht, M.R., Tayyari, S.F. and Zarkesh, J., 2010, 'Deactivation studies of nano-structured iron catalyst in Fischer-Tropsch synthesis', *Journal of Natural Gas Chemistry*, issue 19, pp. 333 – 340

Raje, A.P., O'Brien, R.J. and Davis, B.H., 1998, 'Effect of potassium promotion on Iron based catalysts for Fischer-Tropsch synthesis', *Journal of Catalysis*, issue 180, pp. 36 – 43

Remans, T., Jenzer, G., and Hoek, A., 2008, 'Gas-to-liquids', *Handbook of Heterogeneous Catalysis*, Wiley-VCH, volume 6, pp. 2994-3010

Riedel, T., Schulz, H., Schaub, G., Jun, K., Hwang, J. and Lee, K., 2003, 'Fischer-Tropsch on iron with H_2/CO and H_2/CO_2 as synthesis gases: the episodes of formation of the Fischer-Tropsch regime and construction of the catalyst', *Topics in Catalysis*, volume 26, pp. 41 – 54

Sarkar, A. and Davis, B.H., 2007, 'Nano-Iron catalysts for Fischer-Tropsch synthesis', *Center for Applied Energy Research Presentation*, University of Kentucky

Sarkar, A., Seth, D., Dozier, A.K., Neathery, J.K., Hamdeh, H.H. and Davis, B.H., 2007, 'Fischer-Tropsch synthesis: Morphology, phase transformation and particle size growth of nano-scale particles', *Catalysis Letters*, issue 117, pp. 1 – 17

Sarkar, A., Hamdeh, H.H. and Davis, B.H., 1999, 'Fischer-Tropsch synthesis with Iron nano-catalyst', US DOE Final Technical Report

Schulz, H., 2007, 'Comparing Fischer-Tropsch synthesis on iron and cobalt catalysts - The dynamics of structure and function', *Fischer-Tropsch Synthesis, Catalysts and Catalysis*, pp. 177 – 198, Elsevier B.V

Schulz, H., Nie, Z. and Ousmanov, F., 2002, 'Construction of the Fischer-Tropsch regime with cobalt catalysts', *Catalysis Today*, issue 71, pp. 351 – 360

Schulz, H., 1999, 'Short history and present trends of Fischer-Tropsch synthesis', *Applied Catalysis A: General*, issue 186, pp. 3 – 12

Schulz, H. and Claeys, M., 1999, 'Reactions of α-Olefins of different chain length added during Fischer-Tropsch synthesis on a cobalt catalyst in a slurry reactor', *Applied Catalysis A: General*, issue 186, pp. 71 – 90

Schulz, H. and Claeys, M., 1999(b), 'Kinetically modeling of Fischer-Tropsch product distributions', *Applied Catalysis A: General*, issue 186, pp. 91 – 107

Schwuger, M.J. and Stickdorn, K., 1995, 'Microemulsions in technical processes', *American Chemical Society*, Chemical Review, issue 95, pp. 849 – 864

Seidel, C.W., 1967, 'Mössbauer spectroscopy: Principle and practice', *Nuclear Science & Engineering Corporation*, ACS Fuel Chemistry Division, preprints, volume 11, issue 4, pp 308 – 321

van Steen, E., and Schulz, H., 1999, 'Polymerisation kinetics of the Fischer-Tropsch CO hydrogenation using iron and cobalt based catalysts', *Applied Catalysis A: General*, issue 186, pp. 309 – 320

van Steen, E., 2008, 'Electronic picture of size dependent behavior in the Fischer-Tropsch synthesis', Department of Chemical Engineering, University of Cape Town

van Steen, E., 2009, 'Catalyst Preparation', *CHE5022Z Lecture*, Department of Chemical Engineering, University of Cape Town

Scintag, Inc., 1999, 'Chapter 7: Basics of x-ray diffraction', XRD resources, Department of Earth & the Planetary Sciences, The University of New Mexico, http://epswww.unm.edu/xrd/xrdbasics.pdf

Steynberg, A.P., 2004, 'Introduction to Fischer-Tropsch technology', *Studies in Surface Science and Catalysis: Fischer-Tropsch Technology*, volume 152, Elsevier B.V

Steynberg, A.P., Dray, M.E., Davis, B.H. and Breman, B.B., 2004, 'Fischer-Tropsch reactors', *Studies in Surface Science and Catalysis*, volume 152, Elsevier B.V

Stranges, A.N., 2007, 'A history of the Fischer-Tropsch synthesis in Germany 1926-45', *Studies in Surface Science and Catalysis: Fischer-Tropsch Synthesis, Catalysts and Catalysis*, pp. 1 – 22, Elsevier B.V

Varian, Inc., 1999, 'CP-3800 GC Getting Started Manual', Varian B.V.

Varian, Inc., 2007, 'User Manual CP-4900 Micro-GC', Varian B.V.

Welker, C.V., 2007, 'Ruthenium based Fischer-Tropsch synthesis on crystallites and clusters of different sizes', *PhD Thesis*, Centre of Catalysis Research, Department of Chemical Engineering, University of Cape Town

Zeiss, C., 2010, 'Transmission electron microscope', LEO 912 OMEGA Operating Manual, Energy Filter Transmission Electron Microscope (EFTEM), The Transmission Electron Microscope Unit, Physics Department, University of Cape Town, version 3.20

Appendices

A. Topas-4 Settings

Table A.1: Topas-4 settings

Background Noise		**Additional Convolutions**	
Chebychev Order	3	*Function*	*Angular Dependence*
Instrumental		Hat	Constant
Divergence Beam		Circles	-1/Tanθ
Primary & Secondary Radius (mm)	500	**Structures**	
Axial Convolutions		*Preferred Orientation*	
Full Axial Model		Cry size L (nm)	4 (minimum)
Source Length (mm)	12	PO Spherical Harmonics Order	4
Sample Length (mm)	15		
RS Length (mm)	12		
Prim. Soller (°)	2.3		
Sec. Soller (°)	2.3		
N Beta	30		

B. XRD In-situ CO Reduction Results Table

Table B.1: CO reduction results for small crystallites

Temperature	FWHM (nm)		Phase(s), Sizes (nm) and Percentages (%)					
	γ-Fe_2O_3	Iron Carbide	γ-Fe_2O_3	α-Fe_2O_3	Fe_3O_4	FeO	χ-Fe_5C_2	Rwp
30°C	7.7		7.9 (83.2)	4.0 (16.8)				8.918
75°C	7.4		7.6 (89)	4.0 (11)				8.924
100°C	7.3		7.4 (98)	4.0 (2)				9.401
125°C	7.2		7.3 (99)	4.0 (1)				9.546
150°C	7.4		7.3 (99)	4.0 (1)				10.766
175°C	7.6		7.2 (11.5)		10.5 (88.5)			10.127
200°C	8.2		7.1 (10.3)		10.7 (89.7)			10.705
225°C	8.1				10.3 (74.4)	6.0 (25.6)		11.297
250°C	6.9				12.4 (58.4)	8.0 (41.6)		10.423
275°C	6.7				12.1 (32.6)	7.2 (25.5)	4.9 (41.9)	7.957
300°C		6.7			18.2 (8.6)	13.7 (16)	7.9 (75.4)	8.613
325°C		7.2					9.4	9.896
350°C		6.7					16.5	10.148
350°C		6.7					8.6	9.383
38°C		6.3					8.0	9.662

Table B.2: CO reduction results for medium crystallites

Temperature	FWHM (nm)	Phase(s), Sizes (nm) and Percentages (%)						
		γ-Fe_2O_3	α-Fe_2O_3	Fe_3O_4	FeO	χ-Fe_5C_2 P1	Fe_3C	Rwp
30°C	11.6	11.3 (87.6)	14 (12.4)					9.814
75°C	12.0	13.8 (78.4)	16.2 (21.6)					9.739
100°C	13.0	14.9 (69.3)	19.3 (30.7)					9.724
125°C	13.6	15.4 (62.4)	19.6 (37.6)					9.591
150°C	13.2	12.9 (50.3)	17.7 (16.1)	20.1 (33.6)				9.562
175°C	11.7	15.1 (19.2)	18.4 (15.4)	15.4 (65.4)				9.942
200°C	12.8	16.0 (10.6)	17.3 (8.1)	15.8 (81.3)				8.973
225°C	14.6		15.5 (21.3)	15.1 (78.7)				10.504
250°C	15.6			20.8 (59.4)	10.5 (40.6)			11.967
275°C	14.7			22.3 (43.8)	10.6 (19.5)		3.7 (36.7)	9.492
300°C	14.1			24.2 (20.9)			7.1 (79.1)	10.162
325°C	13.5			32.3 (6.8)			8.9 (93.2)	10.442
350°C	11.5					11.6 (51.1)	2.3 (48.9)	7.614
350°C	10.1					10.0 (59.7)	3.3 (40.3)	8.388
38°C	9.8					9.3 (76.5)	3.5 (23.5)	9.065

Table B.3: CO reduction results for large crystallites

Temperature	FWHM (nm)			Phase(s), Sizes (nm) and Percentages (%)				
	α-Fe_2O_3	Fe_3O_4	Fe	γ-Fe_2O_3	α-Fe_2O_3	Fe_3O_4	Fe	Rwp
30°C	32.3			8.0 (24.8)	43.8 (59.7)	6.4 (15.5)		13.415
75°C	32.3			7.9 (25.1)	43.4 (59.2)	6.5 (15.7)		13.515
100°C	30.9			7.9 (25.4)	43.4 (59.2)	7.1 (15.4)		13.410
125°C	29.7			8.4 (24.3)	43.5 (58.1)	5.9 (17.6)		13.358
150°C	32.3			8.8 (23.1)	43.8 (57.2)	5.3 (19.7)		19.8
175°C	30.9			9.0 (23.0)	43.7 (55.5)	4.5 (21.5)		11.965
200°C	32.3			9.0 (24.5)	44.8 (53.1)	4.0 (22.4)		10.336
225°C	33.8			9.6 (26.0)	45.3 (52.9)	4.0 (21.1)		9.085
250°C	33.8			9.8 (30.0)	45.3 (51.4)	4.0 (18.6)		8.746
275°C		13.6		4.0 (19.5)	46.9 (28.2)	21.1 (52.3)		9.334
300°C		18.1		4.0 (14.1)	22.9 (13.1)	18.6 (77.3)	27.8 (5.5)	9.298
325°C		19.5			23.5 (9.6)	21.1 (73.3)	33.4 (17.1)	8.531
350°C			30.0		22.9 (67.9)	25.6 (4.3)	42.6 (27.8)	9.218
350°C			33.9		28.2 (2.5)	24.2 (52.7)	49.9 (44.8)	9.828
38°C			34.0		29.7 (3.8)	23.0 (52.8)	49.5 (43.4)	10.604

C. Anderson-Schulz-Flory Distributions

The following figures contain the linear product distributions of the small and medium crystallites during the initial and steady state.

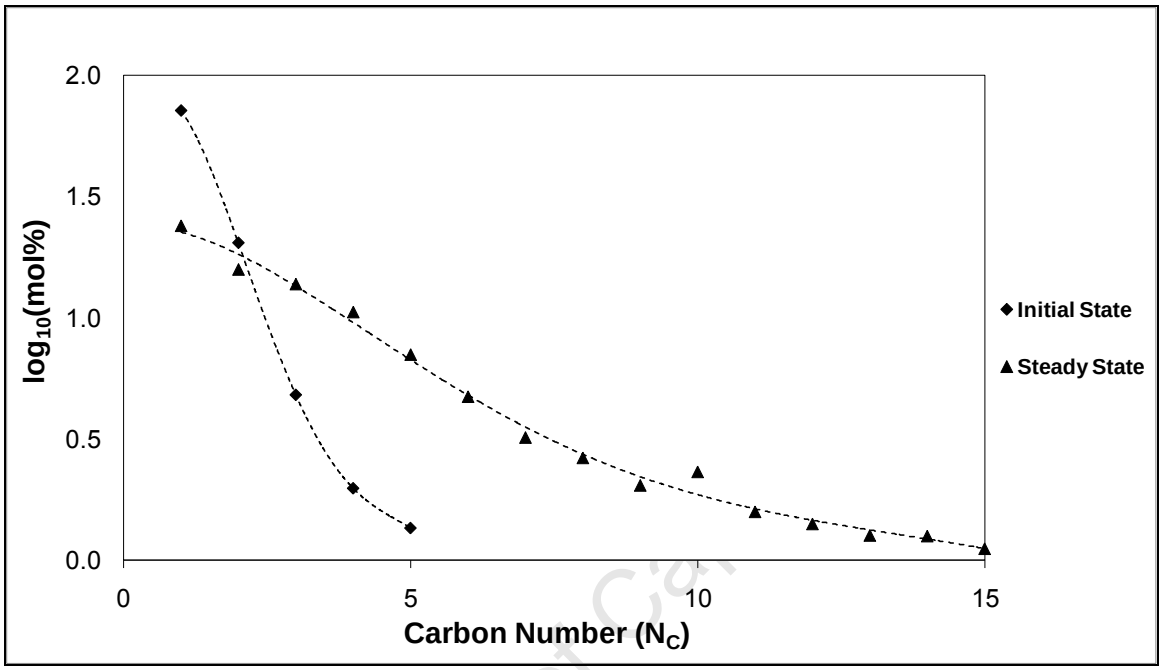

Figure C.1: ASF distribution of the initial and final state for the small crystallite

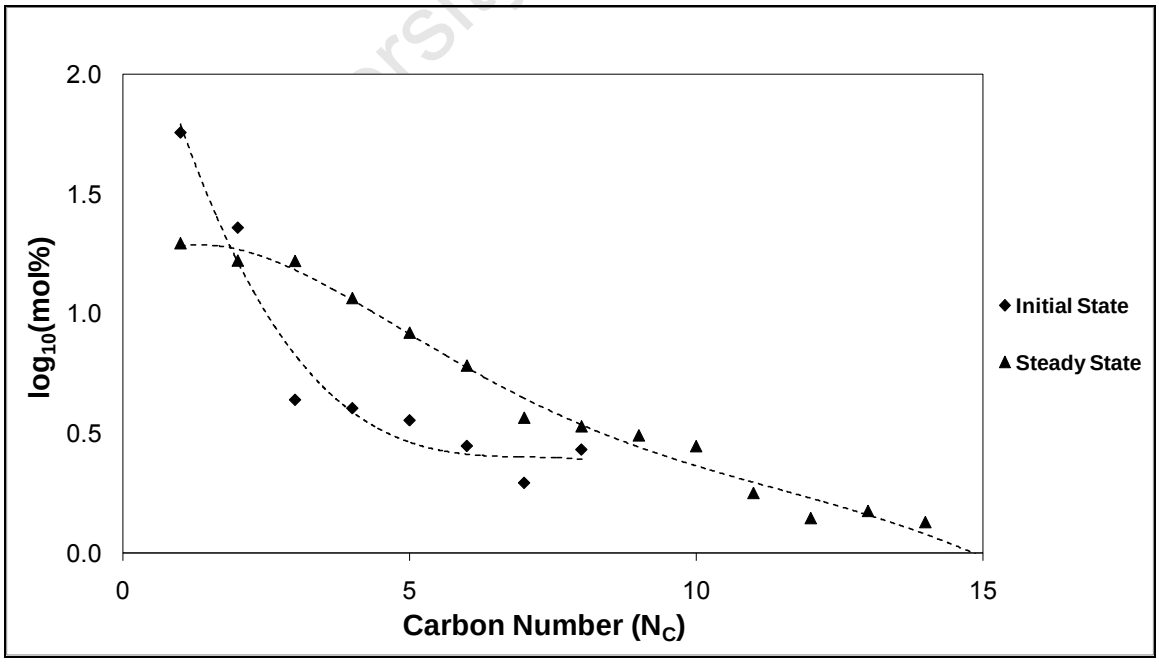

Figure C.2: ASF distribution of the initial and final state for the medium crystallite

D. GC Chromatograms

This section provides an example of a GC chromatogram used to identify the products and to determine the amount of hydrocarbons relative to the methane production.

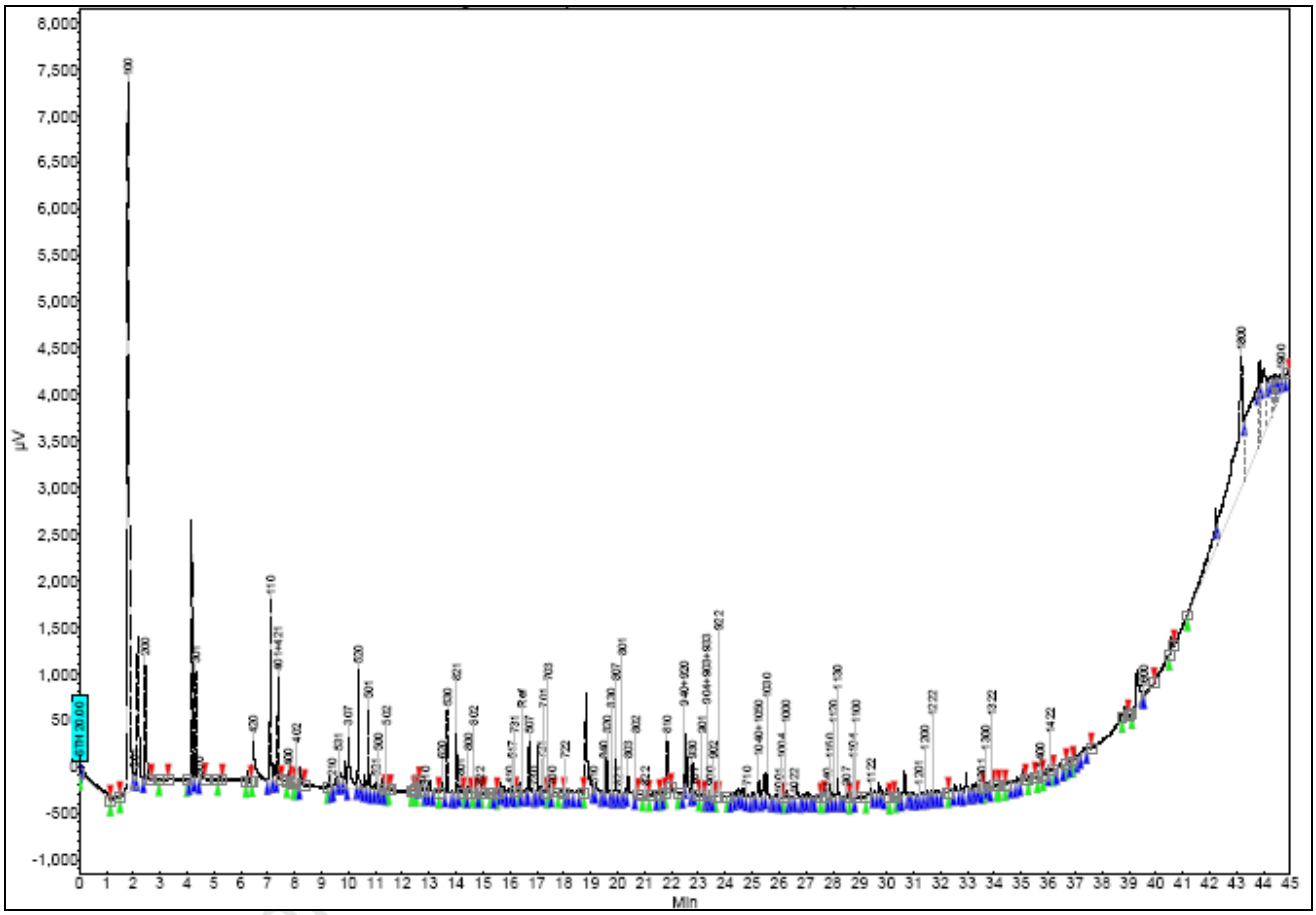

Figure D.1: A GC chromatogram sample

E. Tables Corresponding to Graphs for FT Testing

Table E.1: Information for the small crystallite's conversion, FT rate, CH_4 and CO_2 selectivity

Time (min)	CO Conversion (%)	FT Rate (mol/min.nm^2)	CH_4 selectivity (%)	CO_2 Selectivity (%)
10	7.60	1.29E-07	71.49	4.36
27	7.09	1.20E-07	51.82	4.63
33	7.36	1.25E-07	50.29	4.44
45	7.36	1.23E-07	48.24	4.58
60	6.82	1.15E-07	42.34	5.10
88	5.94	9.87E-08	37.94	6.47
92	5.92	9.81E-08	38.61	6.64
120	6.13	1.01E-07	33.70	7.09
182	6.87	1.13E-07	29.56	7.32
240	9.44	1.57E-07	23.31	6.11
300	9.45	1.56E-07	22.56	6.71

Table E.2: Information for the medium crystallite's conversion, FT rate, CH_4 and CO_2 selectivity

Time (min)	CO Conversion (%)	FT Rate (mol/min.nm^2)	CH_4 selectivity (%)	CO_2 Selectivity (%)
10	44.29	1.78E-06	52.79	0.68
27	9.56	3.76E-07	45.38	3.00
33	6.92	2.69E-07	37.93	4.28
45	3.86	1.43E-07	33.56	8.62
60	3.42	1.25E-07	31.07	10.12
88	3.47	1.24E-07	22.47	11.85
92	3.84	1.38E-07	26.03	11.29
120	4.77	1.74E-07	22.08	9.93
182	5.83	2.12E-07	20.59	10.30
240	5.52	1.99E-07	19.41	11.12
300	5.95	2.15E-07	17.10	10.97

Table E.3: Initial and steady state ASF distributions for small and medium crystallites

Carbon Number	Small		Medium	
	Initial State	Steady State	Initial State	Steady State
1	1.85	1.38	1.76	1.29
2	1.31	1.20	1.36	1.22
3	0.68	1.14	0.64	1.22
4	0.30	1.02	0.61	1.07
5	0.13	0.85	0.55	0.92
6	0.00	0.67	0.45	0.78
7	0.00	0.51	0.29	0.57
8	0.00	0.42	0.43	0.53
9	0.00	0.31	0.00	0.49
10	0.00	0.36	0.00	0.45
11	0.00	0.20	0.00	0.25
12	0.00	0.15	0.00	0.15
13	0.00	0.10	0.00	0.18
14	0.00	0.10	0.00	0.13
15	0.00	0.05	0.00	-0.04

Table E.4: Olefins in linear hydrocarbons at steady state for small and medium crystallites

Carbon Number	Small	Medium
	mole fraction	
2	0.75	0.69
3	0.77	0.77
4	0.76	0.74
5	0.75	0.73
6	0.74	0.72
7	0.73	0.71
8	0.72	0.70
9	0.72	0.67
10	0.70	0.65

11	0.68	0.62

Table E.5: Olefins in C_5 hydrocarbons at initial and steady states for small and medium crystallites

	Initial State	Steady State
Small	0.46	0.75
Medium	0.56	0.73

Table E.6: Olefins in linear C_5 hydrocarbons at steady state for small and medium crystallites

Time (min)	Small	Medium
10	1	1
27	1	1
33	1	1
45	0.72	0.77
60	0.88	0.87
88	0.89	0.86
92	0.91	0.87
120	0.92	0.86
182	0.93	0.90
240	0.94	0.90
300	0.94	0.90

Table E.7: Steady state oxygenates in linear hydrocarbons for small and medium crystallites

Carbon Number	Small	Medium
1	2.78	4.21
2	31.10	26.22
3	10.74	21.41
4	5.65	1.60
5	4.30	10.57
6	0.00	0.00
7	0.00	0.00

Table E.8: Iso to n ratio in C_5 hydrocarbons for small and medium crystallites

TOS (min)	Small	Medium
10	0.00	0.00
27	0.34	0.27
33	0.22	0.26
45	0.17	0.09
60	0.17	0.14
88	0.17	0.15
120	0.13	0.11
182	0.09	0.13
240	0.13	0.08
300	0.13	0.08